論文 / 著書情報
Article / Book Information

題目(和文)	
Title(English)	Cyclic behavior of steel beam-end connections with horizontal or vertical oblique angle
著者(和文)	劉雨辰
Author(English)	Yuchen Liu
出典(和文)	学位:博士(工学), 学位授与機関:東京科学大学, 報告番号:甲第373号, 授与年月日:2025年3月26日, 学位の種別:課程博士, 審査員:吉敷 祥一,河野 進,石原 直,佐藤 大樹,山﨑 義弘
Citation(English)	Degree:Doctor (Engineering), Conferring organization: Institute of Science Tokyo, Report number:甲第373号, Conferred date:2025/3/26, Degree Type:Course doctor, Examiner:,,,,
学位種別(和文)	博士論文
Type(English)	Doctoral Thesis

Cyclic behavior of steel beam-end connections with horizontal or vertical oblique angle

Doctor Dissertation

December, 2024

Institute of Science Tokyo

Liu Yuchen

ABSTRACT

As the beam-to-column connection is a critical component for absorbing seismic energy, its damage and fracture have always been focused as important topics for research. In recent years, due to advancements in building design and functional requirements, the shapes of beam-to-column connections have become more complicated to accommodate these developments. One of the commonly seen forms of beam-to-column connections involves the connection with oblique angles. However, in existing studies on the behavior of these connections, the seismic performance and the effect of oblique angles have not been thoroughly investigated.

This dissertation as a fundamental study on beam-to-column connections with oblique angles, focusing on the beam-end connection, which has the most significant shape changes. This dissertation investigates the cyclic behavior, failure sections, and effects of steel beam-end connections with horizontal or vertical oblique angles through full-scale experiments and finite element (FE) analysis.

In the chapter 2, the effects of horizontal oblique angles on the elastoplastic behavior of beam-end connections under cyclic loading were investigated. The von Mises criterion was employed to predict the failure sections of beam flange. An element test validated these predictions and demonstrated that horizontal oblique angles significantly influence the strain distribution at the obtuse angle zone and plastic deformation capacity. Subsequently, a full-scale experiment was conducted to confirm the conclusions from the element test. In the full-scale experiments, the beam-to-column connections with oblique angles exhibited stable hysteretic behavior and same behavior in elastic and plastic state, indicating that the oblique angle had little effect on the overall cyclic behavior of the connections. Additionally, the strain concentration was also observed at the obtuse angle zone. The failure section of the connection was perpendicular to the beam's axis. As a result, to avoid premature failure caused by strain concentration, it is recommended to use an extended diaphragm method for the connections with horizontal oblique angles greater than 15 degree.

In the chapter 3, the effects of vertical oblique angles on the elastoplastic behavior of beam-end connections under cyclic loading were investigated, and a mechanism analysis for beam-to-column connections was proposed. In the mechanism analysis, the internal forces in the upper and lower flanges were calculated, and the failure section from the upper flange to the lower flange was identified. Additionally, a method for defining beam span in beam-to-column connections with vertical oblique angles was presented. To validate the results of the

mechanism analysis, a full-scale experiment was conducted. The full-scale experimental results showed that beam-to-column connections with vertical oblique angles exhibited stable hysteretic behavior and almost the same elastic and plastic behavior under cyclic loading. The analysis of failure modes and the number of cycles to failure showed that as the vertical oblique angle increased, the plastic deformation capacity of the connections noticeably decreased. These results consistent with the results of the mechanism analysis.

In the chapter 4, FE analysis using ABAQUS was conducted to study the behavior of beam-end connections with vertical or horizontal oblique angles. For the vertical oblique angles, the FE analysis accurately reproduced the experimental results by providing internal forces at the failure section, thereby confirming the effectiveness of the mechanism analysis. The results showed that the internal force in the upper flange increased linearly with increasing vertical oblique angle. Moreover, the effects of loading direction, beam depth, and span were analyzed to further understand their impact on the behavior of connection. Similarly, for horizontal oblique angles, the FE analysis successfully reproduced the hysteretic behavior observed in the experiments and analyzed plastic strain changes at the beam end. The numerical analysis revealed strain concentration changes in the obtuse angle zone under varying horizontal oblique angles, beam widths, and spans. Based on these deformation conditions, a strain analysis was conducted, and an equation for predicting the strain concentration was derived.

CONTENT

5. Conclusions and future works

A. Appendices

CHAPTER 1

Introduction

1.1 Background

Steel moment-resisting frames (SMRFs) are widely used in earthquake-prone areas due to their excellent capacity for absorbing seismic energy. In these systems, beams and columns work together as a unit, absorbing seismic energy through plastic deformation to prevent the rapid collapse of buildings. A common design approach in SMRFs is the strong column-weak beam concept. Under this design criterion, beam-to-column connections are designed to form plastic hinges at the beam ends (Fig. 1.1). Consequently, when evaluating SMRFs, the seismic behavior and plastic deformation capacity of beam-to-column connections are critical factors.

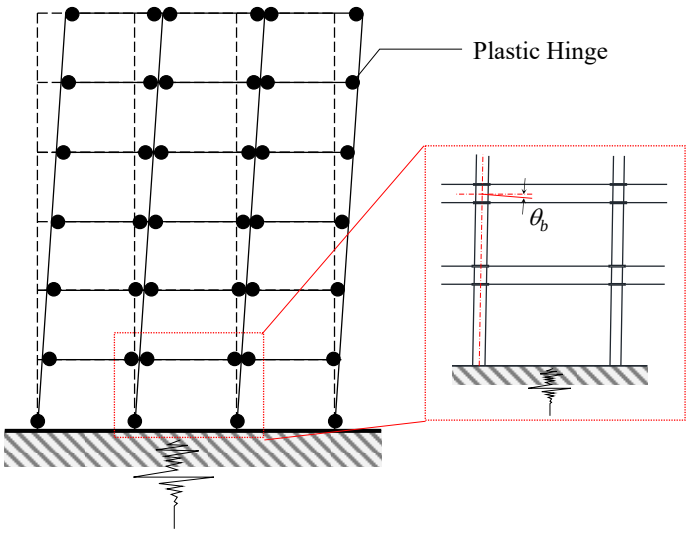

Fig.1.1 Strong column-weak beam concept of SMRFs

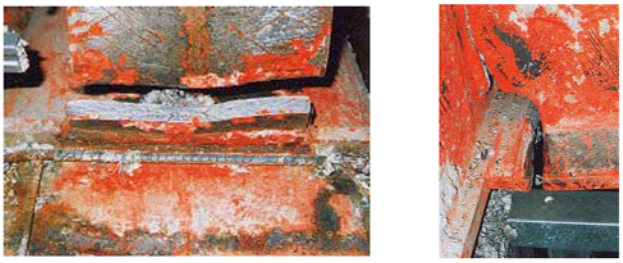

Fig.1.2 Fracture photos of beam-to-column connections in Kobe earthquake.[29]

Following the 1994 Northridge earthquake and the 1995 Kobe earthquake, brittle fractures were observed around the lower flange of beam-to-column connections [1-4]. Investigations revealed issues such as insufficient welding material strength and defects in the welding details at the beam-to-column connections. To prevent premature fractures at beam-end, numerous countries have conducted research on the design of beam-to-column connections. In the United States, the SAC Steel Project was initiated, leading to the development of design recommendations for steel structures, such as FEMA-350 and AISC, to standardize and improve beam-to-column connection quality [5-6]. Similarly, in Japan, Takatsuka K. et al. [7] conducted experimental studies comparing the deformation capacity of welded access holes and slot welds, elucidating the corresponding fracture modes. Suita K. et al. [8] investigated the effects of different weld access hole details and proposed new weld access hole details to prevent strain concentration and brittle fractures at the ends of the weld access holes. Additionally, Ishii T. et al. [9] conducted experiments on beam-to-column connections, using different kinds of steel and connection types to investigate their impact. In Europe, to address seismic concerns, the EU code, specifically Eu 1993-1-8 [10], provides regulations for the construction methods of beam-to-column connections.

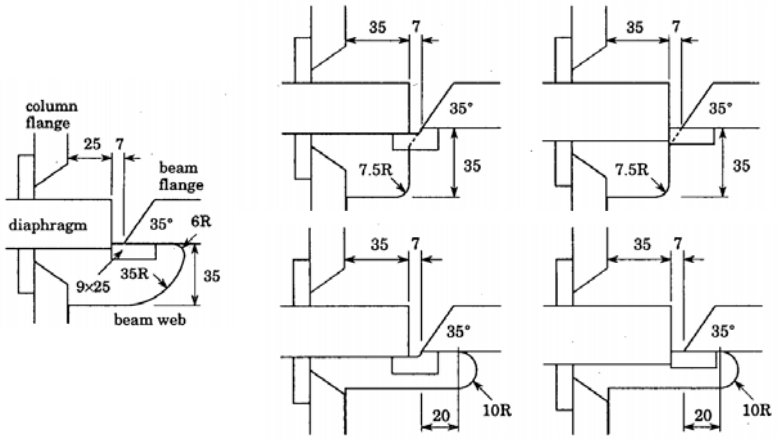

Fig.1.3 Different type of weld access hole in Japan after Kobe earthquake.[8]

Additionally, To effectively evaluate the performance of beam-to-column connections, loading protocols employed for beam-to-column connections test. Various countries have developed design recommendations that include suggested loading protocols. For example, the United States has the SAC protocol [11], Japan recommend Japan Iron and Steel Federation protocol[12].

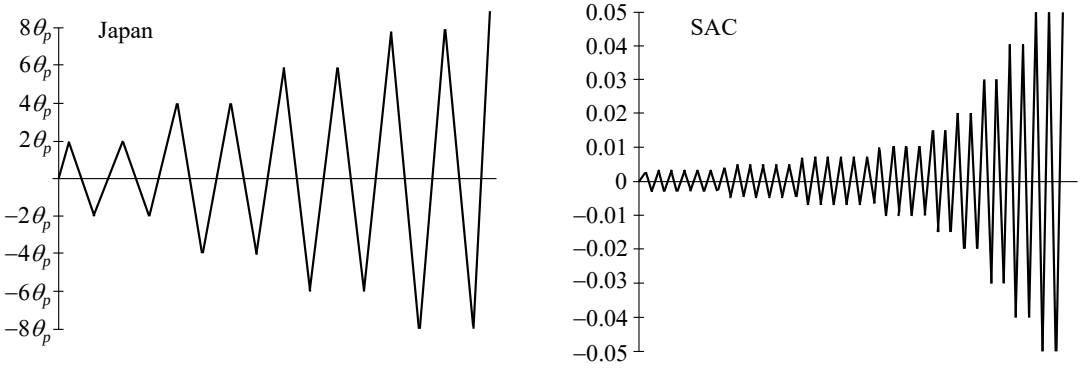

Fig.1.4 Loading protocol of recommendation.[11-12]

However, during the 2011 Tohoku earthquake, long-period ground motions were observed, as shown in Fig.1.5. Buildings were subjected to prolonged swaying under these long-period earthquake ground motions [13]. In such conditions, the fatigue life of beam-to-column connections was severely challenged. Traditional loading protocols were not effective in accurately reflecting the plastic deformation capacity of beam-to-column connections under these circumstances. Consequently, in the wake of the 2011 Tohoku earthquake, much of the research on beam-to-column connections has focused on the fatigue performance of these connections. For example, Y.L. Chung et al. [15] conducted experiments on 24 beam-to-column connections using a large shaking table to simulate long-period ground motion, elucidating the performance of beam-to-column connections under different welding methods. Experimental results show that the presence of RC slabs causes strain concentration at the lower flange end,

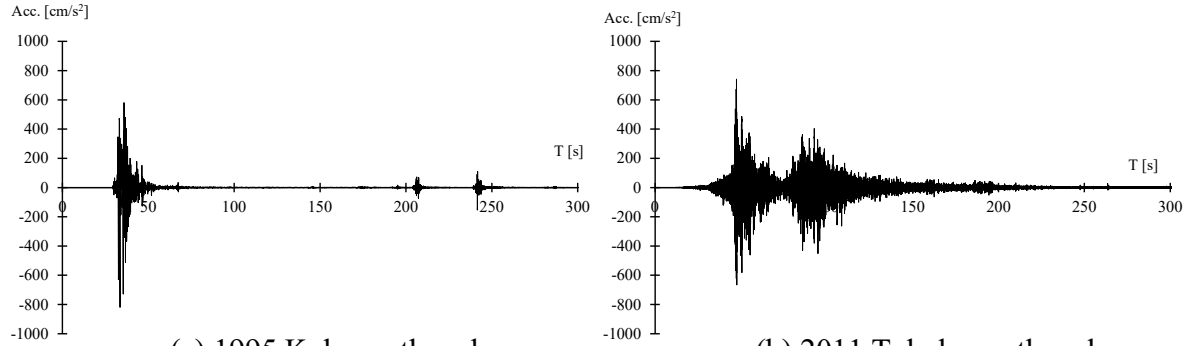

(a) 1995 Kobe earthquake (b) 2011 Tohoku earthquake

Fig.1.5 Acceleration time history of earthquake.[14]

leading to a 50% reduction in plastic deformation capacity. D.G. Lignos et al. [16] used simulations to propose a stiffness deterioration model based on Ibarra-Krawinkler model, highlighting that low-cycle fatigue induced connections fractures under long-period ground motion increase the story drift of the lower stories in high-rise buildings. D.S. Lee et al. [17] introduced the J_b coefficient, which is the ratio of the yield strength of the flange and web in beam-to-column connections to the yield strength based on the section of beam member, and demonstrated that beam-to-column connections with similar J_b values exhibit comparable fatigue life, regardless of the type of beam-to-column connection.

In recent years, with the advancement of research on beam-to-column connections, their seismic performance under various conditions has been studied. For instance, the seismic performance of beam-to-column connections under ground motions of different direction[18] or at the corners of buildings [19]. Simultaneously, to address increasingly complex architectural designs, attention has been given to developing complex forms of beam-to-column connections to solve various needs. Examples include eccentric beam-to-column connections (Fig.1.6 (a)) used at the outer edges to address architectural shape issues [20-21], special-shaped beam-to-column connections designed to accommodate differences in column section sizes (Fig.1.6 (b)) [22-23], and vertically eccentric beam-to-column connections to address variations in floor height (Fig.1.6 (c)) [24-25]. Although these types of beam-to-column connections are not frequently used, they exist in practice and are needed. Due to the complex force transferring characteristics and difficulty of fabrication methods of these beam-to-column connections, their failure modes differ significantly from those of traditional connections. The safety of the-

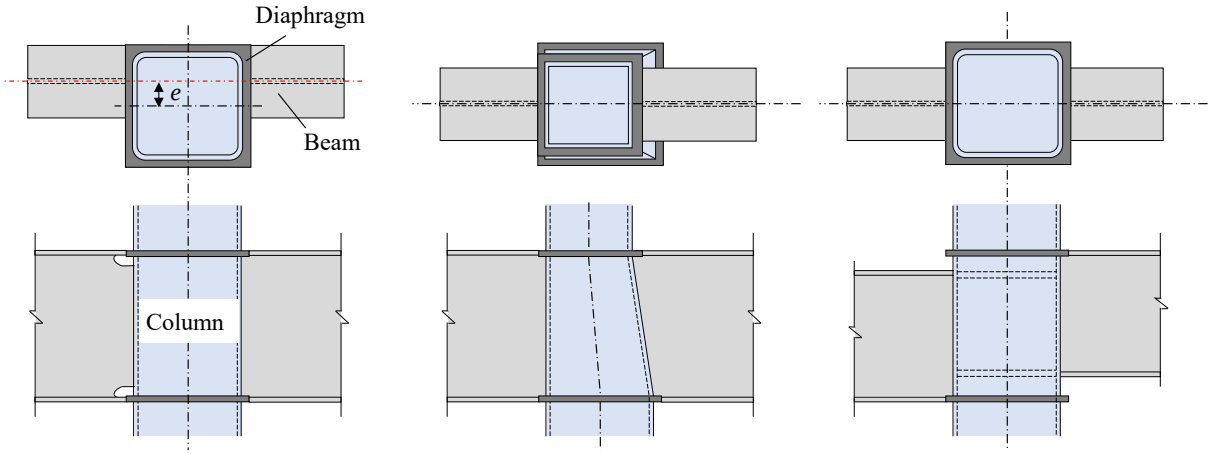

(a) Eccentric connections (b) Different column section (c) Vertically eccentric connections

Fig.1.6 Complex forms of beam-to-column connections.

se connections has received considerable attention. In Japan, some of these complex beam-to-column connection designs have already been incorporated into recommendations [26], as well as into standard details of steel structure for easier production [27-28].

1.2 Statement of problem

In the background section, various stages of research on beam-to-column connections were discussed. Including studies on different shapes of beam-to-column connections, all of which employed perpendicular configurations between beam and column. However, to meet the demands of large spaces or specific architectural designs, beam-to-column connections with oblique angle(Fig.1.7) are also frequently used. As early as the 1995 Kobe earthquake, failures of these types of beam-to-column connections were observed [29], as shown in Fig.1.8. However, after this earthquake, there has been very little research on beam-to-column connections with oblique angles, resulting in limited understanding of their seismic

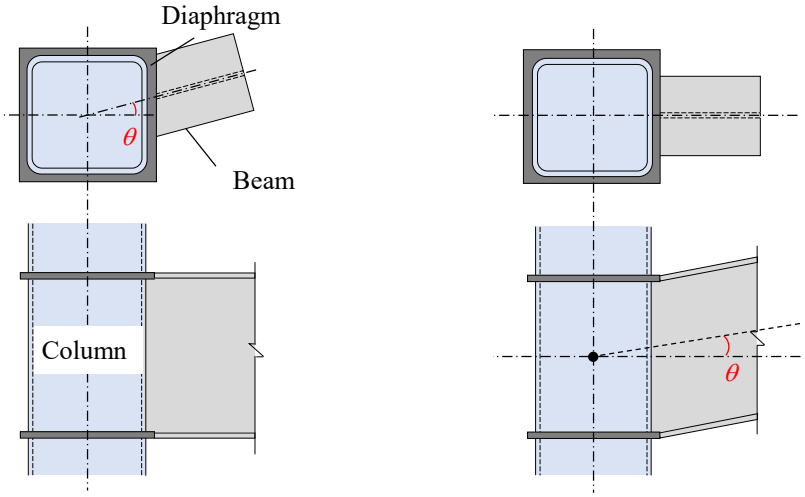

(a) Connection with horizontal oblique angle. (b) Connection with vertical oblique angle.

Fig.1.7 Beam-to-column connections with oblique angle.

(a) Connection with horizontal oblique angle. (b) Connection with vertical oblique angle.

Fig.1.8 Damage to connections with oblique angles caused by the Kobe earthquake.[29]

performance. Up to now, design codes in various countries, such as in Europe and the U.S., rarely address these types of connections. In Japan, there are some design standards on the handling methods for producing beam-to-column connections with oblique angle [26-27], but the effect of oblique angle and the failure mode of beam-to-column are limited. Given this gap in research, it is crucial to understand the different types of beam-to-column connections with oblique angles. Beam-to-column connections with oblique angle can be broadly classified into vertical and horizontal type. Due to the presence of oblique angles, the flange and web of beam-to-column connections become irregular in shape, leading to changes in their mechanical characteristics and connection details. As a result, these changes can potentially affect the seismic performance of the connections, making it essential to investigate the impact of oblique angles more thoroughly.

1.3 Objectives and Scope of Research

In order to address the evaluation of beam-to-column connections with horizontal and vertical oblique angles, this study aims to elucidate the effects of oblique angles on the seismic performance of beam-to-column connections, including the effects on their basic hysteretic behavior (elastic stiffness and maximum strength) and plastic deformation capacity. The study will investigate the effects of oblique angles through mechanism analysis, full-scale experiments and analytical simulations.

The mechanism analyses will concentrate on the beam end to investigate whether the oblique angle changes the force transmission mechanism and failure modes. The experimental parts will involve cyclic loading tests on full-scale specimens to observe the fracture modes and cyclic behavior of each specimen, thereby validating the mechanism analyses. The Finite element (FE) analysis will replicate the experiments to determine whether such complex beam-to-column connections can be accurately modelled, and to investigate the causes of the observed effects through FE analysis. Finally, by analyzing different connection methods in FE models, design recommendations for beam-to-column connections with vertical and horizontal oblique angle will be given.

1.4 Structure of Dissertation

This dissertation is composed of five chapters, providing a detailed introduction to the seismic performance of beam-column connections with vertical and horizontal oblique an-

gles.

Chapter 1 presents the background of beam-to-column connections.

Chapter 2 describes the experiments and analyses of beam-to-column connections with horizontal oblique angle, evaluating their seismic performance and the impact of horizontal oblique angle.

Chapter 3 describes the experiments and analyses of beam-to-column connections with vertical oblique angle, assessing their seismic performance and the effect of vertical oblique angle.

Chapter 4 summarizes the impact of the oblique angles discussed in Chapters 2 and 3, addressing the negative effects of the oblique angles on behavior of beam-to-column connections through analytical models.

Chapter 5 concludes with a summary of all findings from the research work and discusses future works.

References

[1] M. Nakashima, K. Inoue, M. Tada M, Classification of damage to steel buildings observed in the 1995 Hyogoken-Nanbu earthquake, Eng. Struct. 20 (1998) 271–281.

[2] J.M. Ricles, J.W. Fisher, Le-Wu Lu, Kaufmann E.J. Development of improved welded moment connections for earthquake-resistant design, J. Constr. Steel Res. 58 (2002) 565 –604.

[3] S.A. Mahin, Lessons from damage to steel buildings during the Northridge earthquake, Eng. Struct. 20 (1998): 261–270.

[4] H. Akiyama, Evaluation of fractural mode of failure in steel structures following Kobe lessons, J. Constr. Steel Res. 55 (2002) 211–227.

[5] Recommended Seismic Design Criteria for New Steel Moment-Frame Buildings. FEMA -350, USA Federal Emergency Management Agency, Washington, DC; 2000

[6] ANSI/AISC 341-10. Seismic provisions for structural steel buildings. Chicago, IL: AISC; 2010.

[7] K. Takatsuka, K. Suita, Y. Manabe, T. Tanaka, T. Tsukada, Effect of beam-to-column

connection details on deformation capacity of cyclic loading, In Proceedings of the 14th World Conference on Earthquake Engineering (2008) 12–17.

[8] K. Suita, M. Nakashima, K. Morisako, Tests of welded beam-column subassemblies. I: Global behavior, J. Struct. Eng. 124 (1998) 1245–1252.

[9] T. Ishii, S. Kikukawa, K. Morita, K. Takanashi, Experiment Study on Fracture Behavior of Beam-to-column Connection. Proceedings of Constructional Steel 6 (1999) 87–102 (in Japanese).

[10] EN 1993-1-8, Design of Steel Structures - Part 1-8: Design of joints, 2021.

[11] Federal Emergency Management Agency. Interim testing protocols for determining seismic performance characteristics of structural and nonstructural components. FEMA-461 Draft Document, Applied Technology Council, Redwood City, CA, 2007.

[12] Building Research Institute and the Japan Iron and Steel Federation. Study on Testing Method for Structural Performance Evaluation of Steel Structures. Tokyo, 2002.

[13] T. Okazaki et al., Damage to steel buildings observed after the 2011 Tohoku-Oki earthquake, Earthquake spectra 29.1_suppl (2013) 219-243.

[14] Building Research Institute (BRI), Quick Report of the Field Survey and Research on "The 2011 off the Pacific Coast of Tohoku Earthquake (the Great East Japan Earthquake)", Technical Note of NILIM No. 636, BRI Research Paper No. 132, 2011. http://www.kenken.go.jp/japanese/contents/topics/20110311/0311quickreport.html

[15] Y.L. Chung et al., Seismic resistance capacity of beam–column connections in high-rise buildings: E-Defense shaking table test, J Earthq Eng Struct Dyn. 40 (2011) 605-622.

[16] D.G. Lignos et al., Numerical and experimental evaluation of seismic capacity of high-rise steel buildings subjected to long duration earthquakes, Computers and Structures 89 (2011) 959–967.

[17] D.S. Lee et al., Experimental study of low-cycle fatigue behavior of a welded flange-bolted web connection in steel moment-resisting frames, Earthquake Spectra 34.4 (2018) 1829-1846.

[18] Y. Wang et al. Elastoplastic behavior of week-panel beam-column joints with RC slabs under bidirectional loading. J. Constr. Steel Res. 168 (2020) 105880.

[19] R. Nie et al. HSS steel corner column to H-beam joints under cyclic bidirectional load-

ings: Experiment, numerical modeling, and calculation. J. Constr. Steel Res. 192 (2022) 107239.

[20] H. Kuwamura, Y. Sato, Local behavior of eccentric connection of non-diaphragm CHS and beam, J. Struct. Constr. Eng. AIJ 80 (2015) 1785–1794. (in Japanese).

[21] T. Matumiya et al., Cyclic loading test on eccentrically beam-to-column connection part 1-2. Summaries of Technical Papers of Annual Meeting Architectural Institute Japan 2007. pp. 791-794 (in Japanese).

[22] L. Liang, et al. Seismic behavior of irregular shaped beam-column connections, Eng. Struct. 297 (2023) 116942

[23] B. Mou et al., Experimental investigation on shear behavior of steel beam-to-CFST column connections with irregular panel zone. Eng. Struct. 168 (2018) 487-504.

[24] B. Mou, et al., Numerical investigation and design method of bolted beam-column joint panel with eccentricity in beam depths, J. Constr. Steel Res. 180 (2021) 106568.

[25] B. Mou et al., Shear behavior of panel zone with an eccentricity between beam depths: Parameter study and design methodology, Journal of Building Engineering, 40 (2022) 103690.

[26] Architectural Institute of Japan, AIJ Recommendation for Design of Connections in Steel Structures, Maruzen, Tokyo, 2021. (In Japanese)

[27] Japan Steel Constructors Association (JSC). Standard Detail of Steel Structural Frame. Japan Steel Structure Journal Co., Tokyo, 2016 (in Japanese).

[28] Japan Steel Constructors Association (JSC). Design Catalogue of Connections detail of Steel Structures. Japan Steel Structure Journal Co., Tokyo, 2017 (in Japanese).

[29] Reconnaissance Report on Damage to Steel Building Structures Observed from the 1995 Hyogoken-Nanbu (Hanshin/Awaji) Earthquake. Steel Committee of Kinki Branch the Architectural Institute of Japan (AIJ),1995 (in Japanese).

CHAPTER 2

Cyclic loading test of beam-end connections with horizontal oblique angle

2.1 Introduction

Steel structures possess excellent seismic performance and energy dissipation capabilities, making them commonly used in earthquake-prone areas. As an earthquake-prone country, Japan has a large number of mid-rise buildings, among which the application of steel structures is widespread. In mid-rise steel frame structures, one of the most common beam-to-column connections is through diaphragm connection. In Chapter 1, the introduction describes various complex beam-to-column connections. According to the Japanese "Standards details of Structural Frame" [1], there are some cases which beams and columns must be connected at an oblique angle. Unlike the seismic behavior of standard beam-to-column connections (Fig.2.1(a)), the seismic characteristics of beam-to-column connections with horizontal oblique angle (Fig.2.1(b)) are not well understood. Notably, beam-to-column connections with

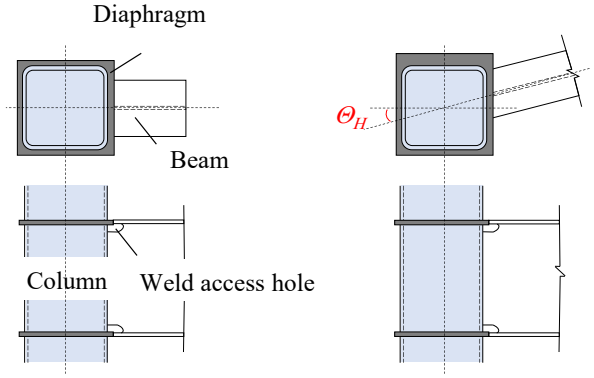

(a) Through diaphragm method. (b) Connection with horizontal oblique angle Θ_H

Fig.2.1 Different type of beam-to-column connections.

horizontal oblique angle introduce bidirectional shear forces in the panel zone, and the irregular shapes of the beam-end connections further complicate the analysis. Under these circumstances, it is essential to study the seismic behavior of beam-to-column connections with horizontal oblique angle.

In previous studies, Kaibara et al. [2] conducted experiments with shear loading directions of 30° and 45°, to investigate the behavior of the panel zone under bidirectional shear forces, reporting on the cyclic behavior of the panel zone. Arakida et al. [3][4] studied the cyclic behavior of panel zones with different aspect ratios under bidirectional shear forces through experiments and finite element (FE) analysis. These studies demonstrated that the panel zone exhibits stable hysteretic behavior, with higher maximum strength observed at the 45° loading direction. However, these studies only tested the panel zone and did not include the beam portion.

Recently, several studies have focused on the strength and ductility of the panel zone with beam portion, to clarify the impact of non-vertical ground motion inputs on the behavior of beam-to-column connections. Wang et al. [5][6] developed weak panel-type beam-to-column connections with a three-dimensional cruciform to test the cyclic behavior of the panel zone under bi-directional loading. Chan et al. [7] proposed a new analytical model to predict the cyclic behavior of the panel zone under bidirectional loading, which aligned well with the experimental results [5]. Additionally, some studies have investigated beam-to-column connections under bidirectional cyclic loading at corner of buildings[8][9]. Although these studies indicated that the fracture mode in the panel zone under bidirectional loading was different, the panel zone still exhibited stable hysteretic behavior, consistent elastic stiffness, and considerable strength [4][5][7]. Therefore, these studies suggested that when beam-to-column connections with horizontal oblique angle are subjected to cyclic loading, the panel of these connections will shows stable cyclic behavior and greater strength.

Following previous studies, using the strong column weak beam design criteria can control the seismic behavior of the panel zone in beam-to-column connection with horizontal oblique angle. However, the behavior of the irregularly shaped beam ends has yet to be clarified. Therefore, more experiments are needed on beam ends of beam-to-column connection with horizontal oblique angle to provide detailed information on their hysteretic behavior and failure mode. To elucidate the seismic behavior of the beam ends, this chapter investigates the hysteretic behavior and plastic deformation capacity of beam-to-column connections with hor-

izontal oblique angle. The research includes mechanism analysis, element testing and full-scale experiments. The von Mises criterion was firstly used to calculate the failure sections. Then, an element test was carried out to verify the conclusion. Full-scale experiment were also conducted. Specimens were subjected to cyclic loading to determine their hysteretic behavior. The seismic behavior was evaluated by comparing the effects of horizontal oblique angle, hysteretic behavior, skeleton curves, and fracture modes.

2.2 Mechanism analysis

This chapter analyzes the failure sections at the beam ends using the von Mises criterion [10]. A beam-end with horizontal oblique angle is shown in Fig.2.2(a). When the beam is subjected to shear force, due to the maximum bending moment appearing at the beam end, two potential failure sections can be anticipated as shown in Fig.2.2(b). The *t*-section is subjected to the maximum bending moment, while the *u*-section is perpendicular to the beam flange and represents the shortest fracture path.

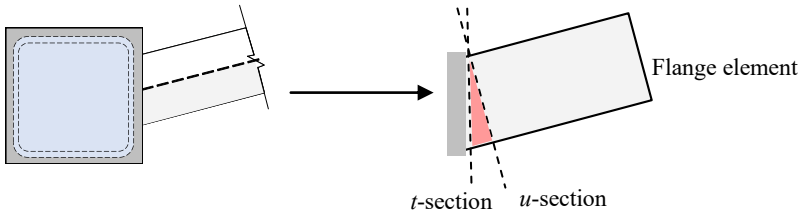

Fig.2.2 Definition of flange element.

Based on the von Mises yield criterion, the strength of the two sections is examined. Taking half of the beam's flange as the subject, its stress state under tensile force is illustrated in Fig.2.3. Here, the tensile force is denoted as *P*. For the purpose of establishing equations, the angle $\theta_f = (90°\text{-}\Theta_H)$ is defined and used in the subsequent discussion (Fig.2.3). Then, the stress yield condition is expressed by the following Eq.

$$\Phi = \sigma_n^2 + 3\tau_{nt}^2 - Y^2 = 0 \tag{2.1}$$

Where σ_n and τ_{nt} are the normal and shear stresses on the *t*-section (see Fig. 2.3),and Y is the uniaxial yield stress. When the subject develops an incremental deformation du, the deformation caused by the normal stress σ_{nt} is expressed as $du\sin\theta_f$, and the deformation caused by the shear stress τ_{nt} is expressed as $du\cos\theta_f$. Therefore, the stress work W_{in} is calculated using the Eq.(2.2).

$$W_{in} = (\sigma_n \sin\theta_f + \tau_{nt} \cos\theta_f)du \tag{2.2}$$

According to the normality rule, the following equations can be given, where ζ is the propor-

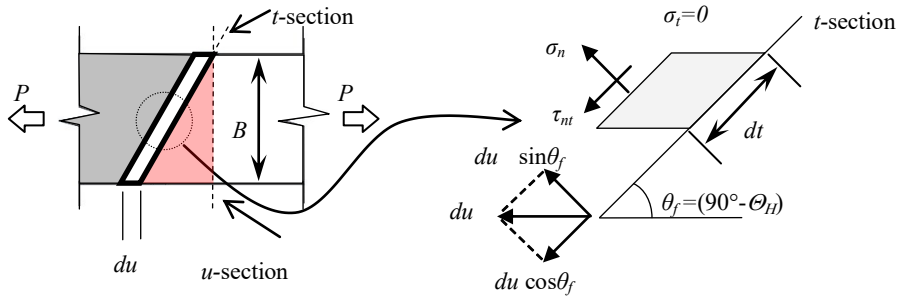

Fig.2.3 Examination of stress state of the flange element.

tionality constant.

$$du\sin\theta_f = \zeta\frac{\partial\Phi}{\partial\sigma_n} = 2\zeta\sigma_n, du\cos\theta_f = \zeta\frac{\partial\Phi}{\partial\tau_{nt}} = 6\zeta\tau_{nt} \tag{2.3}$$

Using Eqs. (2.1) – (2.3), τ_n and τ_{nt} can be derived as follows:

$$\sigma_n = \frac{3\tan\theta_f}{\sqrt{3(3\tan^2\theta_f+1)}}Y, \tau_{nt} = \frac{1}{\sqrt{3(3\tan^2\theta_f+1)}}Y \tag{2.4}$$

By integrating Eqs. (2.2) and (2.4), W_{in} from the *t*-section can be expressed using Eq. (2.5).

$$W_{in} = \sqrt{(1+2\sin^2\theta_f)}\frac{Y}{\sqrt{3}}du \tag{2.5}$$

When the thickness of the flange is set to *d*, based on the relationship between stress work and deformation, the failure strengths P_t and P_u of the *t* and *u*-sections can be expressed as follows:

$$P_u = YBd, P_t = \frac{W_{in}Bd}{du\sin\theta_f} = \frac{\sqrt{(1+2\sin^2\theta_f)}YBd}{\sqrt{3}\sin\theta_f} \tag{2.6}$$

The relationship between the failure strength ratio P_u/P_t determined by Eq.(2.6) and the horizontal oblique angle Θ_H is shown in Fig. 2.4. It can be observed that the smaller the angle θ_f, meaning the larger the horizontal oblique angle Θ_H, the greater the failure strength of *t*-section compared to *u*-section. This indicates that in beam flange with an oblique angle, *t*-section does not constitute a critical failure section.

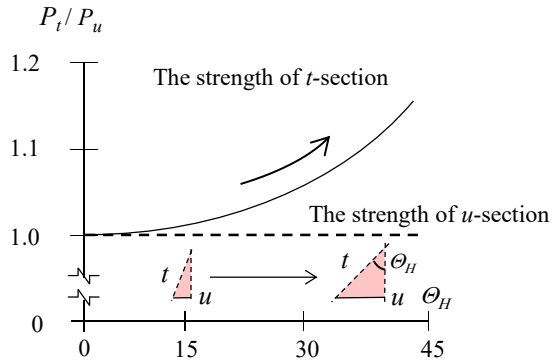

Fig.2.4 Relationship between failure strength and horizontal oblique angle.

2.3 Element test

A tensile test on flange elements with horizontal oblique angle was conducted, including verification of the results based on the von Mises yield criterion in Section 2.2.

2.3.1 Test specimens

An overview of the specimens is shown in Fig. 2.5, whose shape followed the JIS standard[11]. The properties of materials used are listed in Table 2.1. The test assumed an H-beam (RH400x200x8x13) is connected to a diaphragm with horizontal oblique angle. The specimens were designed to replicate the flanges and diaphragms of the H-shaped steel beam using PL12 (SS400) and PL36 (SS400), respectively. In this test, a sufficient thickness of PL36 diaphragm was used to confirm the failure section.

The weld between the beam flange element and the diaphragm featured a 7mm root gap and a 35° bevel angle, and it used complete joint-penetration (CJP) groove welded with a backing plate FB-9x25. JIS YGW18 electrode (F_{EXX} = 550 N/mm^2 and minimum CVN toughness of 70 J at 0 °C) [12] was employed for the welding. The strength of the weld was significantly higher than the yield strength of the specimen

The parameter was the horizontal oblique angle Θ_H. Four specimens (L series) were pre-

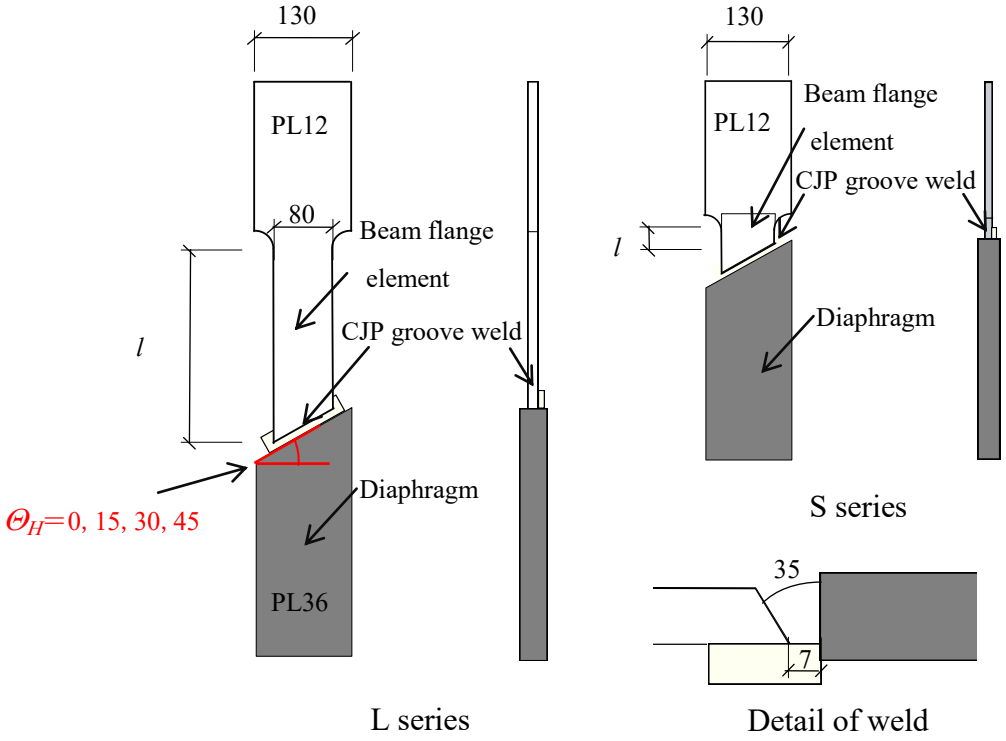

Fig.2.5 Test specimens of beam flange element.

pared for horizontal oblique angles of Θ_H=0°, 15°, 30°and 45°, named L0, L15, L30, L45, respectively. The length l of the beam flange element part of the L series is 250mm. Additionally, three more specimens (S series), which parameter was horizontal oblique angles of Θ_H =15°, 30°and 45° with beam flange element lengths 1/10th of the L series were prepared to promote failure of the beam flange element.

Table 2.1 Properties of materials

Test specimens		σ_y [N/mm^2]	σ_u [N/mm^2]	*E.L.*[%]
Beam flange element	SS400 PL12	316	425	28
Diaphragm	SS400 PL36	296	450	33
Welding electrode	YGW 18	467	565	28

Note: *E.L.*: Elongation

2.3.2 Measurement plan

The test was conducted using tensile testing machine, ensuring that the center of the element aligned with the direction of tensile force. The specimen was clamped at both ends, approximately 170mm from each end, the load was applied monotonically until fracture could be observed.

The measurement plan is shown in Fig. 2.6, and the setup photo is presented in Photo 2.1. The measuring range of specimens was defined as L_0. During the test, deformation δ was obtained using relative displacements measured by displacement transducers installed at the upper and lower of the specimen. Strain gauges were attached near the welding part between the beam flange element and the diaphragm in both u and t-section to measure local strain ε in each position.

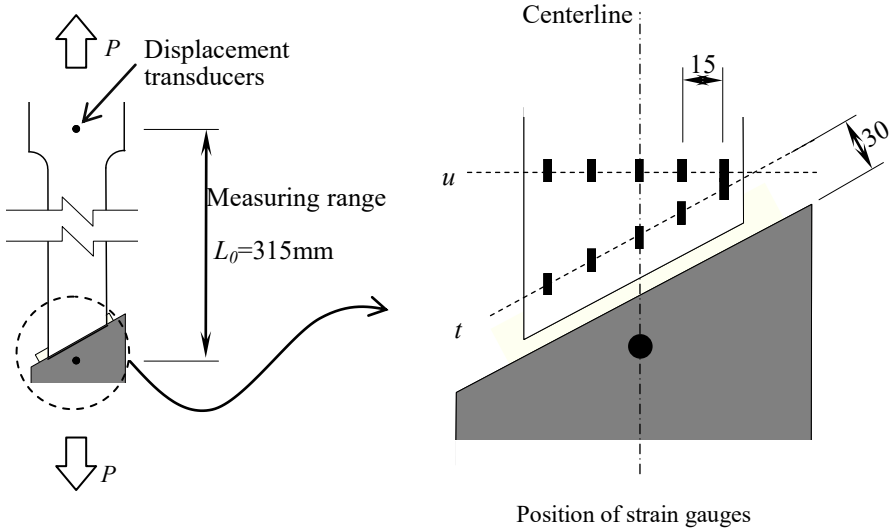

Fig.2.6 Measurement plan.

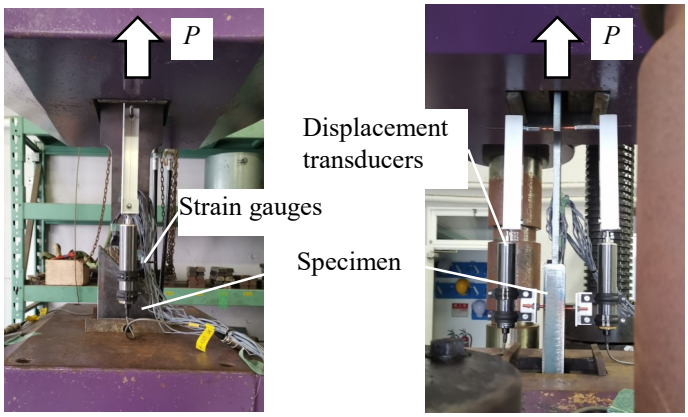

(a) Front view (b) Side view

Photo 2.1. Experimental setup (Specimen L45)

2.3.3 Test results

The relationship between tensile force P and average strain for each series is shown in Fig. 2.7. The vertical axis represents the tensile force P, and the horizontal axis represents the average strain ε_{ave}, calculated by $\varepsilon_{ave}=\delta/L_0$. Different color distinguishes the specimens with different horizontal oblique angle, and black markers indicate the ultimate deformation δ_u of the specimens. The test result observed shows that all specimens initially increased linearly with load while maintaining almost same stiffness and yielded strength around 260 kN. After yielding, the load increased with strain hardening. Additionally, L45 and S45 fractured without reaching the ultimate force, whereas other specimens reached ultimate force before fracturing.

Table 2.2 presents the comparison of test results for each specimen. It was observed that the horizontal oblique angle did not influence the stiffness (k), yield force (P_y), or the ultimate force (P_u). However, the ultimate deformation (δ_u) decreased with increasing horizontal

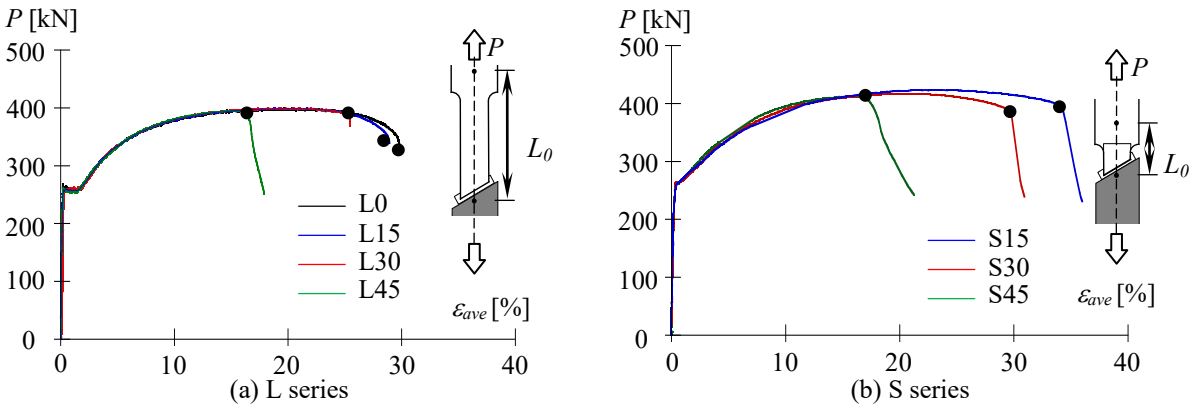

Fig.2.7 Loading behavior of specimens.

oblique angles, indicating a significant impact on the deformation capacity. Photo 2.2 shows the ultimate state of the specimens. All specimens fractured at the *u*-section, confirming the von Mises criteria calculations. Specimen L45, S15, S30, S45, unlike L0, L15, and L30, exhibited premature fracture initiating at the point marked by the red arrow in Photo 2.2, then propagated along the *u*-section until completed failure.

Table 2.2. Summarize of test results.

	Len. of beam flange element l [mm]	Measuring range L_0[mm]	Stiffness k[kN/mm]	Yield force P_y[kN]	Ultimate force P_u[kN]	Ult. deformation δ_u[mm]	Fracture section
L0	250	315	217	257	398	74.6	*u*
L15			209	258	399	72.4	*u*
L30			210	255	399	63.0	*u*
L45			211	257	395	42.0	*u*
S15	42	107	217	266	424	14.6	*u*
S30	55	120	200	254	417	16.8	*u*
S45	72	137	208	260	412	12.7	*u*

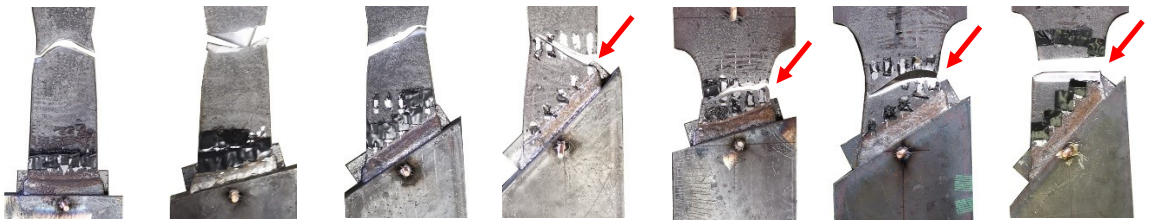

L0 L15 L30 L45 S15 S30 S45

Photo 2.2. Ultimate state of the specimens.

To compare the impact of horizontal oblique angle on the plastic deformation capacity of the L and S series, the test results of horizontal oblique angles and ultimate plastic deformation are summarized in Fig. 2.8. The vertical axis represents the ratio of the ultimate plastic deformation of L series specimens to that of the L0 specimen, and for the S series, it is compared to the S15 specimen. The horizontal axis represents horizontal oblique angle. The results indicate that as the horizontal oblique angle increases, the ultimate plastic deformation capacity significantly decreases, particularly at 45 degrees, where it decreases by nearly 50%.

For further analysis, the strain distributions in the *t* and *u*-sections of L series were also compared, as shown in Fig. 2.9. The local strain ε was picked at the point when deformation δ reached 20 mm, representing the strain hardening phase of each specimen. The distance x indicated the position of the strain gauges. In the figure, the acute angle zone was within 10 mm along the *t*-section, and the obtuse angle zone was at the intersection of the *t* and *u*-

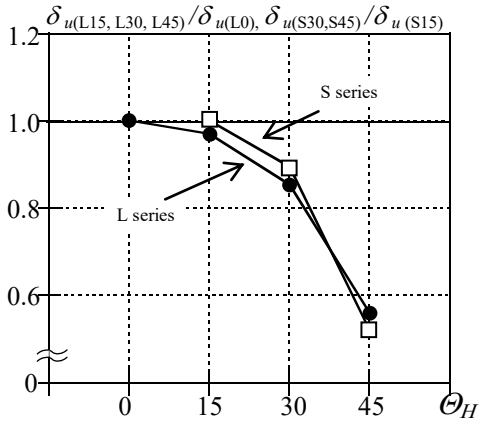

Fig. 2.8 Effect of horizontal oblique angle on deformation capacity

sections (Fig. 2.9(b)). For specimens L15, L30, and L45, the local strain ε values in the obtuse angle zones were larger than those in the acute angle zones. Particularly for specimens L30 and L45, the local strain ε of the *t*-section significantly decreased from the obtuse to the acute angle zone, indicating that the local strain in specimens with horizontal oblique angle is concentrated in the obtuse angle zone.

Additionally, Fig.2.9 compares the local strain ε at every position along the *t* and *u*-sections. Since the ε of the *u*-section exceeded that of the *t*-section, the *u*-section was considered the failure section. For specimen L45, the local strain ε in the obtuse angle zone was 2 times higher than that of a point with distance x=10 mm in the *u*-section. This phenomenon led to a premature fracture at the position indicated by the red arrow (Photo 2.2).

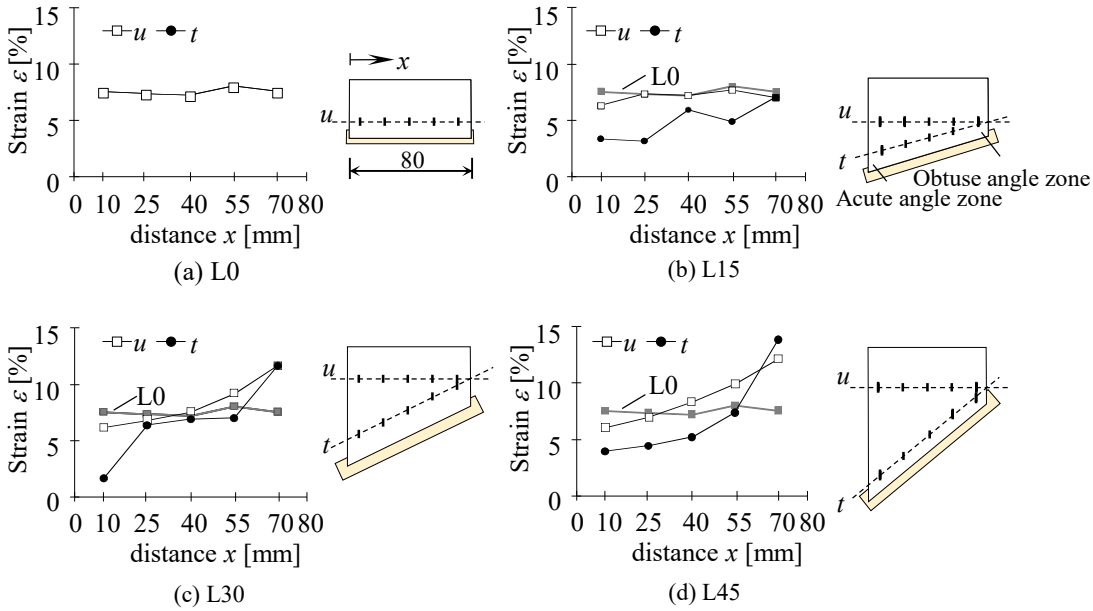

Fig. 2.9 Effect of horizontal oblique angle on deformation capacity.

To confirm the relationship between the degree of strain concentration and the reduction in ultimate deformation capacity, the strain concentration was evaluated, as shown in Fig.2.10. In this figure, the vertical axis represents $\varepsilon_{max\text{-}L\Theta H}/\varepsilon_{ave\text{-}L0}$, where $\varepsilon_{max\text{-}L\Theta H}$ is the maximum local strain of each specimen pick from Fig. 2.9 and $\varepsilon_{ave\text{-}L0}$ is the average local strain of the specimen L0. This ratio represents the degree of strain concentration. The reduction of ultimate deformation capacity $\delta_{u-L0}/\delta_{u-L\Theta H}$ was compared with the strain increasing ratio. The results indicated that the strain increasing ratio correlates with the reduction in ultimate deformation capacity, confirming that strain concentration is a primary cause of reduced ultimate deformation capacity.

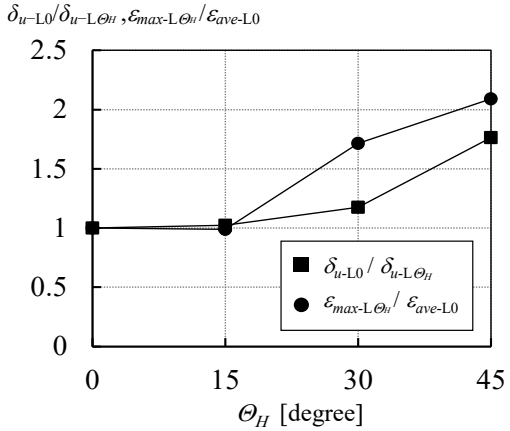

Fig. 2.10 Comparison between ultimate deformation capacity and strain increasing ratio.

2.4 Test program of beam-to-column connections

Based on the element test results, horizontal oblique angles cause strain concentration, which may lead to premature fracture in the obtuse angle zone of beam flange elements. To accurately understand the overall behavior of beam-to-column connections, full-scale experiments were planned. In these experiments, the specimens were designed according to the strong column-weak beam concept to ensure the beam yields before the column and diaphragm. The specimens will use the through diaphragm method, which is commonly applied in Japanese steel structure buildings.

2.4.1 Test specimens

Similar to the element tests, the parameter in the full-scale experiments was the horizontal oblique angle Θ_H. A total of five specimens were tested, and the detail of specimens is

shown in Fig.2.11(a). A specimen without an horizontal oblique angle (Θ_H=0°) served as the standard specimen (NS0), while the other specimens had horizontal oblique angles of 15° (NS15), 30° (NS30), and 45° (NS45). For the connections with horizontal oblique angle, the beam ends were cut to accommodate the oblique angles. Simultaneously, another specimen with a horizontal oblique angle of 15° (NS15E) was tested. The connection of NS15E specimen was fabricated using the methods outlined in the "Standards details of Structural Frame,"[1] with an extended diaphragm to accommodate the horizontal oblique angles, as shown in Fig. 2.11(a).

For all the specimens, the beam dimension was H-400 × 200 × 8 × 13 (depth × flange width × web thickness × flange thickness), made of SS400 steel (nominal yield strength of 235 N/mm² and tensile strength over 400 N/mm²). The columns were cold-rolled square hollow sections (SHS) made of BCR295 steel (nominal yield strength of 295 N/mm² and tensile strength over 400 N/mm²), with dimensions of 250 × 250 × 12 (depth × width × plate thickness).

Table 2.3 lists the material properties of the specimens. Fig. 2.11(b) shows the welding details of beam-to-column connections. The beam-to-column connections were welded to the diaphragm using the through diaphragm method. To ensure the diaphragm remain elastic during the experiments, it was made of SN490C steel (nominal yield strength of 325 N/mm²

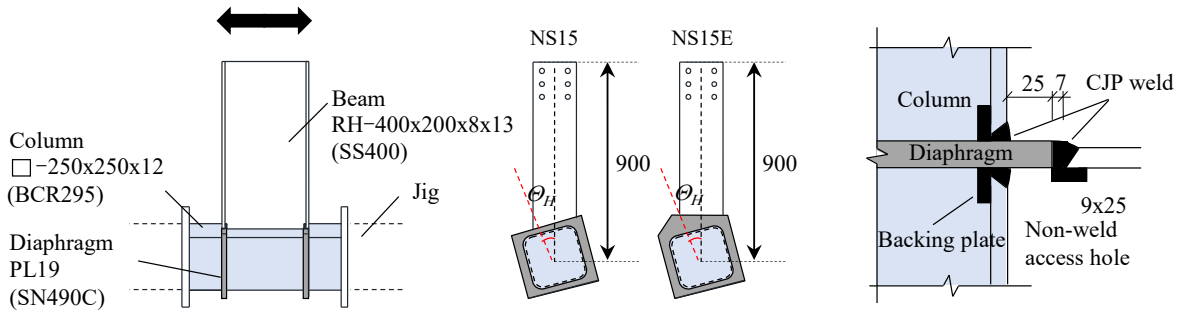

(a) Specimens detail (b) Detail of weld

Fig.2.11 Test specimens.

Table.2.3 Material properties of the full-scale experiment.

Part	Steel type	Thickness t [mm]	Yield strength σ_y [MPa]	Ultimate strength σ_u [MPa]	Y.R. [%]	E.L. [%]
Beam flange	SS400	13	383	438	87	30
Beam web	SS400	8	412	501	82	22
Column	BCR295	12	393	489	80	14

Note: Y.R.: Yield ratio, E.L.: Elongation

and nominal tensile strength over 490 N/mm²), with a thickness of 19 mm. The diaphragm extend 25 mm outward from the column face, in accordance with Design of Connections in Steel Structures Specifications of Japan [13]. The beam flanges and columns were welded to the diaphragm using CJP welds, and the beam webs were welded to the columns using fillet welds. Since weld access holes affect strain distribution and deformation capacity of beam flange, potentially leading to failures near the welds access hole [14], all specimens were connected using non-welded access holes method.

2.4.2 Measurement plan and setup

The setup is shown in Fig. 2.12, with photographs of the setup in photo 2.3. To facilitate loading, a new design was adopted in the setup. The direction of the beam was fixed, and variations in oblique angles were achieved by rotating the column. In this setup, the column ends of the specimens were pin connected to the frame through column jigs. The distance between two pins were 2400 mm. The beam part of specimen was extended using a beam extension jig, and the end of beam extension jig connected to a hydraulic jack. Lateral supports were installed at the top and middle of the beam to prevent lateral buckling. Table 2.4 lists the span and details of each specimen. Due to the varying of horizontal oblique angles, specimens S15, S30, and S45 had irregular beam ends. In these cases, the center of web was set as the measurement point for span L (marked in Table 4 and Fig. 2.12). The length L,

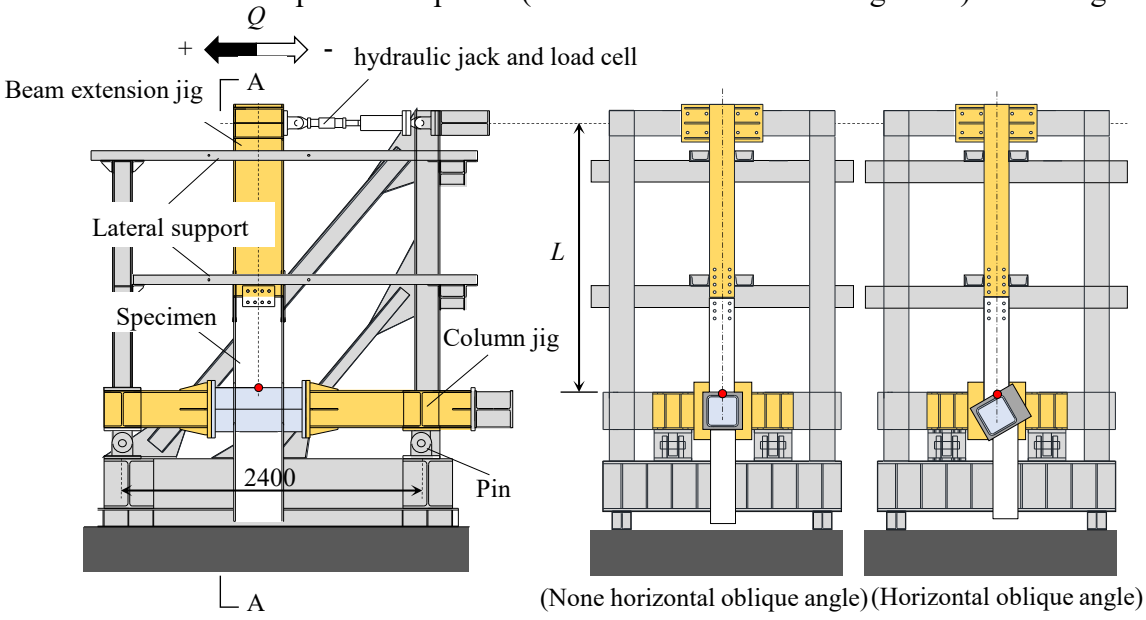

(a) Front view (b) A-A Cross-sectional view

Fig.2.12 Test setup.

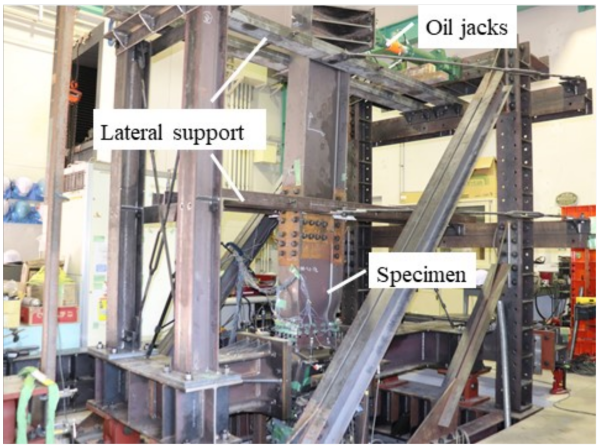

Photo. 2.3 Photographs of the setup.

Table. 2.4 Detail of beam-to-column connections.

No.	NS0	NS15	NS30	NS45	NS15E
Oblique angle Θ_H	0°	15°	30°	45°	45°
Detail of diaphragm (mm)	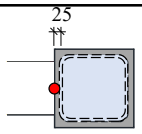	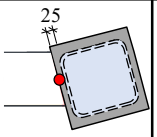	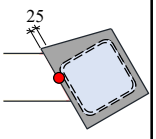	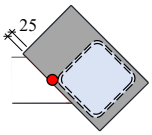	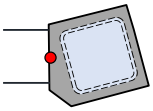
Span L (mm)	2175	2170	2154	2125	2170

which was defined as the hydraulic jack center to the beam-to-column connection, was approximately 2150 mm.

The measurement plan is shown in Fig. 2.13. Horizontal and vertical displacement transducers were installed on targets, which extend from the diaphragm (see Fig. 2.13). The absolute displacement measured from displacement transducers in the horizontal and vertical directions are represented by x_1-x_8 and y_1-y_8, respectively (Fig. 2.13(c)). Column and panel rotation angles, and beam rotation angle are defined as θ_{c+p} and θ_b, calculated using equations (2.7) - (2.8).

$$\theta_{c+p} = \frac{y_4 - y_3 + y_8 - y_7}{2(d_b - t_f)} \tag{2.7}$$

$$\theta_b = \frac{\Delta - \frac{x_3 + x_4 + x_7 + x_8}{4}}{L} - \frac{y_4 - y_3 + y_8 - y_7}{2(d_b - t_f)} \tag{2.8}$$

Here, d_b is the beam depth, and t_f is the flange thickness. The beam rotation angle θ_b was used as the controlled displacement for loading. The shear force Q was measured using a load cell attached to the hydraulic jack. Similar to the element tests, strain gauges were placed at beam ends to study strain distribution, as shown in Fig. 2.13(b) with black marks. Notably, strain gauges along the t-section were positioned 20 mm from the weld to mitigate welding effects.

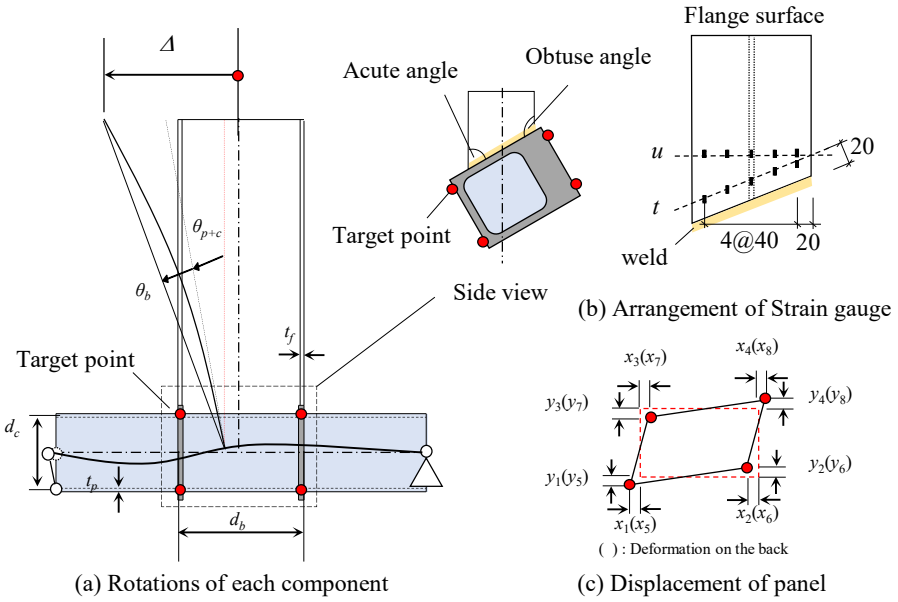

Fig. 2.13 Measurement plan (Length unit: mm).

2.4.3 Loading protocol

The loading protocol is shown in Fig. 2.14. Initially, the first loading level was kept within the elastic range of the beam-end connections to confirm elastic behavior, based on the material properties of the specimens. The amplitude of each loading level was 0.005 (elastic), 0.01, 0.015, 0.02, 0.025, and 0.03 rad, with each level repeated for two cycles. Due to the stroke limit of the hydraulic jack being reached at 0.03 rad, the specimens were then subjected to constant-amplitude cyclic loading at 0.03 rad until fracture after the increasing amplitude.

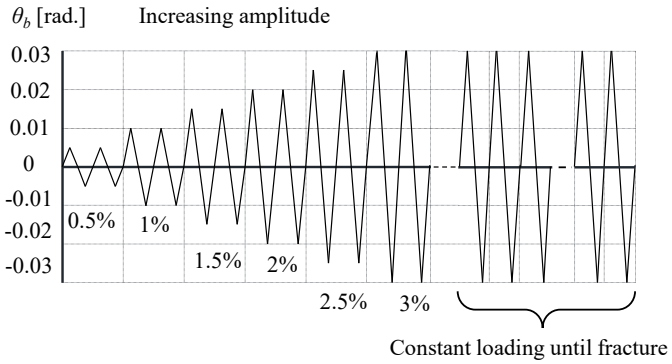

Fig. 2.14 Loading protocol.

2.5 Experiment results

This part will summarize the experimental results, evaluating the hysteretic curves, skeleton curves, fracture modes, strength deterioration of constant amplitude loading and strain distribution of beam end.

2.5.1 Hysteretic behavior and skeleton curves

Fig. 2.15 shows the hysteretic behavior of the NS specimens under increasing amplitude loading. The vertical axis represents the beam moment M, given as $M=L\cdot Q$, and the horizontal axis represents the beam rotation angle θ_b. The red lines in Fig. 2.15 show the calculated results of the elastic stiffness and the full plastic moment M_p. Comparing the hysteretic behaviors of the NS specimens, all exhibited stable hysteretic loops. For all NS specimens, the beams remained elastic until the 0.005 rad loading cycle. A decrease in stiffness was observed when M reached the full plastic moment M_p. The elastic stiffness and full plas-

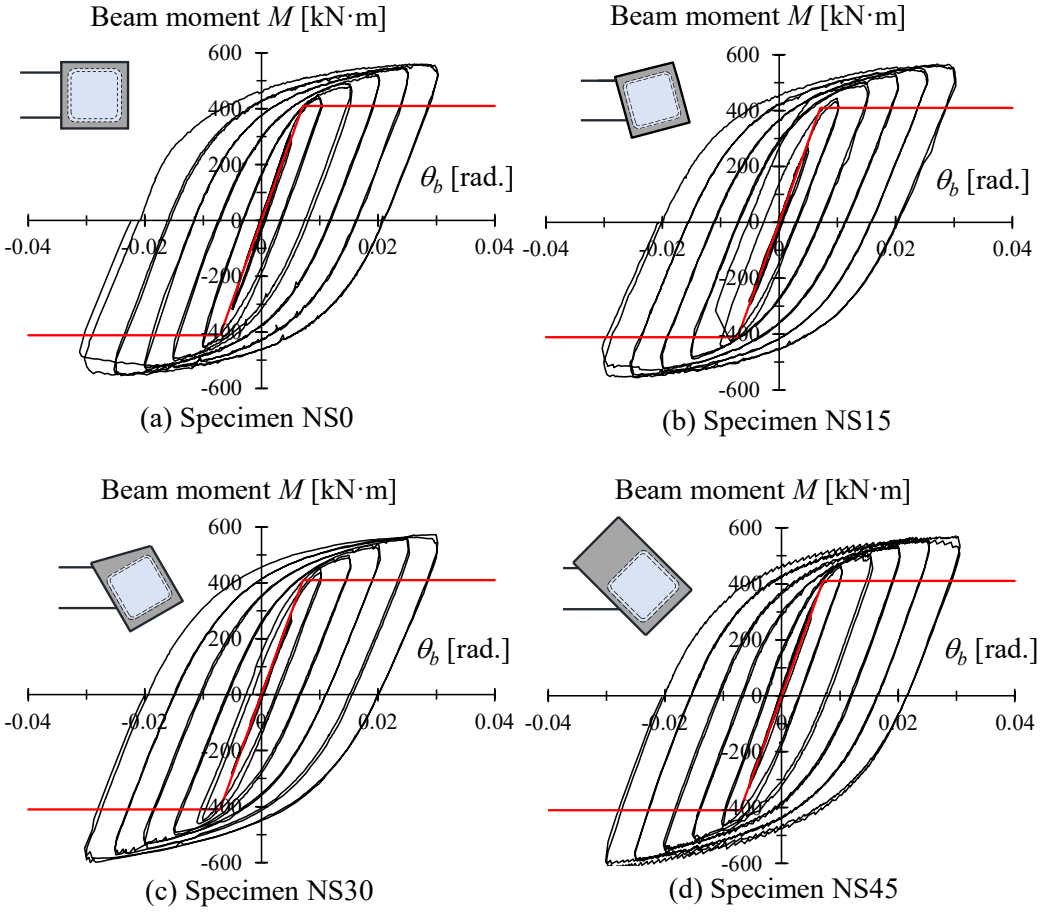

Fig. 2.15 Hysteretic curves of NS specimens under increasing amplitude loading.

tic moment were consistent with the calculated results. For all specimens, as beam rotation angle increased, the beam end moment continued to rise. However, local buckling occurred at the beam ends during the cycle at 0.03 rad loading amplitude, leading to a decrease in beam end moment. Notably, during the loading process of NS15 specimen, a slip occurred at the beam extension jig to the specimen joints during the negative loading of second 0.01 rad cycle, resulting in different behavior compared to the first 0.01 rad cycle. Furthermore, a comparison of the hysteretic curves for NS15E and NS0 specimen is shown in Fig. 2.16. NS15E Specimen also exhibited stable hysteretic curves, with initial stiffness and yield strength similar to those of NS0. That means the different of fabrication did not change the behavior of beam-to-column connection.

Skeleton curves were used to evaluate the elastic and plastic behavior of the specimens. The definition and extraction method of the skeleton curve are shown in Fig. 2.17(a), where $\Sigma\theta_b$ represents the cumulative beam rotation angles. Fig. 2.17(b) and (c) display the results of the skeleton curves extracted from Fig. 2.15 and 2.16. In the figure, different colors distinguishing the various specimens. Despite the differing horizontal oblique angles and fabrication methods, similar elastic and plastic behaviors were observed for all specimens.

The elastic stiffness, maximum strength, and the number of cycles to the damage state are summarized in Table 2.5. The elastic stiffness was determined using the least squares method for the 0.005 rad amplitude loading cycle. Notably, all specimens exhibited the same elastic stiffness and maximum strength. Combining these results, it can be concluded that an horizontal oblique angle has no significant effect on the timing of yielding and local buckling and does not influence the hysteretic behavior during the increasing-amplitude loading process.

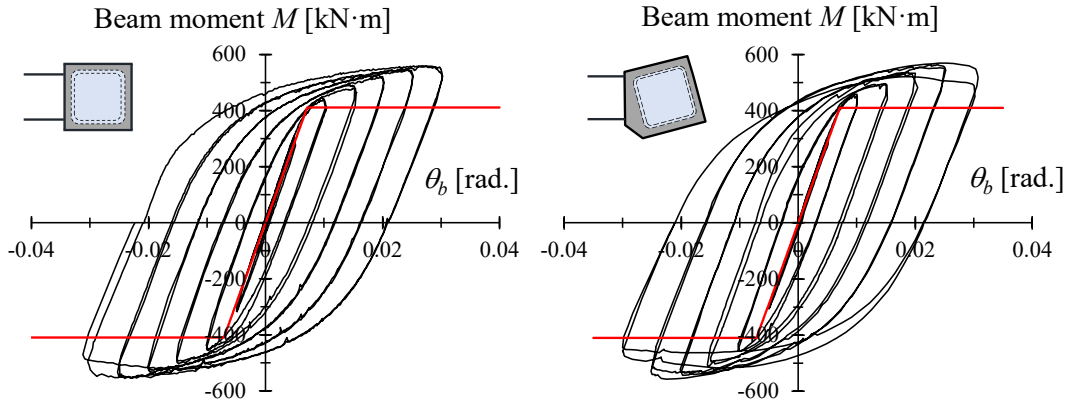

(a) Specimen NS0 (b) Specimen NS15E

Fig. 2.16 Hysteretic curves of NS0 and NS15E specimens.

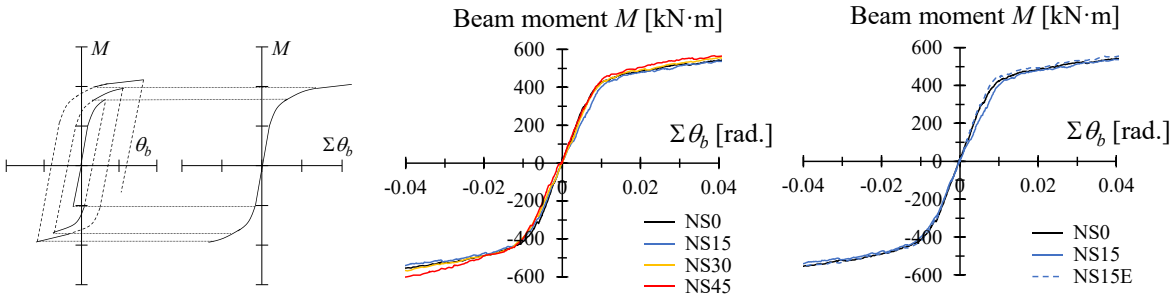

(a) Definition of skeleton curve (b) Skeleton curve of specimens (c) Different type of Θ=15°

Fig. 2.17 Hysteretic curves of NS series and NS15E specimens.

Table 2.5 Summary of experimental results.

Specimen	Stiffness exp. K_{exp} [kN/mm]	Stiffness cal. K_{cal} [kN/mm]	K_{exp}/K_{cal}	Max strength M_u [kN·m]	Cycles of damage state		
					Local buckling	Ductile crack	Timing of fracture cycle
NS0	13.1	12.2	1.07	559.2	0.03(2-)*	0.03(18+)	0.03(22+)
NS15	12.7	12.2	1.04	567.0	0.03(2-)	0.03(27+)	0.03(34+)
NS15E	13.0	12.2	1.06	570.1	0.03(1+)	0.03(22+)	0.03(33+)
NS30	12.0	12.5	0.96	571.5	0.03(1+)	0.03(25-)	0.03(32-)
NS45	13.2	12.9	1.02	572.0	0.03(1+)	0.03(24-)	0.03(29-)

*0.03(2-): Negative loading of the second cycle of 0.03 rad.

2.5.2 Plastic deformation capacity and fracture modes

The peak moment per cycle during loading is summarized in Fig. 2.18 to evaluate the deterioration of strength. The vertical axis represents the beam moment *M*, and the horizontal axis represents the number of loading cycles *N*. Different shapes in the black markers indicate specimens with various horizontal oblique angles, while the blue one represents the NS15E specimen with a different fabrication method. Due to COVID-19, the loading for specimens NS0 and NS15 were interrupted after the 20th cycle. After about one week loading resumed at the 21st cycle, the maximum beam moment increased due to strain aging. Notably, under constant amplitude loading, the deterioration of the maximum moment per cycle was similar for all specimens, regardless of oblique angle or fabrication method.

Table 2.5 compares the timing of cycles to fracture under constant amplitude loading. All specimens showed ductile crack initiation around the 22nd cycle and clearly fracture around the 30th cycle. The similar time of ductile cracks and fracture cycles indicates that the horizontal oblique angle and fabrication method has less impact on the plastic deformation capacity and deterioration trend of beam-to-column connections when the local buckling occurred.

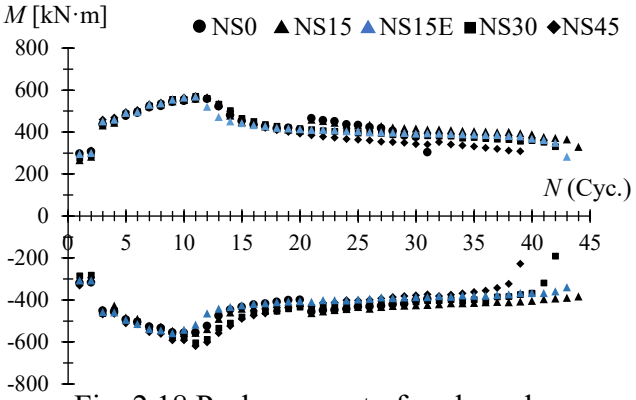

Fig. 2.18 Peak moment of each cycle.

Fracture mode of the specimens are shown in Photo 2.4. Annotations indicating the locations of maximum deformation due to local buckling at the beam ends (local buckling location). All specimens, except NS45, fractured at the locations of maximum deformation caused by local buckling. In NS45, ductile cracks initiated at the location of local buckling but extended toward the obtuse angle zone, clearly showing a difference between the fracture and the local buckling location in the side view of fracture photo (Photo 2.4(e)). Comparing the fracture modes in the element test, all specimens fractured at *u*-section. However, due to beam deformation concentrating at the local buckling locations during the constant amplitude loading, the fracture mode of specimens differed from that observed in the element tests. Comparing the local buckling location of each specimen, it was found that the local buckling location shifted closer to the beam end with the horizontal oblique angle increasing. Although different local buckling location did not significantly affect strength deterioration trend behavior, the horizontal oblique angle had a significant impact on the local buckling location.

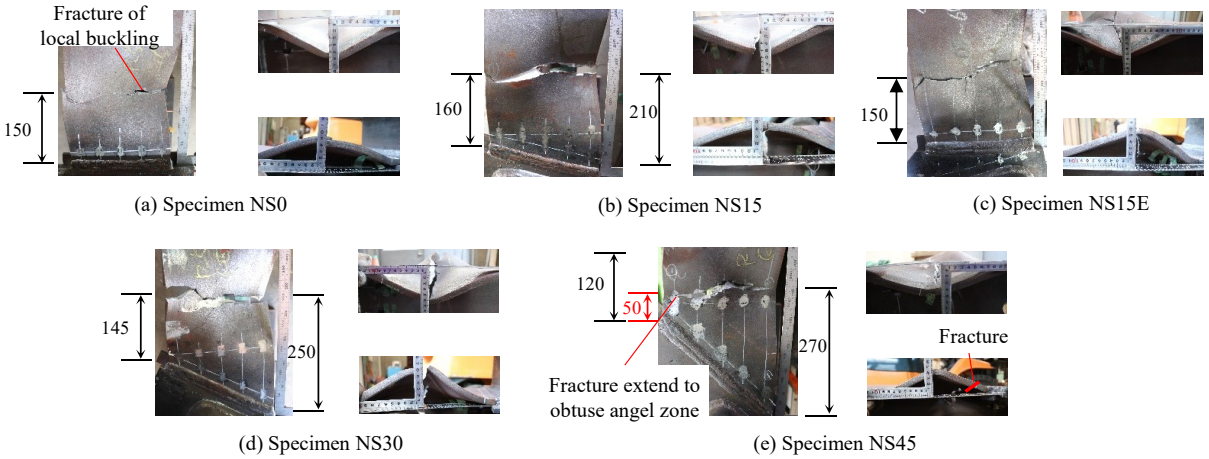

Photo 2.4 Fracture mode of the specimens.

2.5.3 Strain distribution of flange and developing process of the plastic field

The fracture photos of NS45 specimen(Photo 2.4(e)) indicate that crack development did not coincide with the location of maximum deformation caused by local buckling but extended into the obtuse angle zone. This phenomenon suggests potential strain concentration in the obtuse angle zone, similar to the results shown in the element tests in section 2.3.3. Therefore, evaluation of the deformation at the beam end is necessary.

Firstly, the deformation of the beam end was evaluated. Owing to cyclic loading, strain exhibited hysteretic behavior. The strain generated per cycle at the beam end was used to obtain the strain range D [15], as defined in Fig. 2.19. The figure shows an example of the strain history at θ_b = 0.005 rad. to 0.025 rad. The vertical axis represents strains measured from the strain gauges, and the strain range is calculated from the first loading cycles with amplitudes of 0.005, 0.02, and 0.025 rad. to avoid yielding (which occurs at an amplitude within the range of 0.01–0.015 rad.) and local buckling (at an amplitude of 0.03 rad.). The colors distinguish the different amplitudes. The strain range was calculated as $D = \varepsilon_{max}$-ε_{min}.

Fig. 2.20 shows the relationship between D and the position along the u- and t-section of the beam ends. Herein, when comparing the 0.005 rad. amplitude, all specimens exhibit the same strain range on the beam ends in elastic behavior. When the beam ends developed significant plastic deformation at the amplitudes of 0.02 and 0.025 rad, the D of Specimen S0 was concentrated at the edge of the flange (Fig. 2.20(a)), demonstrating a typical strain distribution from the beam to the SHS column connections as aforementioned [15]. Since NS15E and NS0 have the same beam end, the strain range of NS15E showed similar results with NS0, without indicating strain concentration (Fig. 2.20(b)). For S15 specimen, the strain of the acute angle zone along the t-section decreased at an amplitude of 0.025 rad (Fig. 2.20(c)),

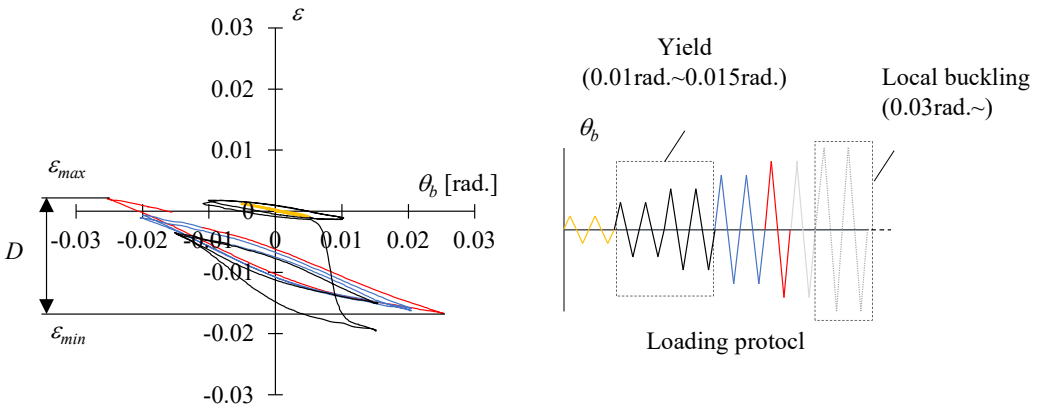

Fig. 2.19 Definition of strain range.

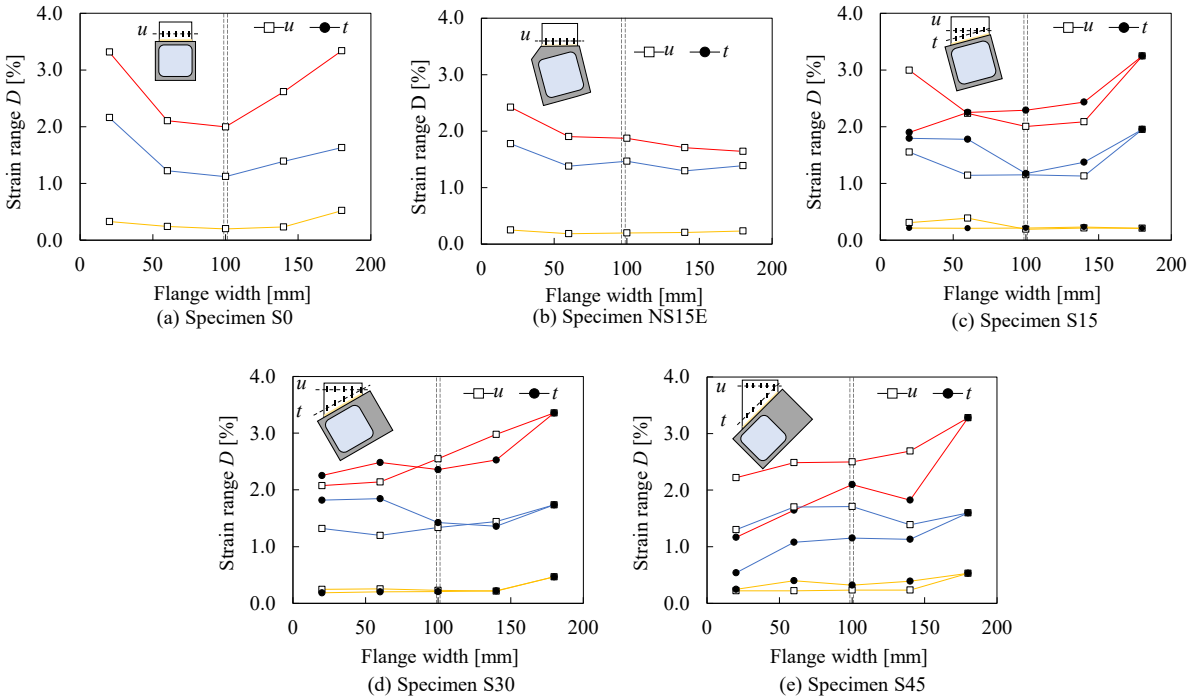

Fig. 2.20 Strain range of beam ends.

but the strain range D of the u-section was similar to that of S0 specimen. Therefore, in the beam-to-column connection with an oblique angle of less than 15°, no apparent difference in the D of S0 specimen was observed. As the oblique angle Θ increased, compared with the D in the obtuse angle zone, the D of S30 and S45 specimens in the acute angle zone of the beam end decreased significantly at amplitudes of 0.02 and 0.025 rad. (Fig. 2.20(d)(e)). This implies that strain concentration occurred in the obtuse angle zone. Specifically, as shown in the t-section of S45 specimen (Fig. 2.20(e)), the value of D of the obtuse angle zone is approximately three times that of the acute angle zone, explaining the reason that the crack proceeds to the obtuse angle zone rather than the maximum deformation in the local buckling zone. In addition, for all specimens with oblique angles, particularly S45 specimen, in the acute angle zone of the beam end, the value of D of the u-section gradually exceeds that of the t-section as the beam rotation increases. Therefore, although the acute angle zone is subjected to the largest beam moment at the beam end, the strain range indicates that it is extremely difficult for the acute angle zone to fracture.

Furthermore, the location of the strain concentrations was consistent with the element test results. However, the fracture mode of the specimens differed from that in the element test. For S45 specimen, the crack originated at the center of the local buckling zone, in con-

trast to the fracture mode of L45 specimen (element test), which developed at the obtuse angle zone. Thus, local buckling caused the fracture mode of the beam-to-column connections to differ from that observed in the element test. In other words, in the case without local buckling, premature fracture might appear at the obtuse angle zone of the beam end.

To further analyze the impact of horizontal oblique angle on the elasto-plastic deformation of the beam end, the plastic field development during the yielding phase at the beam end will also be evaluated. Since NS15E and NS0 have the same shape at beam end , only NS0 specimen will be compared here. Fig. 2.21 shows the skeleton curves and yield

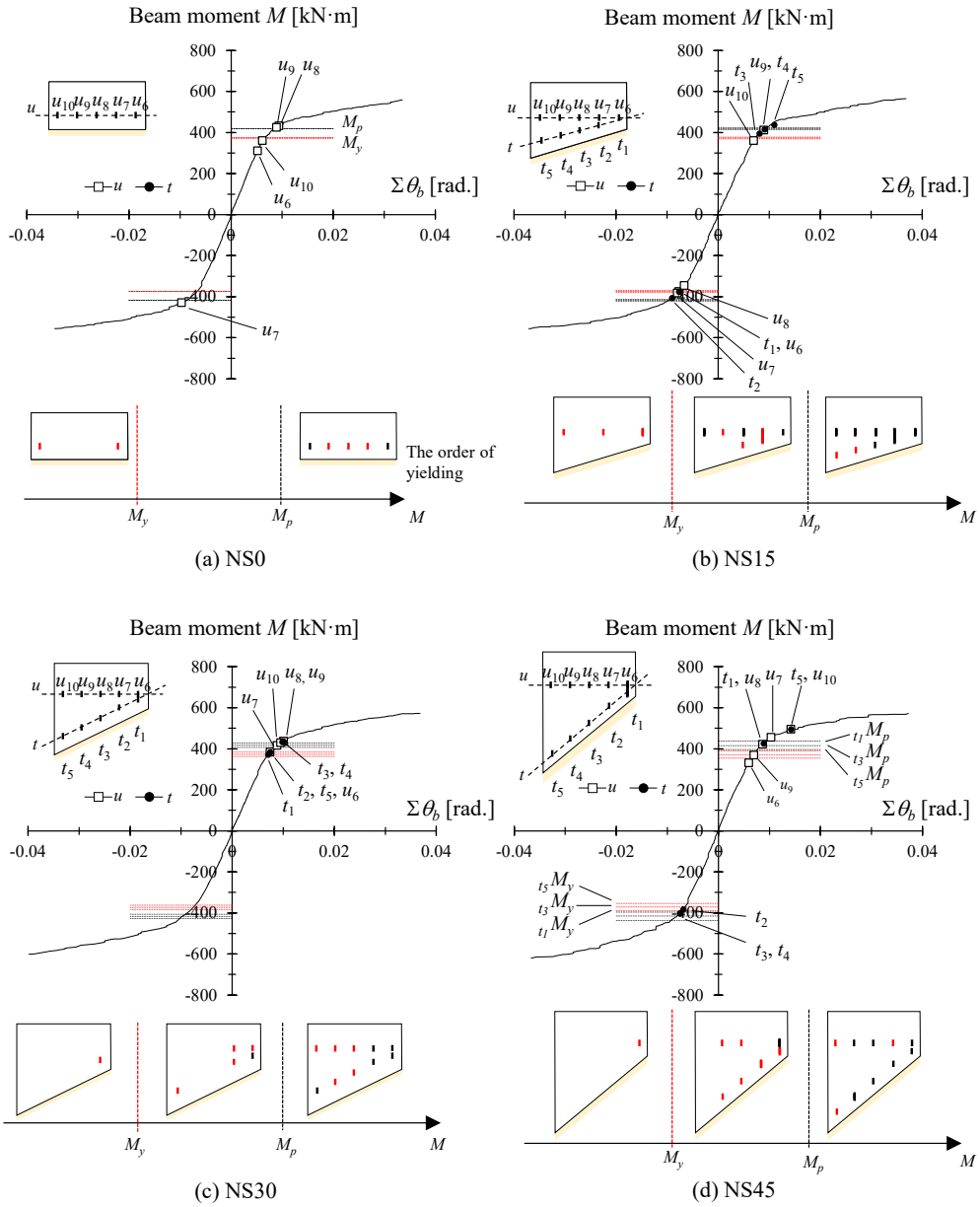

Fig. 2.21 Effect of oblique angle on plastic field development.

strengths at each position of the *u*- and *t*-section at the beam ends. Red and black dotted lines represent the beam yield moment M_y and full plastic moment M_p of the beams, respectively. Because the shapes of the beam ends were irregular, the yield and full plastic moments of the beam ends differed in each section. Subsequently, M_y and M_p were calculated using three sections: the center of the beam (section t_3), acute angle zone (section t_5), and obtuse angle zone (section t_1), as shown in Fig. 2.21(d). The plots of the skeleton curves are presented as M when the values of the corresponding strain gauges reach the yield strain obtained from the material test. The sequence of timing is summarized in the skeleton curves of each specimen. The results from the skeleton curves provide an overview of the development process of the plastic field at the beam ends represented in three phases: before M_y, between M_y and M_p, and after M_p. In the case of S0 specimen, the edges of the flange plasticized before M_y and gradually extended toward the center of the beam as M increased. The progression of plastic development is consistent with the results obtained in the literature[15]. In contrast to that of S0 specimen, the yielding of S15, S30, and S45 specimens first occurred in the obtuse angle zone and then in the acute angle zone.

2.6 Conclusions

These experiments investigated the effects of horizontal oblique angles on the elasto-plastic behavior of SHS steel columns with H-beam-end connections under cyclic loading. The element test were conducted to predict the critical section of a beam flange at an horizontal oblique angle. Following the results of the element test, a full-scale experiments of beam-to-column connections were conducted to clarify the difference in behavior between the element tests and the full-scale experiments. The seismic behavior of the beam-to-column connections and the strain distribution at the beam ends were clarified.

The primary conclusions are as follows:

(1) In the element tests, the failure section calculated using the von Mises criterion was verified based on the results of the tensile tests. By analyzing the failure modes of all the specimens and the strain distribution in the irregular part near the weld, it was found that larger oblique angles caused strain concentration in the obtuse angle zones, causing the specimens to premature fracture.

(2) In the full-scale experiments, the specimens exhibited stable hysteresis behavior. Moreover, upon analyzing the skeleton curves of the beam rotation and timing of local buck-

ling, the results indicated that oblique angles had small effect on the hysteretic behavior of beam-end connections.

(3) Comparing the failure modes, timing of the fracture cycles, and local buckling positions, S0, S15, and S30 specimens fractured at the maximum deformation of the local buckling zone. The crack in S45 specimen started at the center of the local buckling zone and then extended to the obtuse angle zone. With increasing oblique angles, although the local buckling position moved closer to the beam end, it did not affect the strength deterioration behavior. In addition, comparing the timing of the fracture cycles, the fatigue life of connections with oblique angles was no worse than that of connections without oblique angles in the experiments.

(4) The strain range at the beam ends was analyzed. S15 specimen showed no apparent strain concentration, in contrast to S0, S30, and S45 specimens , which showed a significant tendency of strain concentration at the obtuse angle zone, similar to the results of the element test. For S45 specimen, the strain concentration led to a change in crack development. This fracture mode also proved that local buckling caused the fracture mode to differ from that observed in the element test. As a result, in the case without local buckling, premature fracture might occur at the obtuse angle zone of the beam end.

(5) Compared to the fabrication method of NS15E with an extended diaphragm, the seismic performance of the specimen is same as that of the specimen without an horizontal oblique angle. To avoid premature fracture caused by strain concentration in large horizontal oblique angle connections, it is recommended to use the extended diaphragm fabrication method for specimens with oblique angles above 15 degrees.

References

[1] Japan Steel Constructors Association (JSC). Standard Detail of Steel Structural Frame. Japan Steel Structure Journal Co., Tokyo, 2016 (in Japanese).

[2] H. Kaibara et al. A Study on Bearing Capacity and Deformation of Panel Zones Subjected to Shear Loading from Oblique Directions: Square Rectangular Steel Tubular Columns. Summaries of technical papers of annual meeting AIJ (Kyushu branch) 32 (1991) 217–220 (in Japanese).

[3] R. Arakida, I. Chan, Y. Koetaka, Full plastic strength of square hollow section panel zone under arbitrary directional shear force. J. Struct. Constr. Eng. AIJ 84 (2019) 85–95 (in Japanese).

[4] R. Arakida, T. Umeda, Full plastic strength of beam-column joint panel of box column built up by partial penetration welding at the corner seams. J. Struct. Constr. Eng. AIJ 89 (2024) 202-211 (in Japanese).

[5] Y. Wang et al. Cyclic behavior of panel zone in beam-column subassemblies subjected to bidirectional loading. J. Constr. Steel Res. 143 (2018) 32–45.

[6] Y. Wang et al. Elastoplastic behavior of week-panel beam-column joints with RC slabs under bidirectional loading. J. Constr. Steel Res. 168 (2020) 105880.

[7] I. Chan, Y. Koetaka, Numerical model for 3D steel moment frames with H-shaped beams and hollow-section columns under multi-directional seismic ground motions. Eng. Struct. 246 (2021) 112730.

[8] Y. Bai et al. Bi-directional seismic behavior of steel beam-column connections with outer annular stiffener. Eng. Struct. 227 (2021) 111443.

[9] R. Nie et al. HSS steel corner column to H-beam joints under cyclic bidirectional loadings: Experiment, numerical modeling, and calculation. J. Constr. Steel Res. 192 (2022) 107239

[10] K. Inoue, K. Suita, Building steel structure-theory and design. kajima institute publishing CO., Tokyo, 2007. (In Japanese)

[11] Japanese Standards Association (JSA), Ferrous Materials & Metallurgy I-2019: Metallic materials-tensile testing (JIS Z 2241), JSA, Tokyo, 2018.

[12] Japanese Standards Association (JSA), Solid wires for MAG and MIG welding of mild steel, high strength steel and low temperature service steel (JIS Z 3312), Japanese Indus-

trial Standards Committee, Tokyo, 2009.

[13] Architectural Institute of Japan, AIJ Recommendation for Design of Connections in Steel Structures, Maruzen, Tokyo, 2021. (In Japanese)

[14] T. Ishii, S. Kikukawa, K. Morita, K. Takanashi, Experiment Study on Fracture Behavior of Beam-to-column Connection. Proceedings of Constructional Steel 6 (1999) 87–102 (in Japanese).

[15] R. Okamato Elastic stress distribution of beam flange connected to a box type steel column to H-shaped beam connection using Finite Element method. J. Struct. Constr. Eng. AIJ 474 (1995) 171–179. (in Japanese).

[16] Y. Dong et al. Cyclic Behaviors of SHS Columns in Low Cycle Fatigue Tests, Journal of Earthquake Engineering (2022) 1–28.

CHAPTER 3

Cyclic loading test of beam-end connections with vertical oblique angle

3.1 Introduction

As an earthquake-prone country, Japan has widely adopted steel frame structures. In steel frame structures, beam-to-column connections bear the highest bending moments, and under the strong column-weak beam design criterion, the beam ends frequently experience damage during earthquakes. The introduction in Chapter 1 describes various complex beam-column connections, noting that different shapes of beam ends result in varying failure sections[1-4]. Some cases in practices, beams and columns must be connected at a vertical oblique angle. Unlike beams connected perpendicularly to columns, the seismic performance and failure sections of beam-to-column connections with oblique angle are not yet well under-

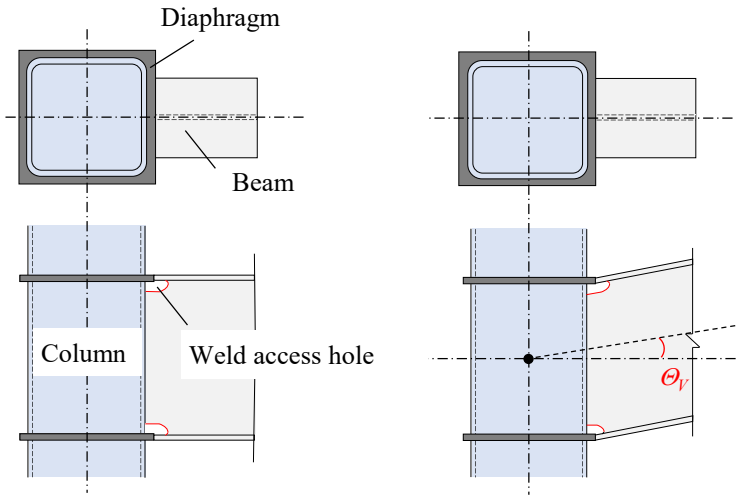

(a) Through diaphragm method. (b) Connection with vertical oblique angle Θ_V

Fig.3.1 Different type of beam-to-column connections.

stood. Notably, such beam-to-column connections were already in use as early as 1994, as mentioned in Chapter 1. According to the "Standards Detail for Steel Frame Structures[5] and Design Guide of Steel Frame Structures Connections Details [6]" in Japan , beams with vertical oblique angles are welded to columns by cutting the beam ends to fit oblique angle, resulting in asymmetrical beam-end shapes.

In Chapter 2, studies on beam-to-column connections with horizontal oblique angles determined the failure section based on the von Mises criterion. Experimental studies showed that horizontal oblique angles do not affect hysteretic behavior but do influence strain distribution at the beam end. For vertical oblique angles, the beam ends have similar shapes; however, the upper and lower flanges of the beam are unequal due to the asymmetry at the beam end. This asymmetry makes it challenging to determine the beam span. In addition the connection with vertical oblique angle between the beam and column affects the details of the beam-to-column connection. For example, when beam flange welded to the diaphragm, the oblique angle affect the welding details. Previous studies [7] have indicated that excessive bevel angles can reduce weld strength. Different fabrication methods for beam-to-column connections also create different problems. Beam-to-column connection with the weld access hole method, the oblique angle alters the shape of the weld access hole. In the non-weld access hole method, the angle creates a gap between beam web and diaphragm. The potential impact of these issue on the seismic behavior of beam ends remains unclear. Therefore, further experimental studies on beam ends are necessary to provide insight into their elastoplastic behavior and failure sections.

To address the issues mentioned above, this chapter presents an analysis of beam-to-column connections with vertical oblique angles using mechanism analysis and full-scale experiments. Section 3.2 presents a mechanism analysis of the beam ends, explains the prediction of the failure section, and defines the modified span of the beam by using theoretical approach. Section 3.3 describes the full-scale experiments conducted to determine the hysteretic curves, failure modes, plastic deformation capacity, and strain distribution. Section 3.4 discusses the experimental results. Finally, Section 3.5 presents the concluding remarks.

3.2 Mechanism analysis of connections with vertical oblique angle

The mechanism of beam-to-column connections with vertical oblique angles differs from that of the conventional beam-to-column connections. To accurately determine the failure section of beam-to-column connections, it is necessary to conduct a mechanism analysis of each section of the connection.

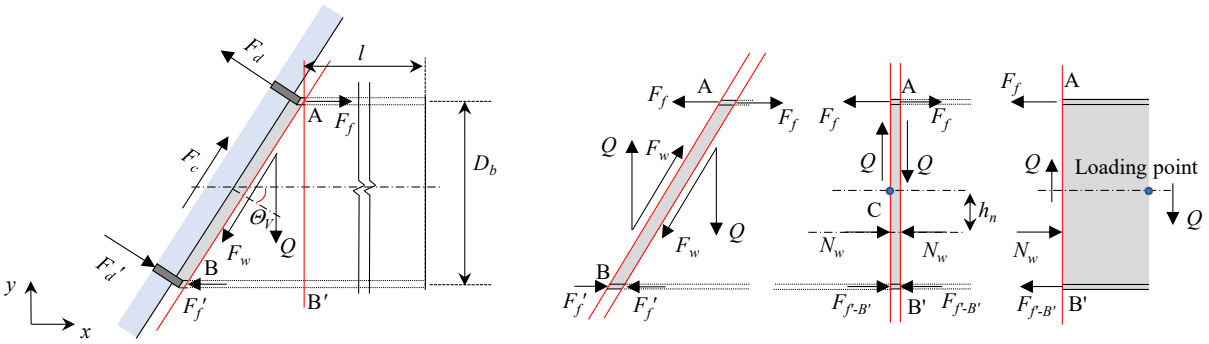

(a) External force balance for column (b) Internal force diagram for AB & AB' sections

Fig.3.2 Mechanisms of force transmission at beam end.

An analysis of the force transmission mechanisms at the beam end is illustrated in Fig. 3.2. For a beam-to-column connection with a vertical oblique angle, two potential failure sections can be anticipated: (1) the section at the beam end, labeled section AB, and (2) the vertical section of the beam end, labeled section AB'. To analyze the internal forces of the two sections, an *xy*-coordinate system was established and the beam end was segmented into three sections. First, an infinitesimal interval of the weld part between the column and beam was segmented for analysis, as shown in Fig. 3.2(a). In the column part, by assuming that the force exerted on the weld section of the web at the beam-to-column connection acts interactively along section AB and by considering the moment balance at points A and B, Eqs. (3.1) and (3.2) can be obtained as shown below.

$$F_d = \frac{Ql\cos\Theta_V}{D_b} + Q\sin\Theta_V \tag{3.1}$$

$$F_d' = \frac{Ql\cos\Theta_V}{D_b} \tag{3.2}$$

Here, l represents the distance between the welding point of the beam's upper flange and loading point (length of upper flange); D_b is the depth of the beam; Q denotes the shear force; F_d and F_d' are the internal forces in the upper and lower diaphragms, respectively. By establishing the external force balance equations in both the x and y directions simultaneously, the axial force of the column F_c can be determined as follows:

$$F_c = Q\cos\Theta_V \tag{3.3}$$

Subsequently, the beam was further segmented into microscopic sections AB and AB', as shown in Fig. 3.2(b). An internal force analysis was performed on section AB, and the moments at the points A and B were calculated. This allowed the determination of the internal forces at the upper flange F_f and lower flange F_f', as shown in Eqs.(3.4) and (3.5).

$$F_f = \frac{Ql}{D_b} + Q\tan\Theta_V \tag{3.4}$$

$$F_f' = \frac{Ql}{D_b} \tag{3.5}$$

From the results of the internal forces F_f and F_f', it is evident that the internal forces in the upper and lower flanges are unequal. The internal force in the upper flange is greater than that in the lower flange, which creates an opposite fictitious axial force in the web, expressed in the x direction. This allows the direction of the shear force Q to be altered to align with the section AB. At the same time, in the section AB', considering the moment at point B', the moment generated by the internal force in the upper flange is deduced to be greater than the external moment. Consequently, the resultant force in the y direction of the web requires an opposing force to produce a moment satisfying the equilibrium condition. Let this force be denoted as N_W and its distance from the midline of the beam is h_n. If the internal force at the lower flange is $F_{f\text{-}B'}$, then by considering the moment at point C, Eq. (3.6) can be obtained as

$$F_f \frac{D_b}{2} + F_{f-B'} \frac{D_b}{2} + N_w h_n = Ql \tag{3.6}$$

Considering the internal force balance in the x direction, as indicated in Eq. (3.7), $F_{f\text{-}B'}$ can be expressed as shown in Eq. (3.8).

$$F_f = F_{f-B'} + N_w \tag{3.7}$$

$$F_{f-B'} = \frac{Ql}{D_b} + Q\tan\Theta_V \left(1 - \frac{D_b}{\frac{D_b}{2} - h_n}\right) \tag{3.8}$$

Based on the boundary conditions of , it can be deduced that $1 - \frac{D_b}{\frac{D_b}{2} - h_n}$ <0; hence, $F_{f\text{-}B'}$ is less than F_f'. Thus, the failure mechanism at the connection can be estimated as follows: the beam failure is initiated at the upper flange at point A, followed by failure at point B at the lower flange, and finally at point B'. Therefore, it can be concluded that the failure section of the beam is section AB. When defining the span of the beam, the midline length L, as expressed in Eq. (3.9), should be used.

$$L = l + \frac{D_b \tan\Theta_V}{2} \tag{3.9}$$

3.3 Test program of beam-to-column connections

Full-scale tests of beam-to-column connections with vertical oblique angle were conducted, including verification of the results based on the Mechanism analysis in Section 3.2.

3.3.1 Test specimens

Fig. 3.3 shows an outline of a specimen with a vertical oblique angle, composed of a built-up H-section beam and a cold-rolled square hollow section (SHS) column. The columns were made of BCR295 steel (minimum nominal yield strength of 295 N/mm^2 and tensile strength of over 400 N/mm^2) and had dimensions of 350 × 350 × 16 (depth ×width × plate thickness). The beams were made of SN400B steel (minimum nominal yield strength of 235 N/mm2 and nominal tensile strength of over 400 N/mm^2) and had dimensions of BH-500×200×9×19 (depth × flange width × web thickness × flange thickness). The beam flange width-thickness ratio of the flange was 5.3, which satisfied the requirement for preventing local buckling [8]. The beams and columns were connected using through diaphragm method. To maintain the elasticity of the diaphragm, it was made of SN490C steel (minimum nominal yield strength of 325 N/mm^2 and nominal tensile strength of over 490 N/mm^2) and had a thickness of 28 mm. In accordance with the AIJ Recommendation for Design of Connections in Steel Structures [8], the diaphragms were extended up to 25 mm from the column face welded to the beam flange, a full-penetration weld was utilized at the connection between the diaphragms and beam flanges. For the connection between beam web and column, a fillet weld was used.

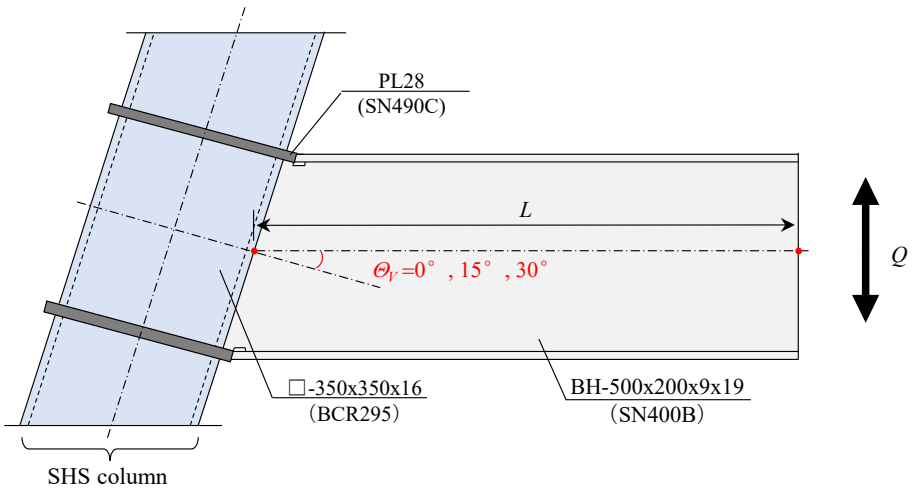

Fig. 3.3 Specimen with vertical oblique angle Θ_V.

Six specimens were prepared to investigate the effect of vertical oblique angles on the seismic behavior of the connections. The main parameter for the analysis was the vertical oblique angle. Specimens without oblique angles were also prepared. Additionally, owing to the variation in the vertical oblique angles, the specifications of the beam-to-column connections at the beam ends varied, which affected the strain distribution of the beam-to-column connections [9]. Furthermore, the effects of weld access holes were investigated. The six specimens included three specimens with (V series) and three without (VN series) weld access holes, with each series having vertical oblique angles of 0°, 15°, and 30°. Table 3.1 presents the parameters of each specimen. The lengths of the upper and lower flanges varied depending on the oblique angle, and the length of the span was approximately 3000 mm for all specimens. The weld details of the connections are shown in Fig. 3.4. To ensure appropriate specifications and quality of the connections, they were designed by a qualified fabricator in Japan and satisfied the specifications for the design of connections mentioned in Standard detail of steel structural Frame of Japan [5-6]. For standard specimens (V0, VN0), the groove angle of the beam flange was 35°. However, in V30 and VN30, the groove angle would result in an excessively large angle at the bevel angle, which can decrease the weld strength [7]. Therefore, an inner bevel angle was used to address this issue. Moreover, for the VNS30 specimens, gaps inevitably occurred at the ends of the beam web, which were treated with filled welding, as shown in Fig. 3.4(f). To confirm the strength of materials, all components were tested according to the JIS Z2241 standard [10], and the results are listed in Table 3.2.

Table 3.1 Parameters of beam-to-column connections.

Oblique angle θ	0°		15°		30°	
No.	V0	VN0	V15	VN15	V0	VN30
Weld access hole	With	Without	With	Without	With	Without
The detail of connections	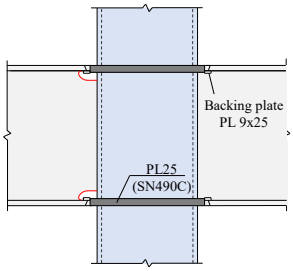		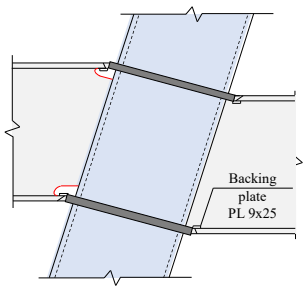		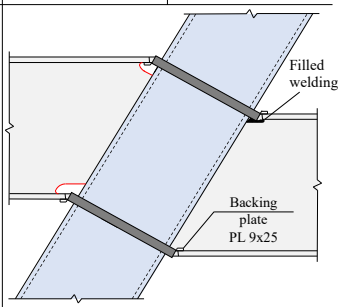	
Span L [mm]	3025		3005		3024	

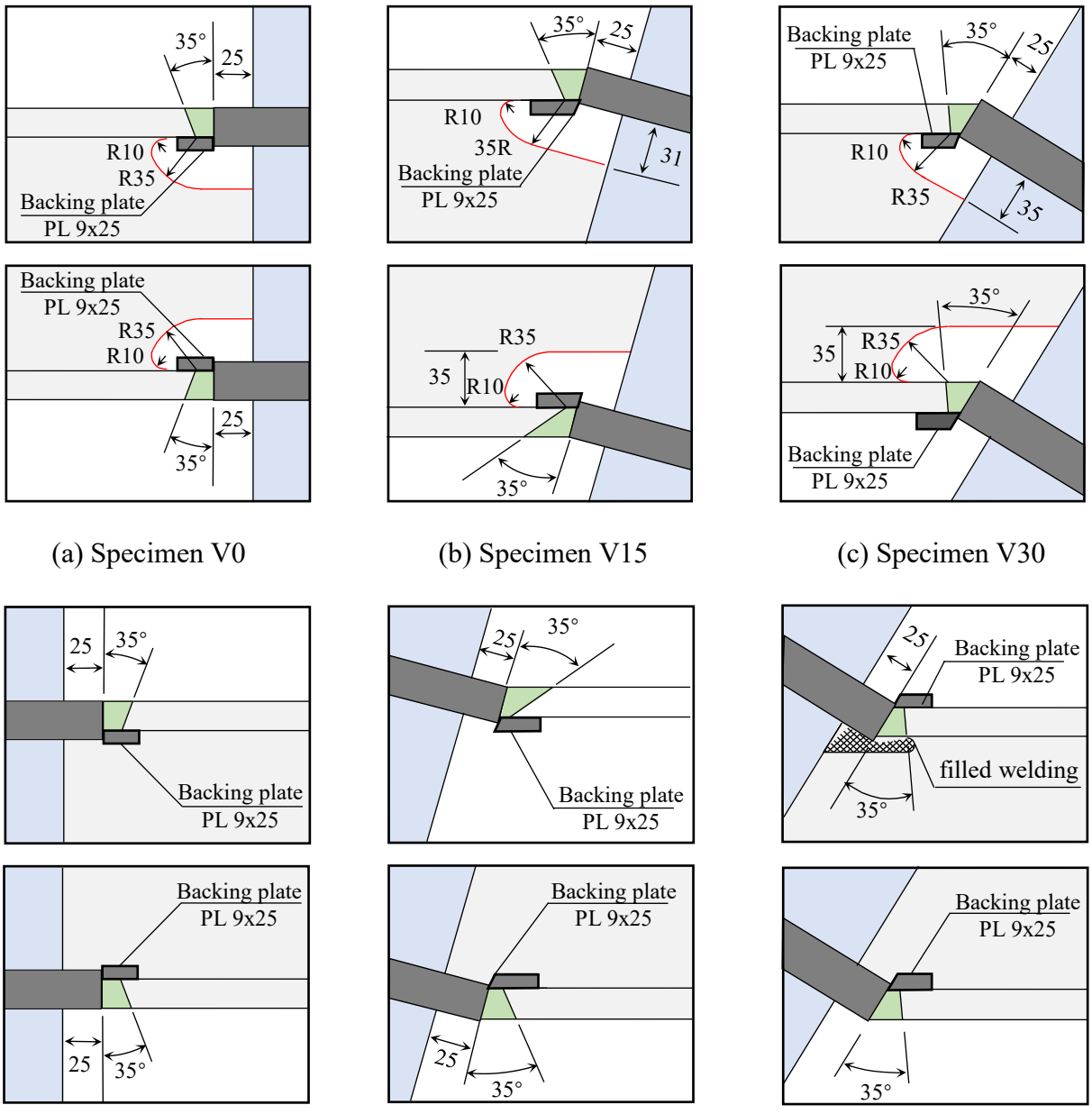

(a) Specimen V0 (b) Specimen V15 (c) Specimen V30

(d) Specimen VN0 (e) Specimen VN15 (f) Specimen VN30

Fig. 3.4 Details of the beam-to-column connections with vertical oblique angle.

Table 3.2 Properties of materials

	Steel type	Thickness t [mm]	Yield strength σ_y [MPa]	Tensile strength σ_u [MPa]	*Y.R.* [%]	*E.L.* [%]
Beam flange	SN400B	19	309	443	70	28
Beam web	SN400B	9	333	457	82	29
Column	BCR295	16	366	474	77	40

Note: *Y.R.*: Yield ratio, *E.L.*: Elongation

3.3.2 Measurement plan and setup

The test setup is shown in Fig. 3.5, where the colored parts represent the specimen. Photo 3.1 depicts the test setup for specimen V30. Each specimen was shaped as a cross-structure between a column and two beams on the left and right sides. Following the setup design method used in the setup of Chapter 2,the columns were appropriately set at an oblique angle inclined to the vertical axis to represent the vertical oblique angle of the beam, whereas the beams were set in the horizontal direction. For a given column, one side of the specimen was first tested and then the other side of the specimen was loaded.

The ends of the column were fixed to the reaction frame using upper and lower fixtures. At the upper fixture, two hydraulic oil jacks were attached to the reaction frame to provide a restraining force in the vertical direction. The beams were extended to 3000 mm using a beam jig, and the end of the beam jig was connected to a hydraulic oil jack. A load cell was set on top of the hydraulic oil jack for measuring the shear force. In addition, lateral supports were installed at the middle of the beam span and near the hydraulic oil jack for preventing the out-of-plane deformations. The upper fixture was not directly attached to the reaction frame for specimens with vertical oblique angles. Hence, the horizontal gap between the upper fixture and reaction frame was filled using adjustable jigs and PC steel bars.

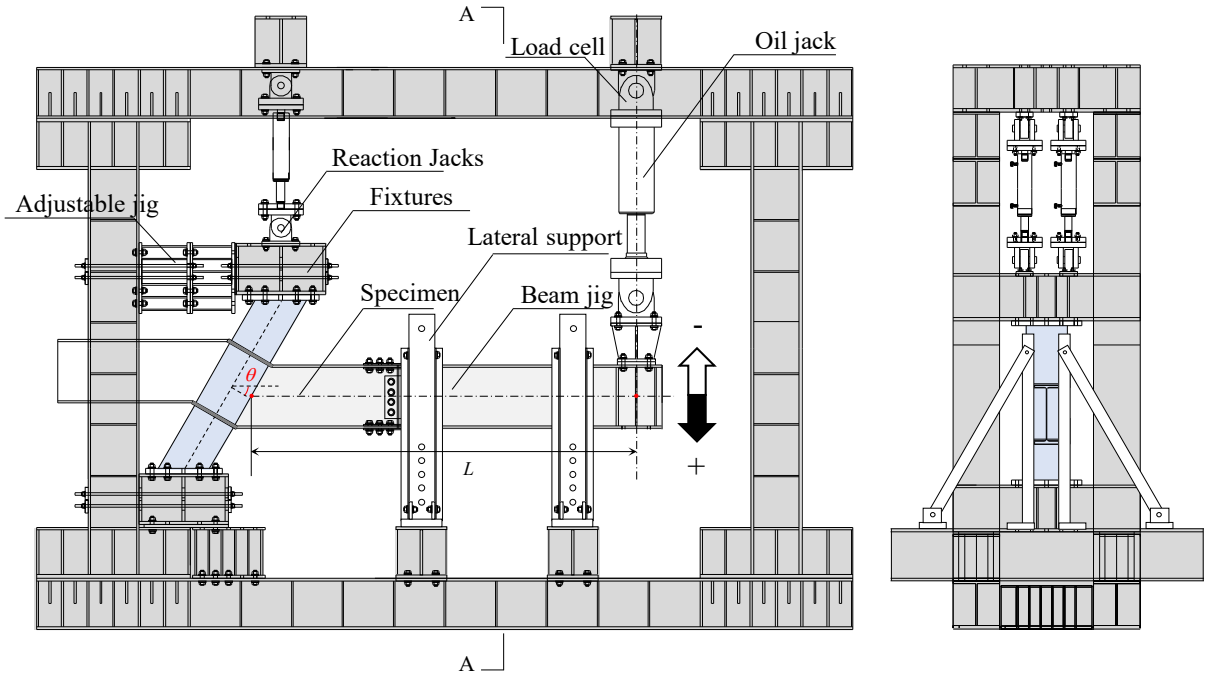

(a) Front view (b) A-A Cross-sectional view

Fig. 3.5 Details of the beam-to-column connections with vertical oblique angle.

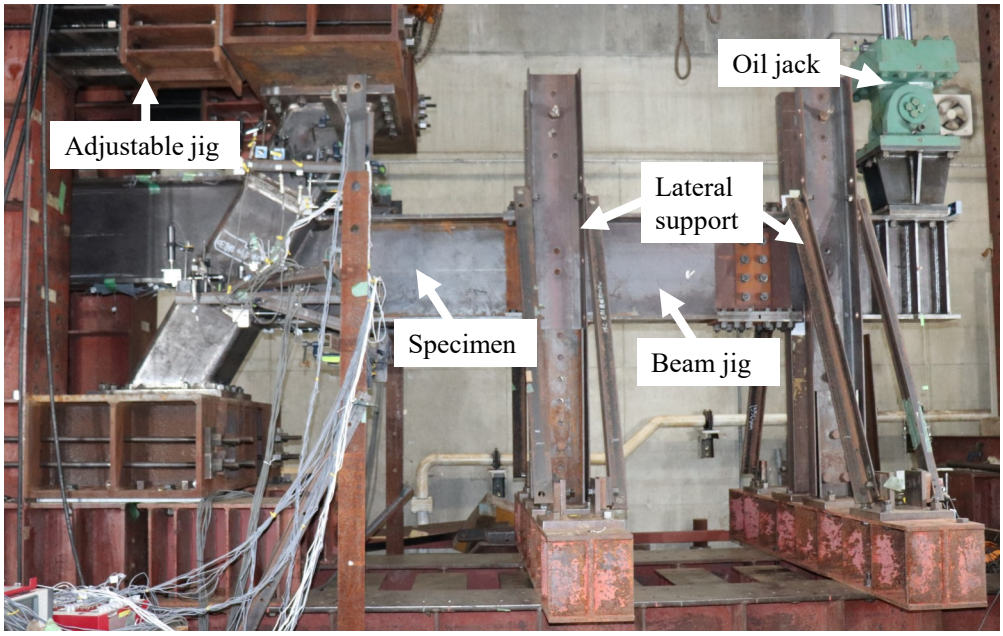

Photo 3.1. Photo of the test setup (V30).

The measurement plan is illustrated in Fig. 3.6. The red circles in the figure indicate the target positions of the displacement transducers. The targets were attached to the sides of the diaphragms to measure the absolute displacements x_1-x_8, y_1-y_8 in the horizontal and vertical directions, respectively. Displacement Δ was the absolute displacement measured from the center of the beam depth, which was provided by the hydraulic oil jack. The beam rotation angle was calculated using.

$$\theta_b = \frac{\Delta - \frac{y_3+y_4+y_7+y_8}{4}}{L} + \frac{\frac{x3-x4+x7-x8}{2} + (D_b - t_f)\sin\Theta_V}{(D_b - t_f)\cos\Theta_V - \frac{y_3-y_4+y_7-y_8}{2}} - \tan\Theta_V \qquad (3.10)$$

where D_b represents the beam depth and t_f represents the beam flange thickness. The vertical shear force Q was measured using a load cell set on the hydraulic oil jack. The beam rotation angle was used as a control value for the loading. The downward direction was defined as the positive loading direction for both the beam rotation and shear force.

The arrangement of the strain gauges were used to investigate the strain distributions at the beam ends is presented in Fig. 3.6(c). In this figure, the positions of the strain gauges on the beam flanges are represented by black triangles, and those on the beam web are represented by black rectangles. The strain gauges were arranged along (1) the oblique section parallel to section (AB), which was offset 30 mm from the column face, and (2) the vertical section (AB'), which is perpendicular to the beam flanges and passes through a point 70 mm

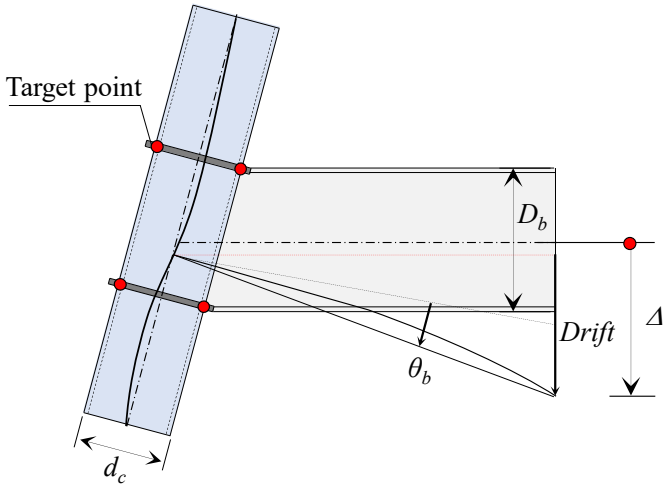

(a) Rotations of each component

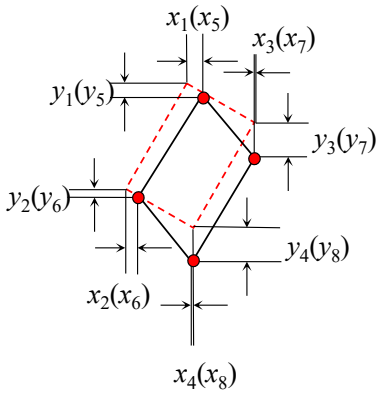

( ) : The target deformation at the back

(b) Displacement of panel

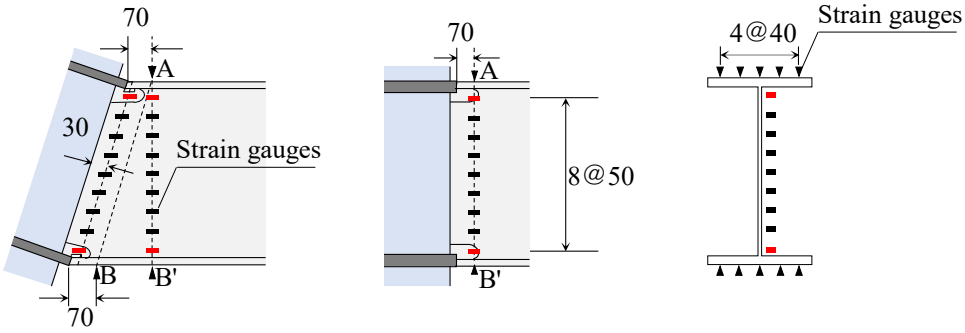

(c) Arrangement of Strain gauges

Fig. 3.6 Measurement (Length unit: mm).

from the edge of the upper diaphragm. Strain gauges marked in red were attached only to the series of NS specimens because of the lost section of the beam web in the case of specimens with a weld access hole.

3.3.3 Loading protocol

The loading protocol is shown in Fig. 3.7, which is the same as that used in Chapter 2. Based on calculations using the material properties of the specimens, the full plastic rotation angle of the beam, denoted as ${}_p\theta_b$, was 0.0057 rad. The first loading level was maintained in the elastic range to confirm the elastic behavior. The amplitude of each loading level was set to 0.005 (elastic), 0.01, 0.015, 0.02, 0.025, and 0.03 rad. Each level was repeated for two cycles. The stroke of the hydraulic oil jack reached its limit when the loading amplitude reached 0.03 rad, and therefore, the specimens were subjected to a constant-amplitude (0.03 rad) cyclic loading until a fracture occurred in the connections or the peak strength of each

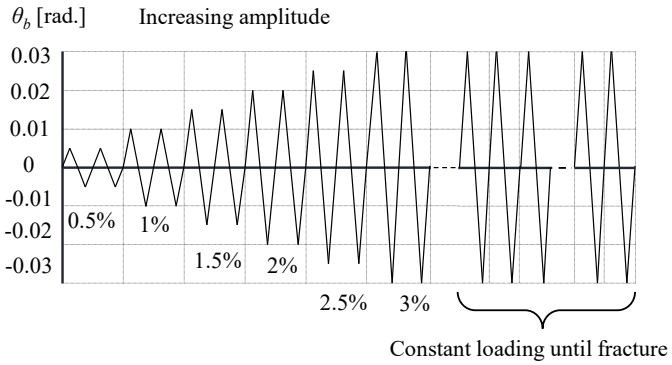

Fig. 3.7 Loading protocol.

cycle decreased by more than 20% of the maximum strength measured in the test.

3.4 Experimental results and discussion

The hysteretic curves, elastic stiffnesses, ultimate strengths, and failure modes were evaluated in the experiments. The experimental results are discussed below.

3.4.1 Hysteretic behavior and damage to specimens

The hysteretic curves obtained from these experiments are shown in Fig. 3.8. The vertical axis represents the beam-end moment M given by $M=Q\cdot L$, and the horizontal axis represents the beam rotation angle. The red line in the figure represents the full plastic moment M_p and calculated stiffness K_{cal} of the beam, which was calculated based on the material test results. With increasing-amplitude loading, all specimens exhibited stable hysteresis behaviors regardless of the presence of a vertical oblique angle. From the results of the hysteretic curves, a slight difference can be observed between the maximum strength in positive and negative loading directions, which may be attributed to experimental errors caused by slight deformations in the fixed boundary conditions of fixture jigs. Furthermore, all specimens were in an elastic state when the beam rotation angle was less than 0.01 rad, and the experimental stiffness showed good agreement with the calculated stiffness. During constant-amplitude loading, local buckling was observed at the beam-end flange of the VN0, VN15, and VN30 specimens in the second cycle of 0.03 rad positive loading side. Following repeated cyclic loading, the beam-end moment gradually decreased because of the growth of local buckling at the beam flange. However, only V15 exhibited local buckling at the upper flange of the beam among the V series specimens, whereas the other specimens did not experience local buckling prior to failure.

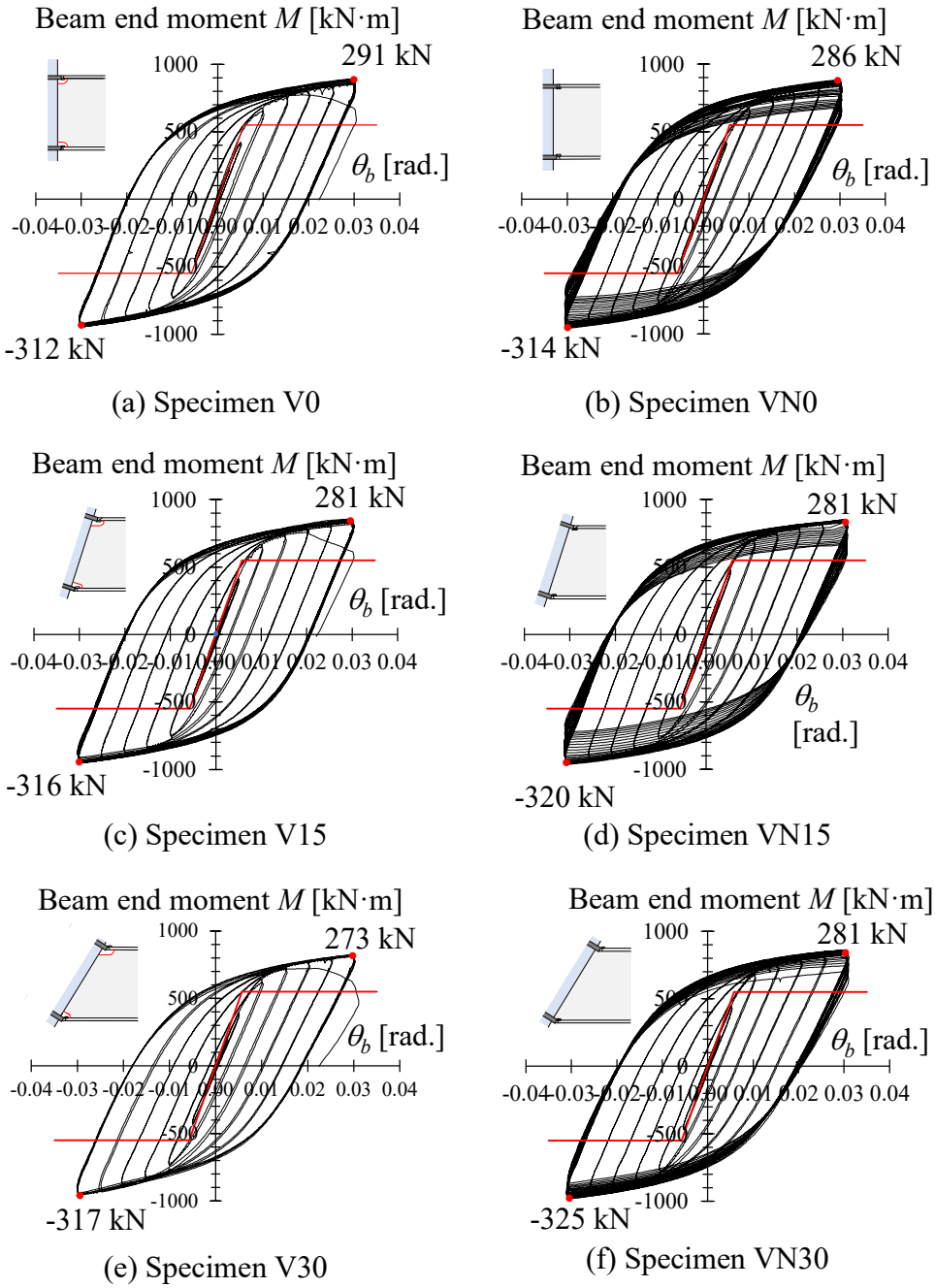

(a) Specimen V0 (b) Specimen VN0

(c) Specimen V15 (d) Specimen VN15

(e) Specimen V30 (f) Specimen VN30

Fig. 3.8 Hysteretic curves of the beam component.

The hysteretic curves of panel zones are shown in Fig. 3.9. The horizontal axis represents the shear deformation of the panel zone, which was calculated using triaxial strain gauges attached to the center of the panel. The black, yellow, and blue graphs represent specimens with vertical oblique angles of 0, 15, and 30°, respectively. The red line represents the shear stiffness of the panel zone, obtained from the triaxial strain gauges. For comparison, the results of the VN0 and V0 specimens are shown in gray along with the other results. The

hysteresis curves of the panels show that panel zones of all specimens exhibited elastic behavior. The deformations generated by the panels account for a small portion of the overall deformation. A comparison of the shear stiffnesses of the panels without a vertical oblique angle (k_{p0}) and those with an oblique angle showed that the former had a lower shear stiffness. From the mechanism analysis in Chapter 3.2, under the same loading shear force, the shear force on the panel zone of the specimen with a vertical oblique angle is smaller than

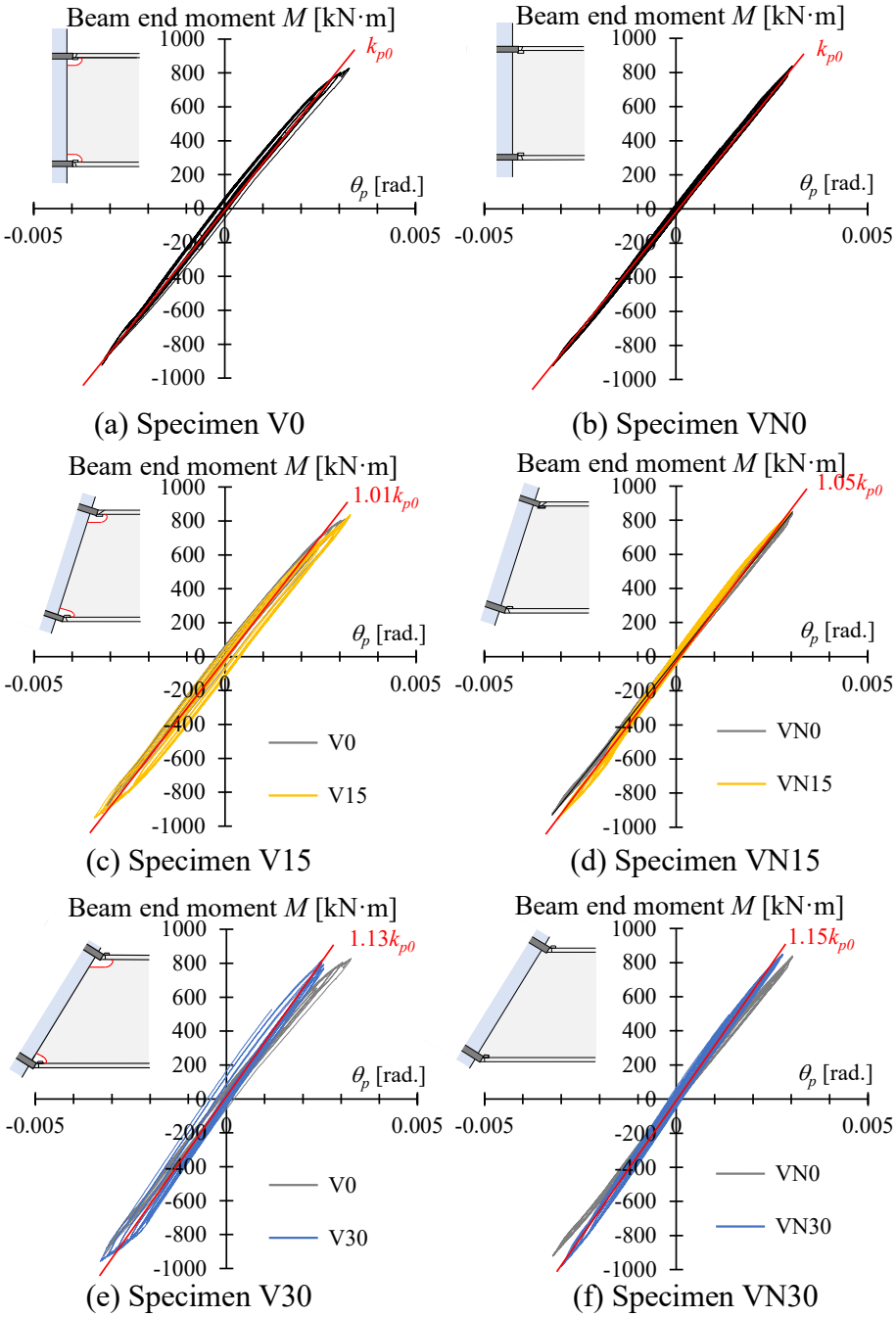

(a) Specimen V0 (b) Specimen VN0

(c) Specimen V15 (d) Specimen VN15

(e) Specimen V30 (f) Specimen VN30

Fig. 3.9 Hysteretic curves of panel zones.

that of the specimen without a vertical oblique angle, as given in Eqs. (1) and (2). Under the same loading conditions, the shear force of the panel zone decreased, which led to an increased stiffness.

3.4.2 Comparison of fracture modes and plastic deformation capacity

The stiffness, ultimate strength, and timing of the stop loading cycles are listed in Table 3.3. In the table, the experimental stiffness K_{exp} and calculated stiffness K_{cal} have similar results. The vertical oblique angle did not affect the connection stiffness, and the ultimate strengths on the positive loading side ${}_pM_u$ and negative loading side ${}_nM_u$ of each specimen were evaluated. The ultimate strength on the positive loading side was smaller than that on the negative loading side because of the fixation condition at the upper fixture of the test setup. Comparing ${}_pM_u$ and ${}_nM_u$ of the V and VN series revealed that, although there are minor differences between the ultimate strengths on the positive and negative loading sides, there was very little difference in the maximum strength of the beam-to-column connections, regardless of the size of the vertical oblique angle. The deformation capacity based on the timing of the fracture cycle can be expressed as follows: For the timing of the stop loading cycles of the VN and V specimens, the VN0 and VN15 specimens stopped loading when the strength decreased to 80% of the ultimate strength, while the VN30 and V specimens stopped loading when a fracture was clearly observed at the connection.

The maximum and minimum moment of each loading cycle were compared to investigate the deterioration in the beam strength of the specimens under constant-amplitude loading. The results are presented separately for the V and VN series in Fig. 3.10, where white, yellow, and blue represent specimens with vertical oblique angles of 0, 15, and 30°, respectively. The plastic deformation capacity of V series specimens was lower than that of the VN

Table 3.3 Summary of experimental results.

Specimen	Oblique angle Θ_V [degree]	Stiffness exp. K_{exp} [kN/mm]	Stiffness cal. K_{cal} [kN/mm]	K_{exp}/K_{cal}	Ult. Str. of positive ${}_pM_u$ [kN·m]	Ult. Str. of negative ${}_nM_u$ [kN·m]	Stop loading cycle Cyc [No.]
V0	0°	9.91	10.46	0.95	893.0	−946.0	0.03(11+)
V15	15°	10.07	10.64	0.95	856.7	−953.2	0.03(11+)
V30	30°	10.9	10.53	1.04	825.2	−958.1	0.03(5+)
VN0	0°	9.78	10.46	0.93	885.3	−957.8	0.03(28+)
VN15	15°	9.56	10.64	0.90	851.0	−963.3	0.03(19+)
VN30	30°	10.3	10.53	0.98	861.3	−982.7	0.03(20+)

*0.03(2-): The second cycle of 0.03 rad amplitude at the negative loading side.

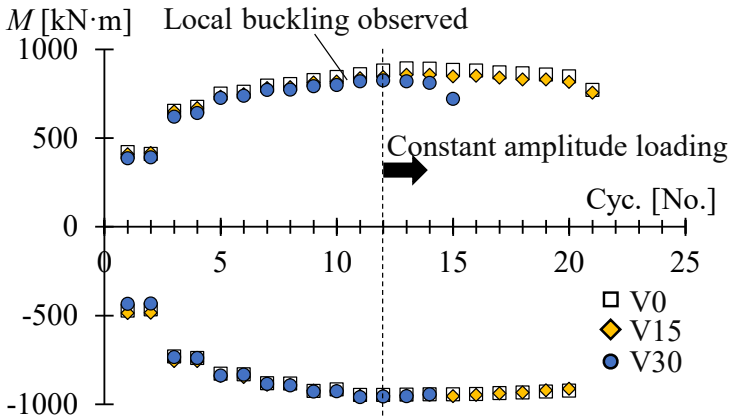

(a) V series

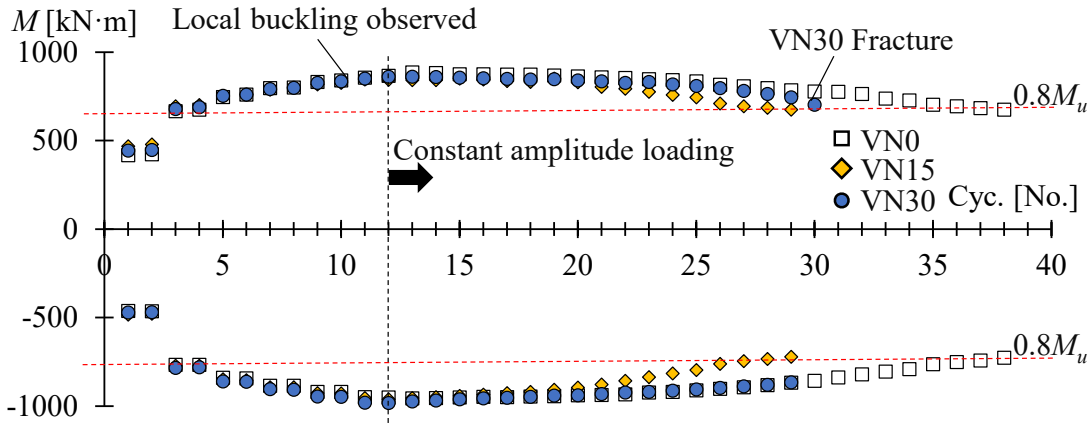

(b) VN series

Fig. 3.10 Comparison of strength deterioration.

series specimens. For both V and VN series, specimens with large vertical oblique angles demonstrated poor plastic deformation capacity. However, the vertical oblique angle only makes a small contribution to the deterioration of the connection strength under cyclic loading.

Photographs of the damage are shown in Photo. 3.3 In the V0 and V30 specimens, cracks originated at the bottom of the weld access holes of the upper flange of the beam at the first loading cycle of 0.02 rad amplitude. Cracks penetrated from the toe of the weld access holes progressed with cyclic loading, eventually leading to the complete fracture of the upper flange of the beam. In the V15 specimen, a similar crack appeared at the bottom of the weld access hole. However, in the first loading cycle of 0.03rad amplitude, local buckling occurred at the upper flange of the beam end, resulting in a slow process of the crack propagation. Although the V15 specimen eventually failed because of the fracture at the edge of weld between the upper flange of the beam and the diaphragm in the 11th cycle of constant

amplitude loading. In specimens without a weld access hole (VN0, VN15), cracks first appeared at the edge of the weld at a beam upper flange, and then, local buckling occurred near the beam end. The local buckling severely progressed faster than crack propagation, and the fracture did not occur at the beam ends. VN30 developed similar local buckling at the beam end; however, the growth of the crack at the edge of the weld at the beam upper flange led to a fracture of the connections. The results indicated that fractures occurred at the upper flange of the beam in specimens with vertical oblique angles, despite the bending moment in the lower flange of the beam being larger than that in the upper flange. This phenomenon is consistent with the analysis of the mechanism described in Chapter 3.2.

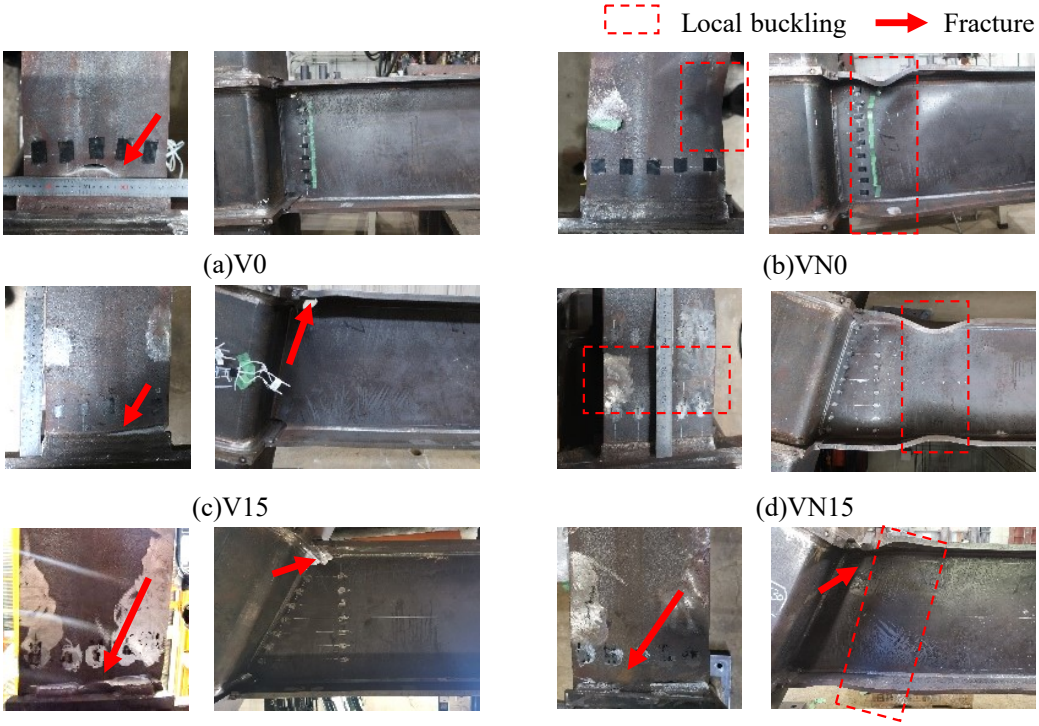

Photo. 3.2 Damage of specimens.

3.4.3 Comparison of skeleton curves

Skeleton curves extracted from the hysteretic curves were used to compare the plastic deformation capacity of the specimens. A basic skeleton curve is shown in Fig.3.11 (a). The skeleton curves of the VN and V series specimens are depicted in Fig.3.11 (b) and (c), respectively. In this figure, the vertical axis is the beam moment *M* and the horizontal axis is the beam rotation angle in the skeleton curve. The skeleton curves of the VN and V series specimens were almost the same in terms of the elastic and plastic behaviors. Therefore, the vertical oblique angle has little effect on the hysteretic behavior of the beam-end connections.

In Chapter 3.2, the mechanism analysis explained differences in the forces experienced by the upper and lower flanges of the beam. From the hysteretic behavior, it can be easily deduced that the upper flange develops plastic deformation earlier because the force in the upper flange of the beam is greater than that in the lower flange. Therefore, the point at which the beam stiffness decreased by 10% was defined as the first yielding moment M_y[11], as shown in Fig. 3.12.The intersection point between the extension lines of the initial and subsequent stiffness, which is a line connected between the point of the maximum beam rotation angle and half of that point, was determined as the full plastic moment M_p. The bending moment of the beam was provided by both flanges, and the moment generated by the beam web was neglected. Using Eq. (3.4), the yield moment of the upper flange of the beam can be calculated as

$$M_y = \frac{\sigma_y \cdot A_f \cdot L}{\frac{1}{D_b} + \tan \Theta_V} \tag{3.11}$$

where σ_y and A_f represent the yield stress of the beam flange and area of the upper flange of the beam, respectively. The results of the calculations based on Eq. (3.11) and the experimental yielding moments determined using the definition shown in Fig. 3.12 are summarized in Table 3.4 and Fig 3.13. The results show that the yield moment of the beam's upper flange decreases with an increase in the vertical oblique angle. The ratio of the experimental result ${}_{exp}M_y$ to the calculated result ${}_{cal}M_y$ was close to 1.0, which indicates that the proposed theory can effectively evaluate the reduction in the first yielding moment. Conversely, the vertical oblique angle does not affect the full plastic moment. The calculated result of the full plastic moment ${}_{cal}M_p$ and its experimental result ${}_{exp}M_p$ do not change significantly in accordance with the vertical oblique angle.

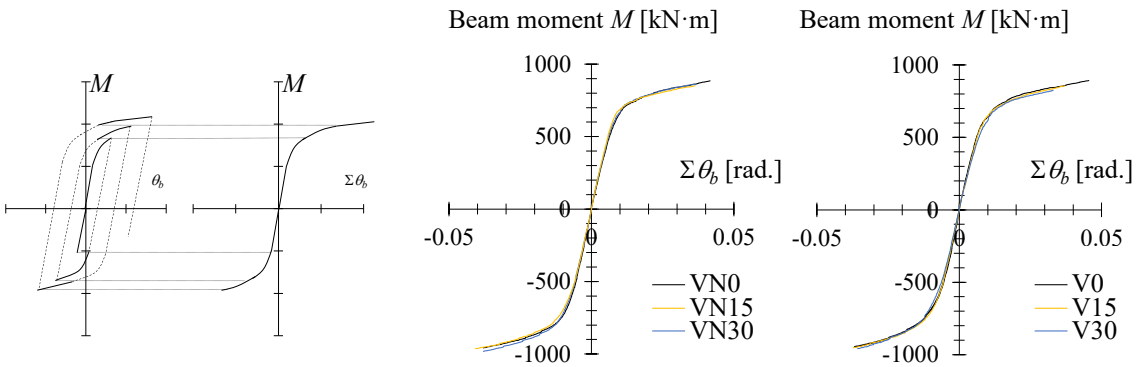

(a) Definition of skeleton curve (b) Skeleton curve of VN series (c) Skeleton curve of V series

Fig. 3.11 Comparison of skeleton curves.

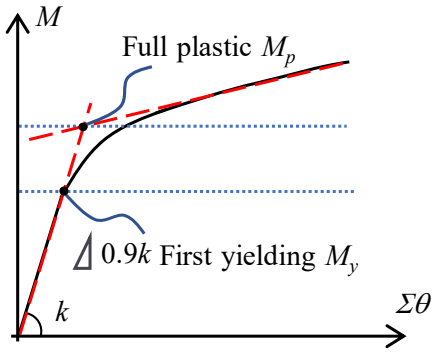

Fig. 3.12 Definition of the yielding moment.

Table 3.4 Summary of yielding moments.

Specimen	${}_{cal}M_p$ [kN·m]	${}_{exp}M_p$ [kN·m]	${}_{cal}M_y$ [kN·m]	${}_{exp}M_y$ [kN·m]	${}_{cal}M_y/{}_{exp}M_y$	${}_{cal}M_p/{}_{exp}M_p$
V0	676	737	549	0.95	1.01	0.92
V15		720	537	0.95	1.01	0.94
V30		718	524	1.04	1.03	0.94
VN0		718	549	0.93	0.98	0.94
VN15		730	537	0.90	0.99	0.93
VN30		725	524	0.98	0.99	0.93

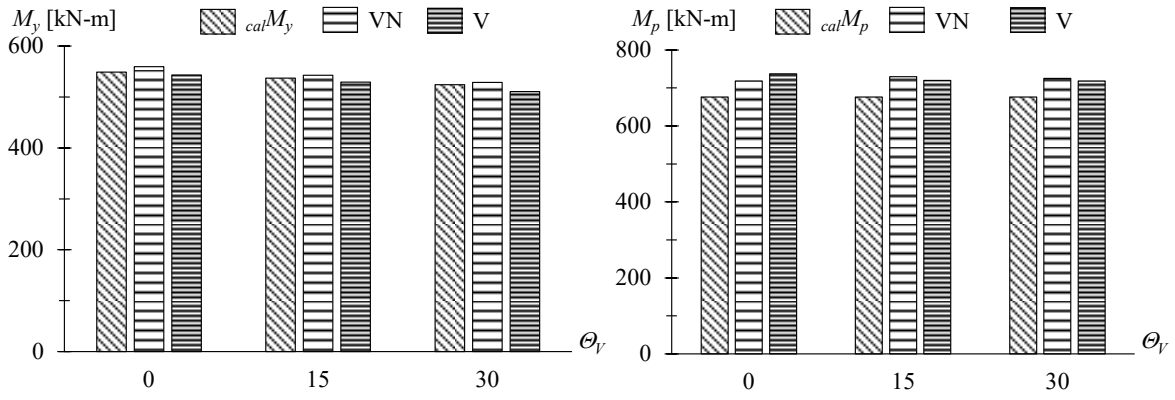

Fig. 3.13 Comparison of the yielding and full plastic moment.

3.4.4 Damage of beam flange

According to the experimental results, V0, V15, V30 and VN30 specimens failed at the end of the upper flange of the beam. To confirm the damage to the beam end, the deformations of the beam flange and web were evaluated in this and next chapter. Owing to cyclic loading, strain was generated per cycle, which was analyzed based on the strain range [12].

First, the damage to the beam flanges was evaluated. Fig. 3.14 presents a comparison

of the average strain ranges at points A, B, and B' of each specimen. In this figure, the vertical axis represents the average of the strain range $\Delta\varepsilon$ and horizontal axis represents the beam rotation angle θ_b. The average of the strain range $\Delta\varepsilon$ per cycle was determined as the difference of mean of all strain data measured at the peak deformation point in the positive and negative loading sides by the five strain gauges affixed to the beam flange section (Fig. 3.6). The strain ranges at point A on the upper beam end and points B and B' on the lower beam end are denoted as ${}_A\varepsilon_{\Theta V}$ and ${}_B\varepsilon_{\Theta V}$ and ${}_{B'}\varepsilon_{\Theta V}$, respectively. In addition, the lines of different shapes represent specimens with different vertical oblique angles, whereas the different col-

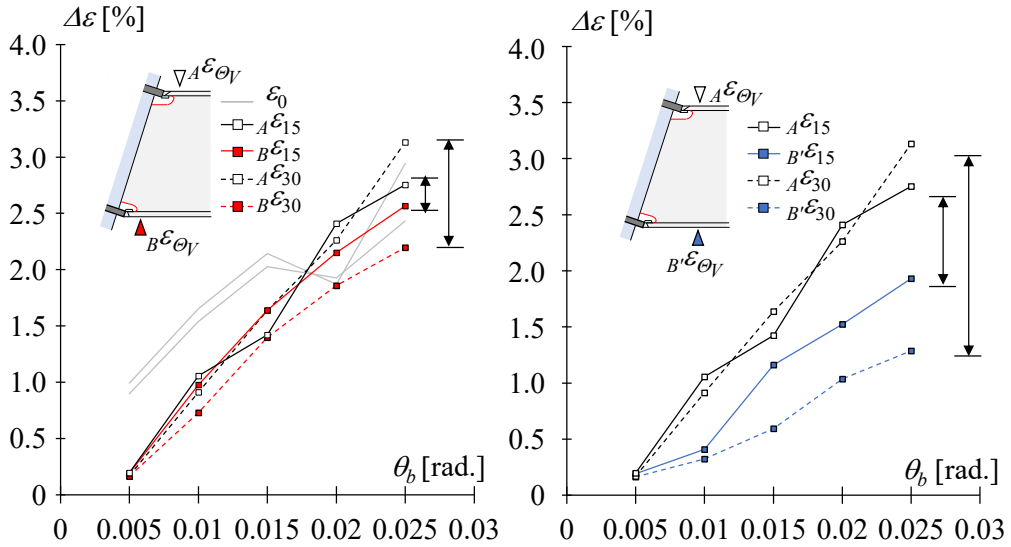

(a) *AB* section of V specimens (b) AB' section of V specimens

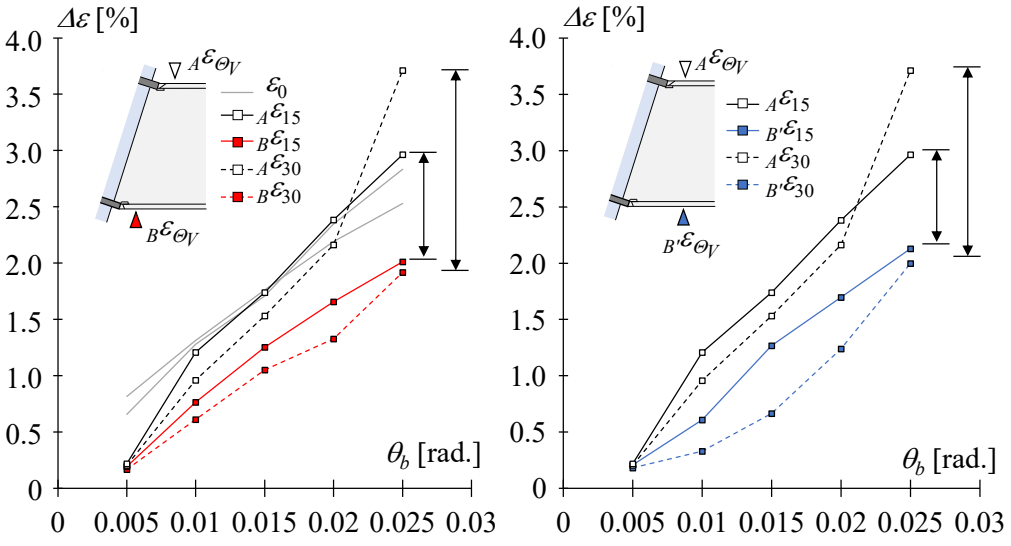

(c) AB section of VN specimens (d) AB' section of NS specimens

Fig. 3.14 Effect of the vertical oblique angle on the average strain range at beam flanges.

ors of the square markers denote the strain ranges at different points on the upper and lower beam ends. Comparing the results of the solid (Θ_V =15°) and dashed (Θ_V =30°) lines of V and VN series of specimens indicates that the difference between points A ($_A\varepsilon_{\Theta V}$) and B ($_A\varepsilon_{\Theta V}$) becomes more pronounced with an increase in the vertical oblique angle, which is indicated by the vertical black arrow, especially evident in the results of the VN specimens (Fig. 3.14(c)). Furthermore, the results of the strain range at the three sections ($_A\varepsilon_{\Theta V}$, $_B\varepsilon_{\Theta V}$, $_{B'}\varepsilon_{\Theta V}$) indicate that the deformation at the upper flange ($_A\varepsilon_{\Theta V}$) of the beam of all specimens (black lines) are greater than those in each section of the lower flange ($_B\varepsilon_{\Theta V}$, $_{B'}\varepsilon_{\Theta V}$) (colored line). This result is consistent with the fracture photographs (Photo. 3.2). In addition, comparing the strain ranges at points B and B' on the lower flange of the beam show that the strain range at point B is slightly larger than that at point B' in the VN series of specimens; however, the difference is not significant (see Fig. 3.14(c), (d)). However, for the V series specimens, this difference was very apparent and increased with the vertical oblique angle (Fig. 3.14(a), (b)), which means that the weld access hole causes the strain concentration of the lower flange at the beam end.

3.4.5 Damage of beam web

Similar to the beam flanges, the damage to the beam web was analyzed using the strain range. However, this analysis focused on the distribution of the deformation in sections AB and AB' because of the change in the shape of the beam web. Owing to local buckling, only the behavior obtained in the increasing-amplitude loading section is discussed. Fig. 3.15 and Fig. 3.16 shows the strain distribution with the 15 and 30° specimens in the first cycle of positive loading from 0.005–0.025 rad amplitudes in sections AB and AB'. Strain distributions at 15 and 30° were similar despite the size of the vertical oblique angle. The vertical axis represents the depth of the beam and the horizontal axis represents the strain range of the beam web. The red and blue squares indicate the strain distributions in sections AB and AB', respectively. Compared to the results of the specimens without a vertical oblique angle, a clear variation in the strain distribution can be observed in the triangular part of the beam end, especially at section AB (Fig. 3.15(c), (f)), where the strain distribution shows asymmetric results. Almost all deformation was concentrated in the lower half of the beam web, with minimal deformation in the upper half. In section AB', the deformation remained concentrated in the lower part (Fig. 3.15(b), (e)) in addition to a small increase in the neutral axis of the

beam. This result confirms the conclusion in Section 3.2 that the resultant force N_w of the beam web is in the lower part of section AB'. In the S and NS series of specimens, the deformation was concentrated in section AB, especially near the weld access holes (Fig. 3.15(c), (f)). Overall, the vertical oblique angle significantly affected the strain distribution at the

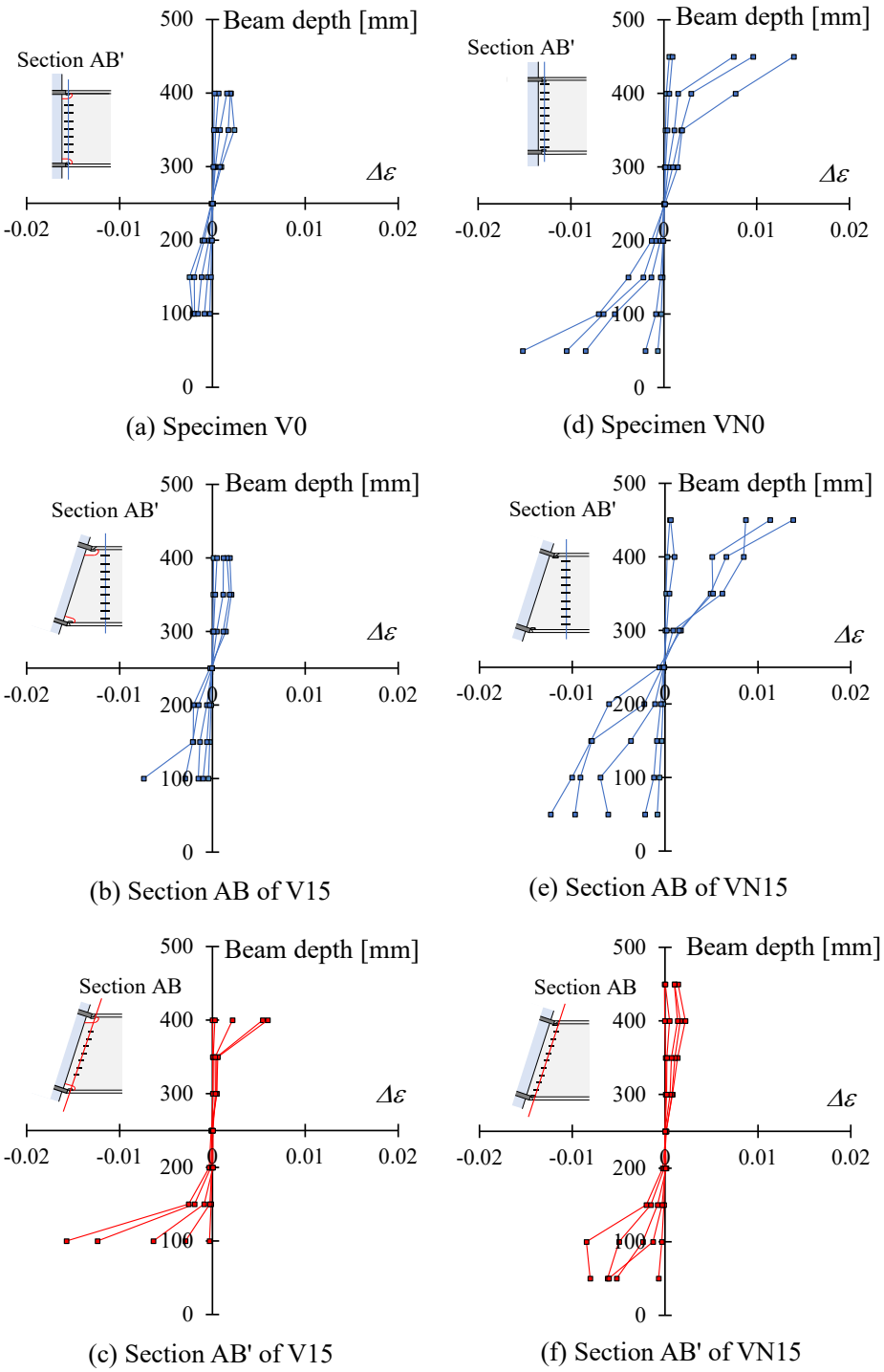

(a) Specimen V0 (d) Specimen VN0

(b) Section AB of V15 (e) Section AB of VN15

(c) Section AB' of V15 (f) Section AB' of VN15

Fig. 3.15 Strain range at beam web with oblique angle of 15.

beam end. In the beam web, the vertical oblique angle caused the strain distribution at the beam end to be asymmetric rather than triangular as in the NS0 and S0 specimens.

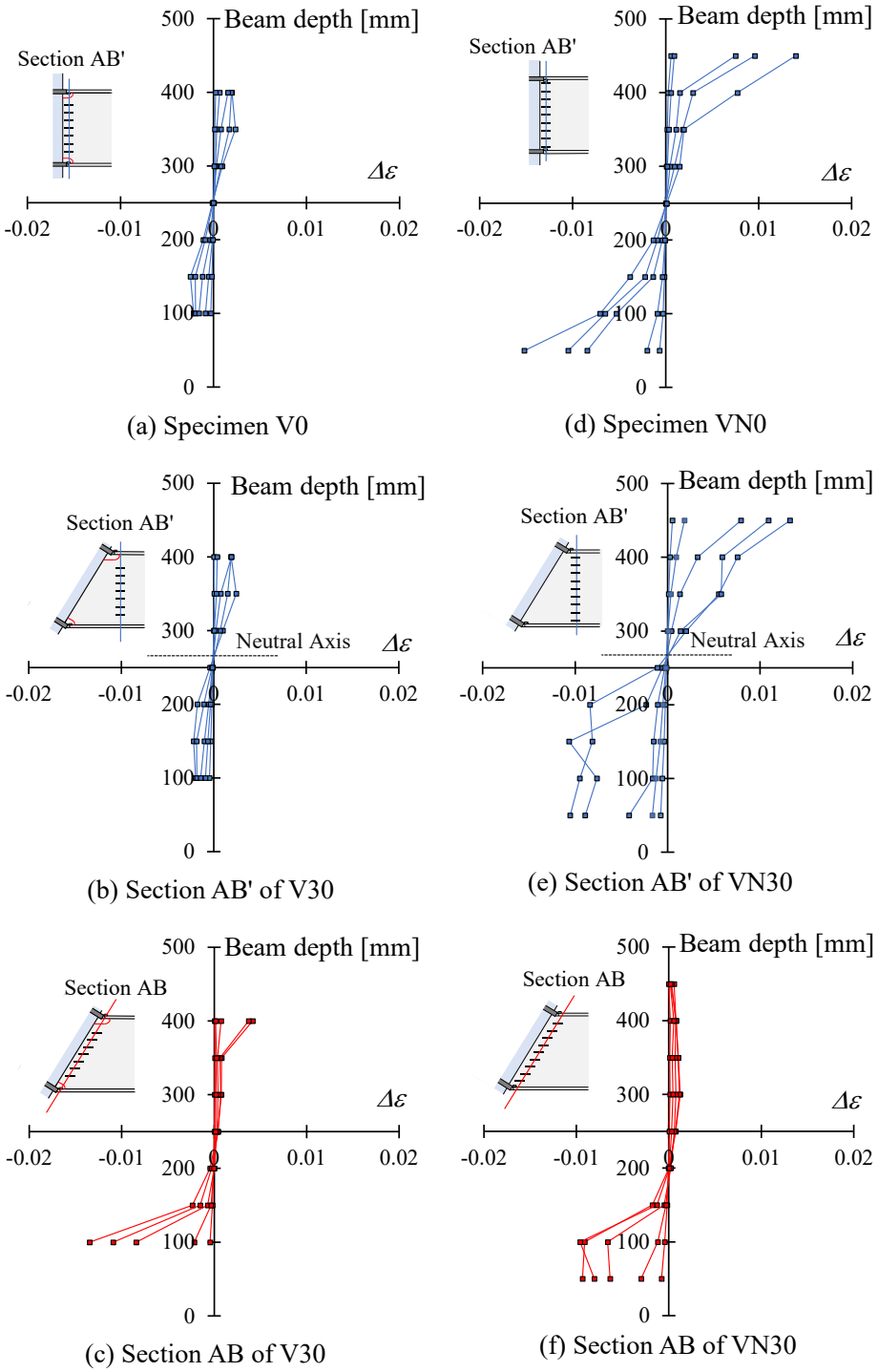

(a) Specimen V0

(d) Specimen VN0

(b) Section AB' of V30

(e) Section AB' of VN30

(c) Section AB of V30

(f) Section AB of VN30

Fig. 3.15 Strain range at beam web with oblique angle of 30.

3.5 Conclusions

This study investigated the effects of vertical oblique angles on the seismic behavior of SHS steel column-to-H beam-end connections under cyclic loading and proposed a mechanism analysis for beam-to-column connections. To clarify the critical section and results of the mechanism analysis, a full-scale experimental study of beam-to-column connections was conducted. The experimental results were analyzed from three aspects: hysteretic curves, failure modes, and strain and stress distribution, confirming the prediction from the mechanism analysis.

(1) In the mechanism analysis, a force model at the beam end was analyzed to calculate the internal forces on the upper and lower flanges of the beam. The critical failure section from the end of the upper flange to end of the lower flange was identified based on this analysis. A method for confirming the beam span was also established.

(2) In the full-scale experiment, all specimens exhibited stable hysteretic behavior. The analysis of the stiffness, ultimate strength, and skeleton curves indicated that vertical oblique angles had little effect on the cyclic hysteresis behavior (elastic stiffness and max strength) of beam-to-column connections.

(3) Beam-end connections with vertical oblique angles begin to fail from the upper flange. By analyzing the fracture mode and number of cycles to failure, it is clear that when the vertical oblique angle increases, the plastic deformation capacity of the connections noticeably decreases. Additionally, connections with weld access holes exhibit lower plastic deformation capacity than those without weld access holes.

(4) In beams with vertical oblique angles, the asymmetrical shape at the beam end resulted in an asymmetric strain distribution between the upper and lower parts. The deformation at the beam end was primarily concentrated in the upper flange, followed by that at the end of the lower flange. In the beam web, a greater amount of strain was concentrated in the lower half, causing the neutral axis at the beam end to incline toward the upper flange. This result is consistent with the findings of the mechanism analysis..

(5) The vertical oblique angles of beam-to-column connections result in an internal force difference between the upper and lower flanges, with the upper flange experi-

encing greater internal force, which increases with the vertical oblique angle increase. An evaluation method based on the upper flange yield for determining the beam's yield point is provided and verified. In engineering practice, it is advisable to avoid large vertical oblique angles and welded access holes to maintain the plastic deformation capacity of the beam ends.

References

[1] L. Liang, et al. Seismic behavior of irregular shaped beam-column connections, Eng. Struct. 297 (2023) 116942

[2] B. Mou, et al., Experimental investigation on shear behavior of steel beam-to-CFST column connections with irregular panel zone. Eng. Struct. 168 (2018) 487-504.

[3] B. Mou, et al., Numerical investigation and design method of bolted beam-column joint panel with eccentricity in beam depths, J. Constr. Steel Res. 180 (2021) 106568.

[4] B. Mou et al., Shear behavior of panel zone with an eccentricity between beam depths: Parameter study and design methodology, Journal of Building Engineering, 40 (2022) 103690.

[5] Japan Steel Constructors Association (JSC). Standard Detail of Steel Structural Frame. Japan Steel Structure Journal Co., Tokyo, 2016 (in Japanese).

[6] Japanese Society of Steel Construction (JSSC). Design Guide of Steel Frame Structures Connections Details. Building Research Institute, Tokyo, 2017.(in Japanese)

[7]] S. Shiraga, M. Tabuchi, T. Tanaka, A study of beam-to-column connections by fillet weld – Part 4. Strength of oblique crossing weld. Summaries of Technical Papers of Annual Meeting Architectural Institute, Japan, 1997, pp. 289–290 (in Japanese).

[8] Architectural Institute of Japan, AIJ Recommendation for Design of Connections in Steel Structures, Maruzen, Tokyo, 2021. (In Japanese)

[9] Y.J. Kim, S.H. Oh, Effect of the moment transfer efficiency of a beam web on deformation capacity at box column-to-H beam connections, J. Constr. Steel Res. 63 (2007) 24–36.

[10] Japanese Standards Association (JSA), Ferrous Materials & Metallurgy I-2019: Metallic materials-tensile testing (JIS Z 2241), JSA, Tokyo, 2018.

[11] R. Park, Ductility evaluation from laboratory and analytical testing. Proceedings of the 9th world conference on earthquake engineering. Tokyo-Kyoto, Japan, 1988.

[12] Y. Dong et al. Cyclic Behaviors of SHS Columns in Low Cycle Fatigue Tests, Journal of Earthquake Engineering (2022) 1–28.

CHAPTER 4

Finite element analysis of beam-end connection with horizontal or vertical oblique angle

4.1 Introduction

Steel structures, widely used in Japan, offer advantages such as high strength, excellent seismic performance and ease of construction. However, the inherent characteristics of steel, including geometric nonlinearity (large deformation effects) and material nonlinearity (such as yield and hardening behaviors), introduce challenges to accurate numerical analysis. Finite element (FE) method, incorporating nonlinear solution techniques alongside constitutive and contact models, enables the precise simulation of these complex behaviors. This kind of analysis results provides more reliable prediction of seismic response, support for design involving high-strength steel, large-span structures, and intricate connections. ABAQUS is a widely recognized tool for FE analysis, offering capabilities not only in static analysis but also in modal, buckling[1-2], and fatigue analyses[3]. Through FE analysis, detailed modeling can catch stress distribution[4], strain states[5], and internal force transfer mechanisms among components, especially in high stress concentration areas such as beam-to-column connections[6] and welds[7]. FE analyses not only help reducing the costs of experiment but also facilitate design optimization. Recent advancements in computational power and algorithmic developments have significantly accelerated the use of FE analysis in steel structure simulation. New constitutive models[8-9] and new algorithms[10] have been led to more accurate results. However, despite the advantages of FE analysis, a number of practical challenges remain, including the accuracy of complex structures, saving computing resources, and validation of results with experimental data.

In the experimental studies presented in Chapters 2 and 3, it was observed that oblique angles introduce notable differences in stress and strain distribution at beam-ends. These change in strain and stress reduce the plastic deformation capacity of beam-to-column connections. However, there are gaps in the experimental data. Only certain angle effects have been captured. In order to fill these gaps and to more comprehensively evaluate the effects of oblique angle on stress and strain distributions, this chapter uses ABAQUS software to simulate beam-end connections with oblique angles. After verifying that the analysis accurately replicates experimental results, parameter such as oblique angle, beam section, beam span, and loading condition will be examined for their effect on the performance of the connection.

4.2 FEA results of beam-end with vertical oblique angle

In the previous analysis of the strain distribution in Sections 3.4.4 and 3.4.5, the internal force difference between the upper and lower flanges and the asymmetric strain results of beam web were shown. Such findings imply a significant difference in the stress distribution in the beam-end connections with a vertical oblique angle. In this chapter, the FE analysis to determine the stress distribution at the beam-end is presented. Furthermore, the mechanism analysis model mentioned in Section 3.2 for predicting the strength of the upper and lower beam flanges will be compared to the analysis result. A parameter analysis on beam depth and span will be given to show the effect in the connection with vertical oblique angle.

4.2.1 Model construction

The FE models of the specimens were constructed using software Abaqus/CAE 2020. Since effectiveness of reduced integration method was presented [11-12], solid elements using a mixture of 8-node linear reduced integration was utilized for establishment of all models for the FE analysis. The FE model (S30) is shown in Fig. 4.1. Because the column and diaphragm remained in an elastic state during loading, only the beam part was modeled instead of the entire column to simplify the analysis. The analytical models were segregated into series with and without weld access holes (S and NS series, respectively) to ensure consistency with the experimental conditions. Since both the element tests and full-scale experiments exhibited fractures away from the weld. In all the models, the backing plates of the weld at the beam-

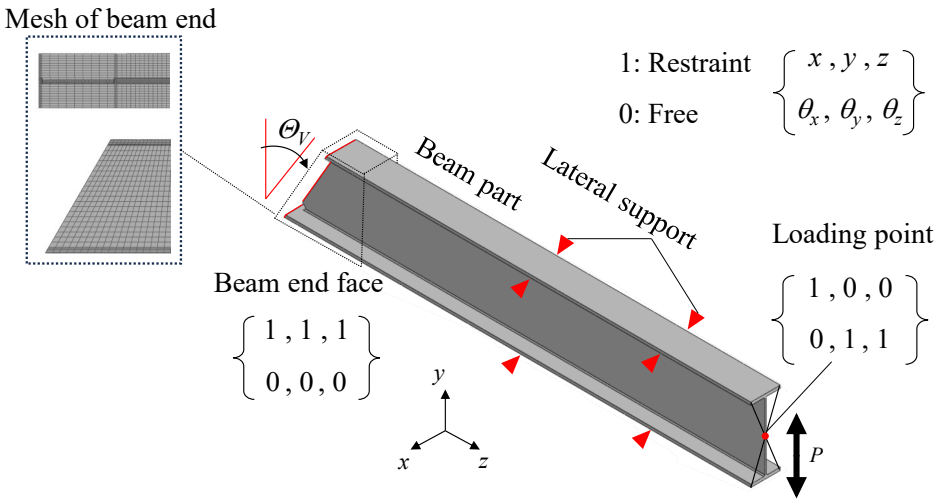

Fig.4.1 FE models of beam-end connection with vertical oblique angle (V30).

end were not constructed. A structural optimization method was adopted to represent the components as regular-shaped meshes. Total number of mesh used for each model is approximately 26000, while that of areas near weld access holes were finely meshing to enhance the accuracy of the analysis. For the boundary condition, the face of the beam-end was completely fixed in *x*, *y* ,*z* direction whereas loading was applied at a point about 3000 mm away from the beam-end and rotation of the point in *y* and *z* directions was fixed to match the experimental conditions (Fig. 4.1). A full Newton and geometric nonlinear were chosen for the iteration's algorithm of FE models. The loading protocol used in the analysis adopted the approach of increasing amplitude employed in the experiments. Because of the nonlinear nature of the materials, the analysis was based on the Von Mises criterion, and kinematic and isotropic hardening properties were employed for the materials setting. The properties of materials used in the analysis were based on the results of the nominal stress and strain relationship obtained from materials coupon test in Chapter 3.3.1, which were converted into true stress and true strain data.

4.2.2 Comparison of experimental results

Fig. 4.2 shows a comparison of the hysteretic curves between the FE analysis and experimental results. Although small discrepancies appeared in the Bauschinger part, the FE analytical results aligned well with the experimental results and exhibited stable hysteretic behavior. The maximum moment and elastic stiffness values obtained from the analysis are listed in Table 4.1. The vertical oblique angle had no influence on the maximum moment or

stiffness. For the maximum moments at the positive ($_pM_u$) and negative ($_nM_u$) loading sides, the ratio of the experimental to analytical results varied in the range of 0.92 to 1.10. There-

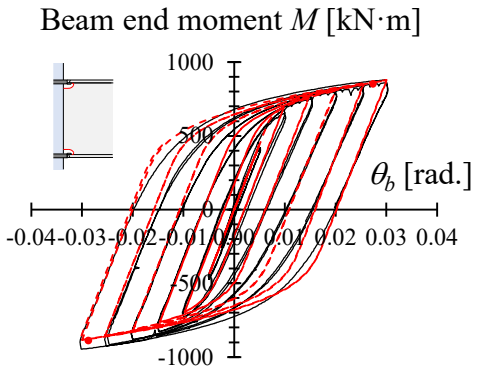

(a) Specimen V0

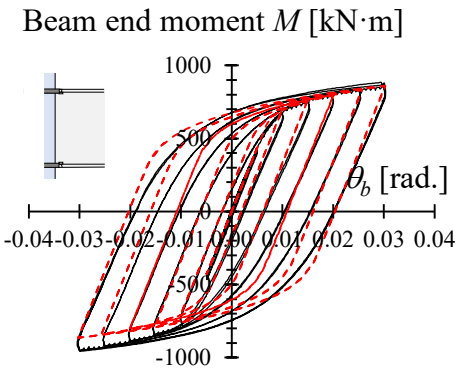

(b) Specimen VN0

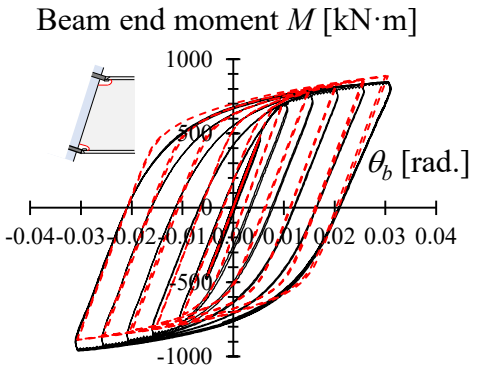

(c) Specimen V15

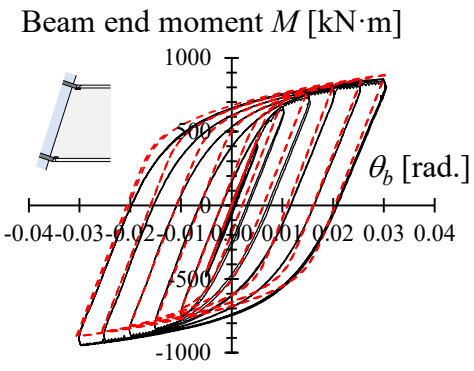

(d) Specimen VN15

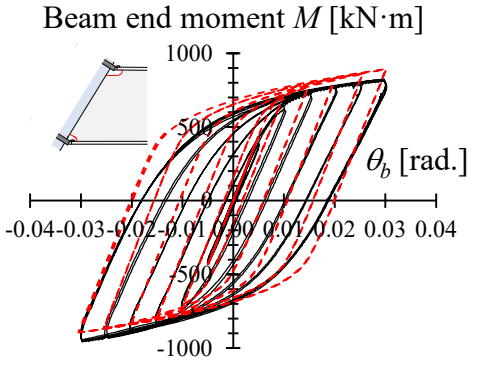

(e) Specimen V30

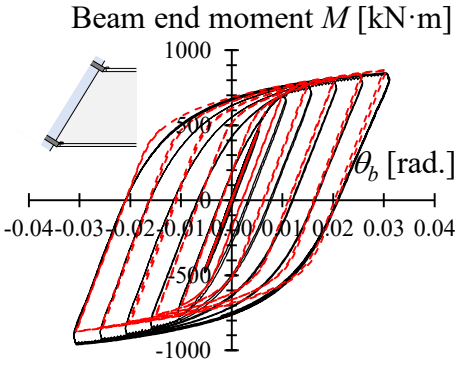

(f) Specimen VN30

Fig.4.2 Comparison of hysteretic curves obtained from FE analytical results.

Table 4.1 Summary of FE analytical results

Specimen	Stiffness K_{FEA} [kN/mm]	K_{exp} / K_{FEA}	Ult. Str. of positive ${}_pM_{u\text{-}F}$ [kN·m]	Ult. Str. of negative ${}_nM_{u\text{-}F}$ [kN·m]	${}_pM_u$ / ${}_pM_{u\text{-}F}$	${}_nM_u$ / ${}_nM_{u\text{-}F}$
V0	9.50	0.95	881.29	−886.62	1.01	1.07
V15	9.72	0.95	891.82	−895.44	0.96	1.06
V30	9.67	1.04	901.26	−902.72	0.92	1.06
VN0	9.50	0.93	879.16	−884.52	1.01	1.08
VN15	9.50	0.90	885.71	−889.15	0.96	1.08
VN30	9.50	0.98	893.06	−893.99	0.96	1.10

fore, the FE analytical results clearly reflect the experimental outcomes.

4.2.3 Analysis of stress distribution and internal force at beam-end

The stress distribution of S33, obtained from the FE analysis, was compared with the strain distribution from the experiment. Fig. 4.3 shows the stress distribution at the peak of positive loading in the first cycle of 0.025 rad. The centroid line of the beam and maximum stress are also marked in the figure. The stress distributions of the specimens with vertical oblique angles appear to be asymmetric, unlike those of the VN0 and V0 specimens. For the specimens with vertical oblique angle, the area of compression in the lower half of the beam web is significantly larger than that in the upper half. It can also be observed that the tensile stress in the upper flange of the beam is greater than the compressive stress in the lower flange. In the stress distribution at the beam-end, the neutral axis gradually rises from the triangular part of the beam-end. The greater the vertical oblique angle, the more the neutral axis rises. This result agrees with the experimental results, indicating that the analytical stress dis-

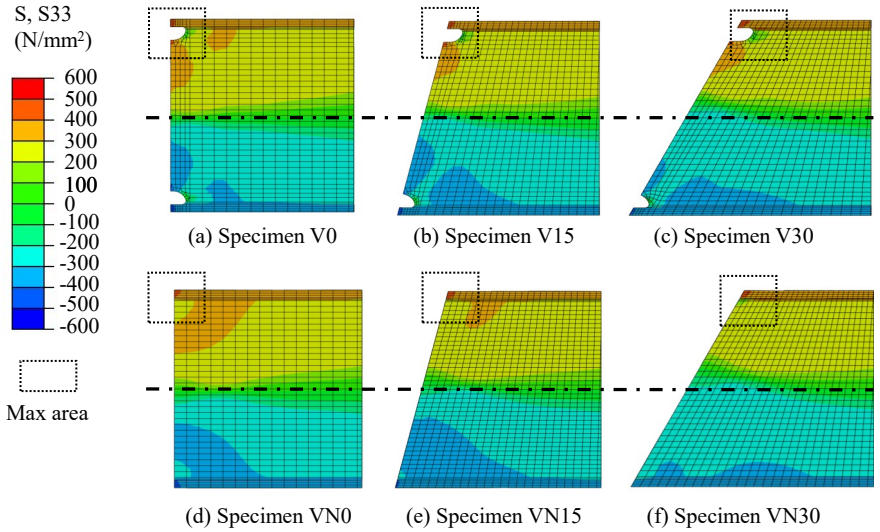

Fig.4.3 Stress distribution from FE analysis at 0.025 rad (z direction).

tribution generally reflects the state of the beam in the experiments.

These results demonstrated that the FE analysis results can effectively reflect the stress state at the beam-end. Therefore, to analyze the internal forces at the critical section of the upper and lower flanges of the beam, the stress σ_{33} of the flanges in the z direction was extracted. Then, the internal force $F_{f\theta}$ at the upper and lower flanges for different vertical oblique angles can be given as

$$F_{f\theta} = \sum_{1}^{i} {}_{i}A_{f} \cdot {}_{i}\sigma_{33} \tag{4.1}$$

where σ_{33} is the stress in the z direction for each element and ${}_{i}A_{f}$ is the projected area of each element in the z direction. Fig. 4.4 shows the internal forces of the beam flanges, obtained from the FE analysis, versus the beam rotation. In the figure, the square markers represent the internal forces calculated at different positions on the upper and lower flanges of the

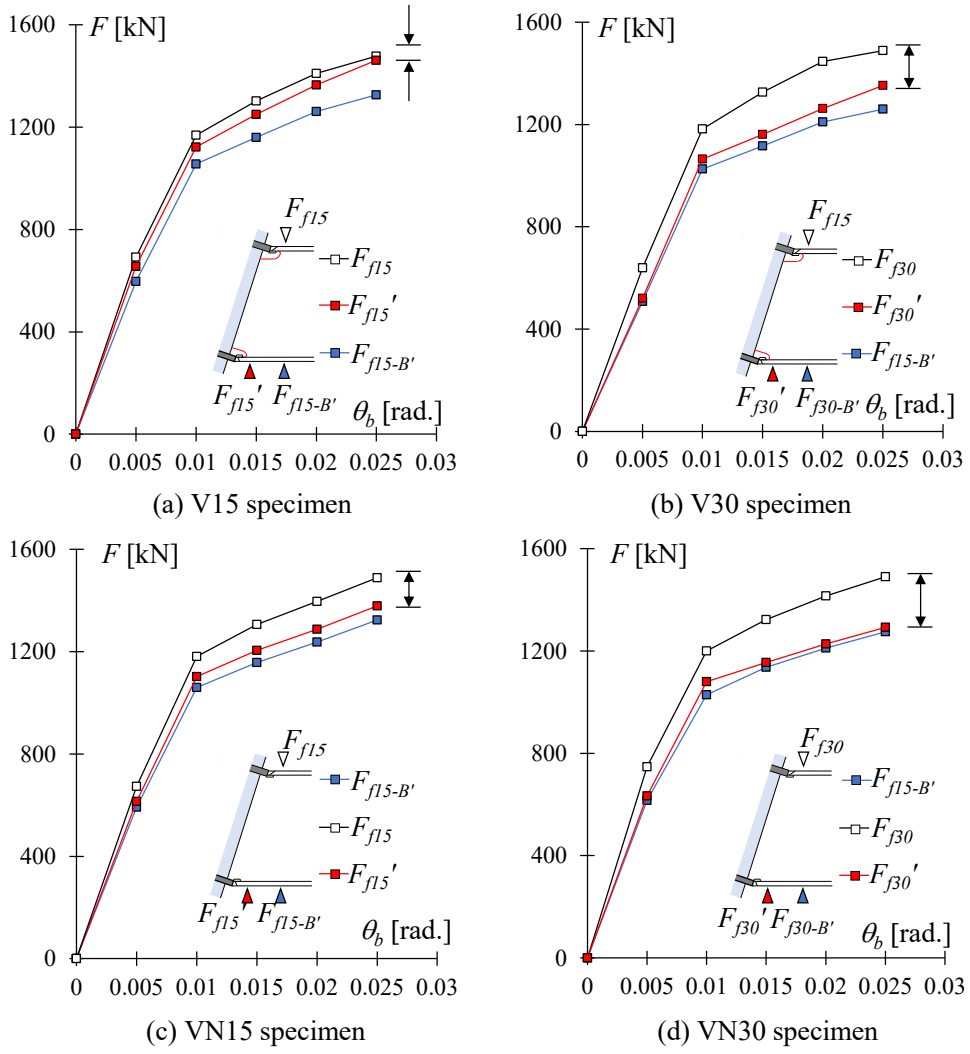

(a) V15 specimen (b) V30 specimen

(c) VN15 specimen (d) VN30 specimen

Fig.4.4 Stress distribution from FE analysis at 0.025 rad (z direction).

beam. Owing to the occurrence of local buckling at the 0.03 rad cycle, the results are shown only until 0.025 rad. A comparison of the results also showed that the internal forces at the end of the upper flange were greater than those at the lower flange of the beam-end and those at point B'. At the same time, the difference in internal forces between the upper and lower flange of the V and VN specimens also changes considerably in plastic state.

4.2.4 Effect of weld access hole

Additionally, to better understand the variation in the internal forces in the upper and lower flanges at the failure section after plastic deformation, the changes in the internal force differences between the upper and lower flanges at each beam rotation angle are presented in Fig. 4.5. The dashed lines represent the calculation results of the difference between Eqs. (3.4) and (3.5) from Section 3.2 defined as $\Delta F_{f\text{-}cal}$, and black squares represent the difference in the internal force between the upper flange F_f and lower flange F_f', obtained from the FE analysis. It can be observed that the calculated and FE analytical results align very well in the elastic state, indicating that the mechanism analysis can effectively predict the capacity of the upper and lower flanges of the beam. After the initiation of plastic deformation (0.01–0.025 rad.), there was a significant variation in the difference in the internal force between the upper flange F_f and lower flange F_f' for the V and VN specimens. In the V series, the internal force difference between the upper and lower flanges at the beam-end decreased significantly, indicating that the stress at the lower flange of the beam-end rapidly increased with the progress of plasticity. However, this phenomenon was not observed in the VN series. This

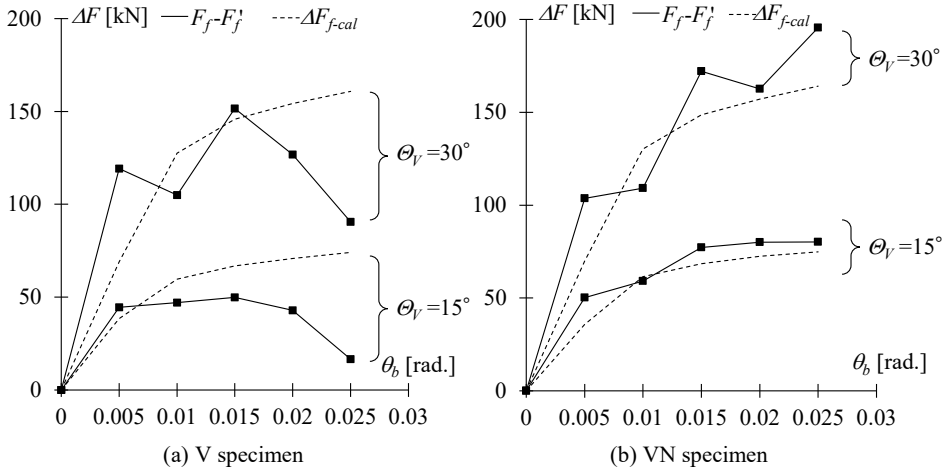

Fig.4.5 Difference between internal forces of beam flanges obtained from FE analysis and theoretical analysis.

suggests that the presence of weld access holes increases the internal force on the lower flange of the beam-end in elastoplastic behavior. These results are consistent with the experimental results of the strain distribution at the beam-end described in Section 3.4.4.

4.2.5 Parameter analysis

The previous section shows the validity of the FE analysis results in internal forces as well as stress distributions. Therefore, in this chapter, based on the validity of the FE analysis, a numerical analysis will be conducted to discuss the effect of vertical oblique angles on the structural behavior of the beam-end connections in various conditions.

4.2.5.1 Effect of different loading method

In practical case of beam-end connections with vertical oblique angle, cases involving beams with vertical oblique angles are more common than those involving column with oblique angles. For instance, beams in sloped roofs often exhibit vertical oblique angles, when beams are connected to column with vertical oblique angle, the shear force they experience is typically perpendicular to the beam, as shown in Fig. 4.6(b). Unlike the case of column with an oblique angle (Fig.4.6(a)), this configuration also introduces a component force along the beam direction. In beam-end connections without oblique angles, previous studies [13] have clarified the effects of axial forces acting along the beam direction on maximum strength, local buckling, failure modes, and strain distribution. Therefore, to analyze the influence of axial force on beam-end connections with vertical oblique angle, this chapter simulates two loading modes to clarify the impact of axial force on long-term loads.

Table 4.2 presents the numerical analysis specimens. The parameters for the FE analy-

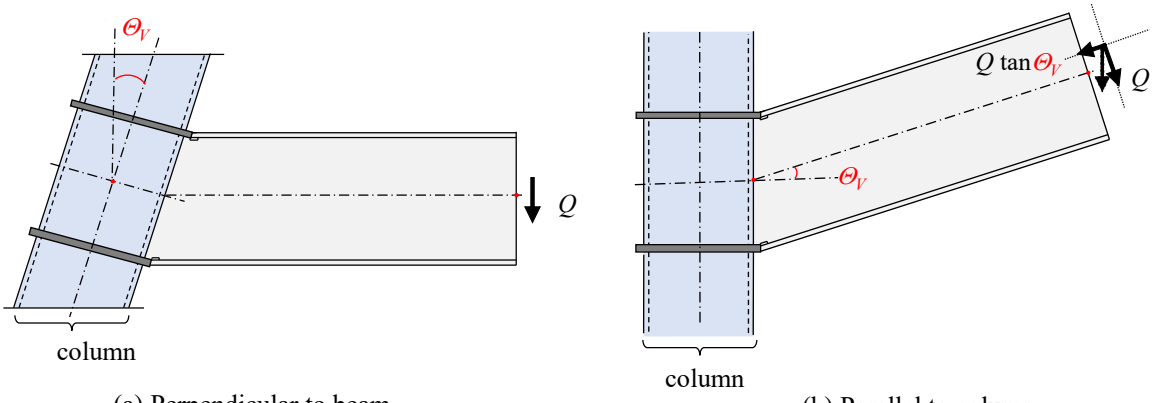

(a) Perpendicular to beam (b) Parallel to column

Fig.4.6 Different loading directions in practice.

Table 4.2 Analysis list of loading method

Spec.	Θ_V	Section	Span L	Loading method	Loading direction
VN30	30	BH 500x200x9x19	3000	Cycle loading	Perpendicular to beam
VN30-M	30			Monotonic loading	
VN30-O	30				Parallel to column

sis are the loading directions: one paralleled to the column and the other perpendicular to the beam. To understand the effects of long-term loads, monotonic loading was applied in the analysis. For the loading direction paralleled to the column, the load was applied by decomposing the force into two components: one parallel to the beam and the other is perpendicular to the beam, and both components were applied at same time. The oblique angle at the beam-end was set to 30 degrees to emphasize its impact. The beam section and span were consistent with the experimental conditions. Additionally, the material properties, model, and analysis conditions were consistent with those used in the previous section.

The numerical analysis results are shown in Fig. 4.7. The gray line represents the results of VN30 specimen under cyclic loading, while the red solid line represents the analytical results of VN30-M specimen under the loading perpendicular to the beam. The red dashed line indicates the results of VN30-O specimen under the loading parallel to the column. The results match the yield strength and maximum strength observed under cyclic loading, confirming the validity of monotonic loading for beam-end connections with vertical oblique angles. A comparison between VN30-M and VN30-O reveals that under different loading directions, the presence of axial force causes a slight reduction in the maximum

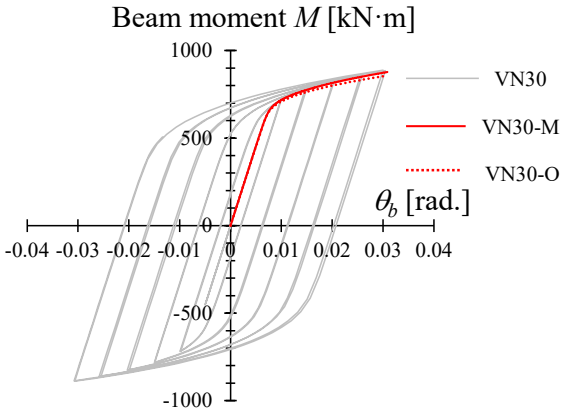

Fig.4.7 Loading behavior of numerical analysis.

strength.

To further analyze the impact of axial force, the internal forces at the upper and lower flanges at the beam-end were extracted using the method described in Eq.(4.1). The comparison results are shown in Fig. 4.8(a), where the vertical axis represents internal force of flange and the horizontal axis represents beam rotation angle θ_b. Solid lines represent the results for VN30-M, while dashed lines indicate VN30-O results. The black line represents the internal force in the upper flange, and the red line represents the internal force in the lower flange. The results clearly show that the internal force difference between the upper and lower flanges decreases significantly in VN30-O compared to VN30-M. The reduction in the internal force difference is attributed to the axial force generated during loading, as illustrated in the mechanical analysis in Fig. 4.8(b). Assuming the axial force allocation of the web is negligible, the upper and lower flanges would each bear half of the axial force,

$$F_A = \frac{Q}{2} \cdot \tan \Theta_V \tag{4.2}$$

where Q is the shear force applied to the beam. This axial force opposes the internal force in the upper flange while reinforcing the internal force in the lower flange, thereby reducing the difference between the internal forces. To demonstrate the relationship between axial force and the internal force difference, the differences of internal force for VN30-O and VN30-M were summarized in Fig. 4.9. The vertical axis represents the internal force difference ΔF. The black solid line represents the internal force difference $\Delta F_{VN30\text{-}M}$, while the dashed line represents the internal force difference $\Delta F_{VN30\text{-}O}$. The difference between $\Delta F_{VN30\text{-}O}$ and $\Delta F_{VN30\text{-}M}$, calculated from $\Delta F_{M\text{-}O} = \Delta F_{VN30\text{-}M} - \Delta F_{VN30\text{-}O}$, is represented by the red line in the figure.

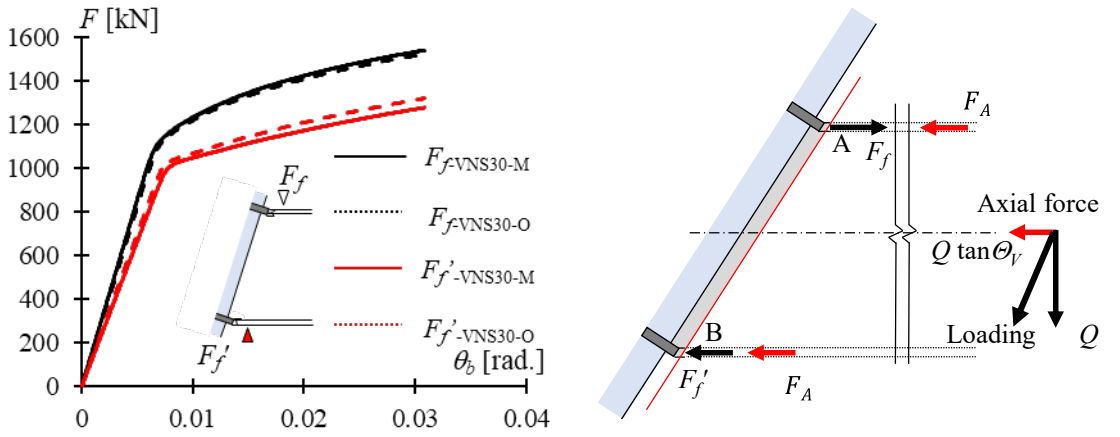

(a) Internal force of flange (b) Mechanical analysis of beam-end

Fig.4.8 Loading behavior of numerical analysis.

The calculated value ΔF_{cal}, given by $\Delta F_{cal} = Q\tan\Theta_V$, is represented by the red dotted line. From the internal force difference $\Delta F_{VN30\text{-}O}$ and $\Delta F_{VN30\text{-}M}$, it is evident that significant fluctuations occur as the beam flange enter plastic state. This occurs due to the unequal internal forces in the upper and lower flanges. The upper flange yielding earlier than the lower flange. Furthermore, comparing the calculated values ΔF_{cal} and the simulation results $\Delta F_{M\text{-}O}$, the value of $\Delta F_{M\text{-}O}$ is approximately half of ΔF_{cal}, indicating that the beam web absorbs nearly half of the axial force component. As a result, it can be concluded that under the loading mode parallel to the column, the axial force component mitigates the phenomenon of internal force concentration in the upper flange. However, since the axial force component is shared approximately equally between the flange and the web, the internal force difference between the upper and lower flanges cannot be entirely eliminated.

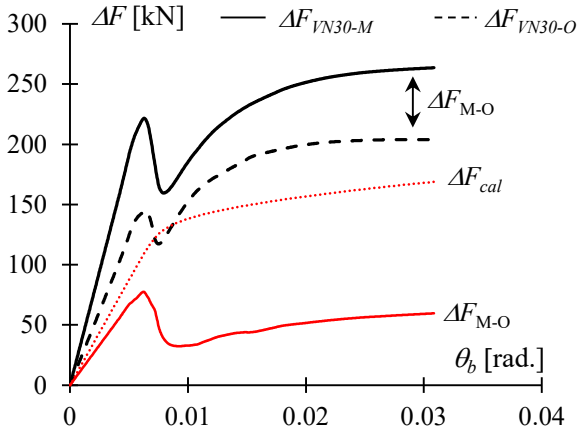

Fig.4.9 Comparison of the internal force difference between different loading direction.

4.2.5.2 Effect of different vertical oblique angle

For the experiments conducted in Chapter 3, it was confirmed that the internal force difference between the upper and lower flanges gradually increases with the vertical oblique angle. However, only the specimens with 15° and 30° vertical oblique angles were loaded. To comprehensively understand the effect of various oblique angles on the beam-end connections, numerical analysis with oblique angle as the parameter was conducted.

The detailed parameters of the specimens are summarized in Table 4.3. The vertical oblique angle of connection ranged from 0° to 30°, divided at intervals of 5°, resulting in a total of seven specimens being analyzed. In Chapter 3, it was observed that weld access holes in beam-end connections could affect the internal forces in the upper and lower flanges dur-

Table 4.3 Numerical analysis list of connections with vertical oblique angle

Spec.	Θ_V	Section	Span L	Loading method	Loading direction
VN0	0	BH 500x200x9x19	3000	Cycle loading	Perpendicular to beam
VN5	5				
VN10	10				
VN15	15				
VN20	20				
VN25	25				
VN30	30				

ing plastic deformation. Therefore, all specimens in this analysis used the beam-end connections without weld access holes. In addition, aside from the vertical oblique angles, the material properties, boundary conditions, and other relevant settings of the models were consistent with those described in Seciton 4.2.

The hysteretic curves obtained from the FE analysis are shown in Fig. 4.10, where the red line represents the FE analysis results and the black line corresponds to the experimental results for specimen VN15. It can be observed that the analytical results closely match the experimental results. To continuously compare the effect of different vertical oblique angles on the internal forces at the beam flange, the internal forces at the AB and AB' sections of the flange were extracted using the method described in Eq. (4.2). The internal forces obtained from the FE analysis for the AB and AB' sections are summarized in Fig. 4.11.

The internal force of beam flange in Fig.4.11(a) are extracted from the elastic state (θ_b=0.005 rad.), while those in Fig. 4.11(b) are extracted from plastic state (θ_b=0.025 rad.). To validate the effectiveness of the mechanisms of force transmission introduced in section 3.1 ,the calculations of internal force in beam flange using Eqs. (3.4) and (3.5) are also included in the figures. The vertical axis in the figures represents the ratio of the flange internal force at each oblique angle ($F_{\Theta v}$) to the force without an oblique angle (F_0) allowing for comparison of the trends in the internal forces. The horizontal axis indicates the oblique angle of the specimens. A comparison of the internal forces at AB and AB' sections shows that regardless of the oblique angle, the internal force at the upper flange is the largest, followed by

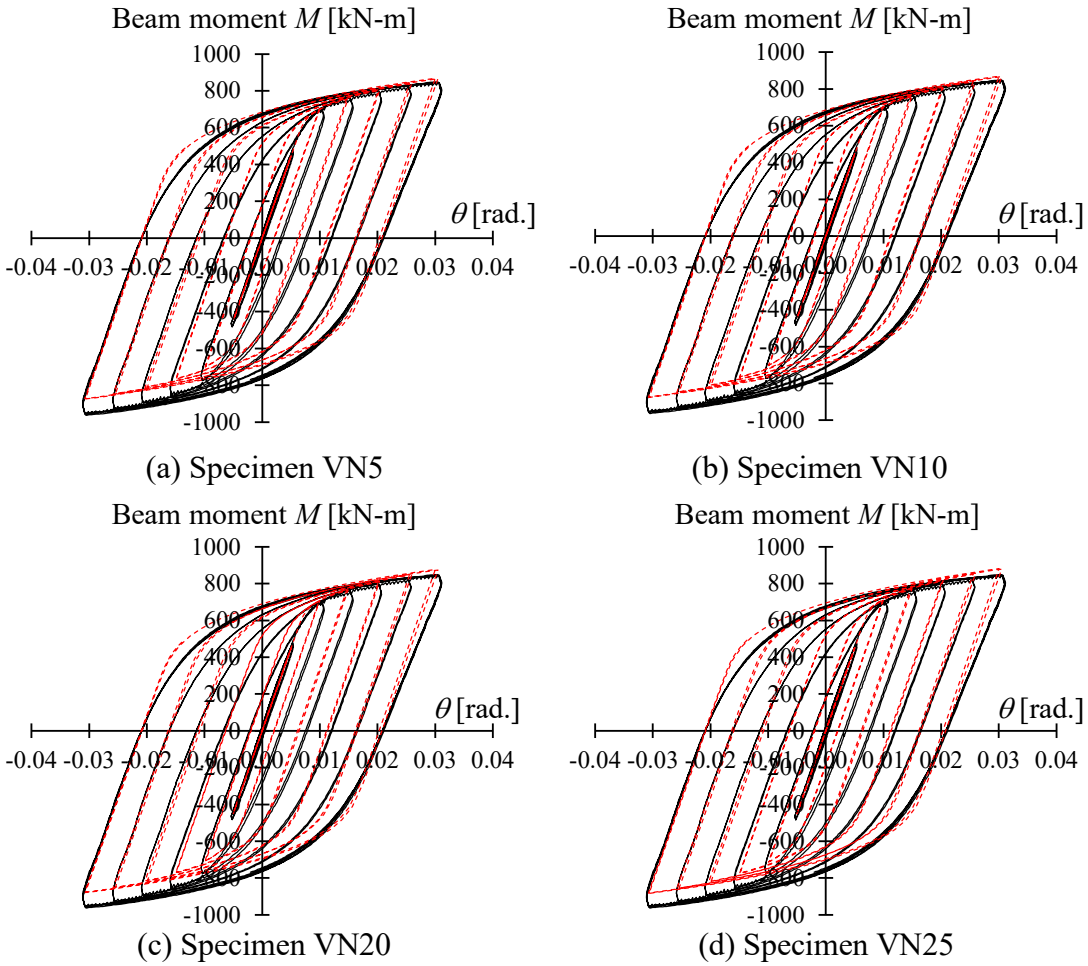

(a) Specimen VN5 (b) Specimen VN10

(c) Specimen VN20 (d) Specimen VN25

Fig.4.10 Hysteretic curves of FE analysis.

the force at Point B, with the smallest force at Point B'. This result aligns with the experimental result. A comparison of the internal forces in the upper and lower flanges at different oblique angles reveals a linear relationship: the internal force in the upper flange increases, while that in the lower flange decreases as the oblique angle increases. This trend closely matches the calculated values $F_{f\text{-}cal}$ and $F_{f\text{-}cal}$'. Furthermore, a comparison of the elastic state (Fig.4.11(a)) and plastic state (Fig.4.11(b)) shows that the internal force difference between the upper and lower flanges decreases after the beam-end enters the plastic state.

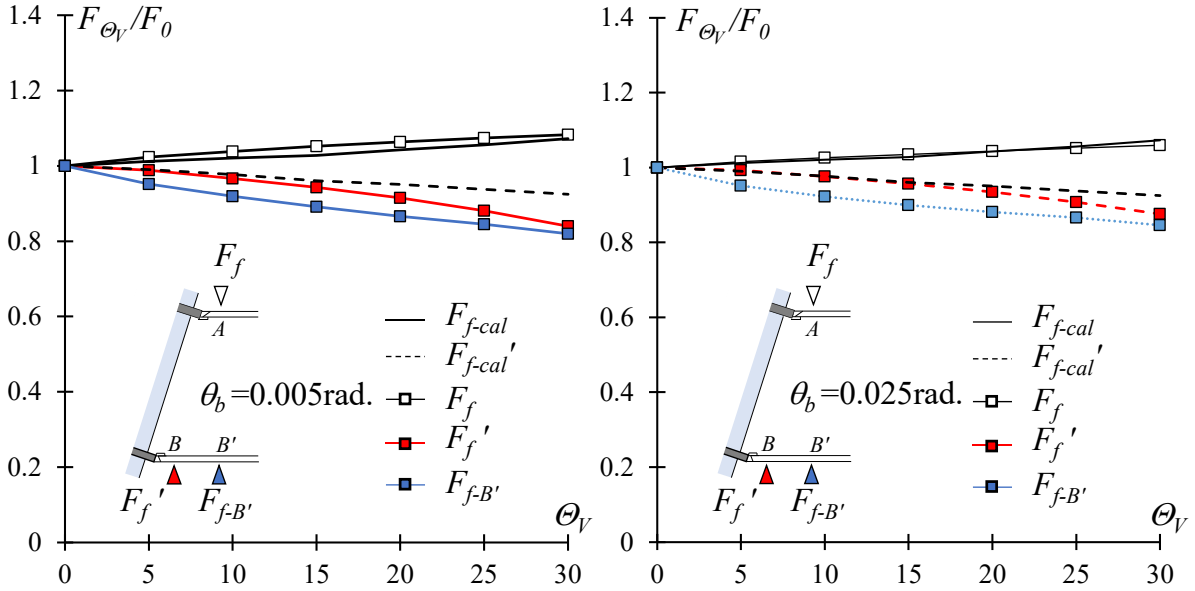

(a) Internal force of flange at θ_b=0.005rad. (b) Internal force of flange at θ_b=0.025rad.

Fig.4.11 Internal force of the beam-end flange at section AB and AB'.

4.2.5.3 Effect od different span and beam depth

In the mechanism analysis presented in Section 3.1, the internal forces of the upper and lower flanges were calculated using Eq. (3.4) and (3.5). These equations include the beam span and depth, indicating that both parameters influence the distribution of internal forces in the beam flanges. To confirm the effects of beam span and depth, a numerical analysis was conducted with span and depth as parameters.

All specimens used in the analysis of this chapter are summarized in Table 4.4. The parameters of the specimens are beam depth and span. The beam sections of the specimens are RH400×200×8×13 (D4 series) and RH300×200×8×12 (D3 series), both of which are commonly used in Japan. The beam spans of the specimens were set as 4m (L4 series) and 2m (L2 series) to represent long and short spans, respectively. In the previous chapter, it was demonstrated that the internal force of the beam flange changes linearly with the oblique angle. Therefore, under each parameter for beam section and span, only the oblique angles of 0°, 15°, and 30° were considered to investigate the impact of beam section and span on the internal force of the beam-end. Additionally, during the model generation process, the same approach as described in Fig. 4.1 was adopted. When the beam section changed, the size of each mesh was appropriately increased or decreased to maintain consistency in the number of elements at the beam-end.

The results of the FE analysis were evaluated separately for the elastic and plastic

Table 4.4 Numerical analysis list of connections with different beam section and span.

Spec.	Θ_V	Section	Span L	Loading method	Loading direction
VN0-L4	0	BH 500x200x9x19	4000	Cycle loading	Perpendicular to beam
VN15-L4	15				
VN30-L4	30				
VN0-L2	0		2000		
VN15-L2	15				
VN30-L2	30				
VN0-D4	0	RH 400x200x8x13	3000		
VN15-D4	15				
VN30-D4	30				
VN0-D3	0	RH 300x200x8x12			
VN15-D3	15				
VN30-D3	30				

states. Firstly, the internal forces of the upper and lower flanges, F_f and F_f', extracted from the elastic state (θ_b=0.005 rad.) were summarized in Fig. 4.12. The FE analysis results for beam depth and span are shown in Fig. 4.12(a) and (b), and Fig. 4.12(c) and (d), respectively. The vertical axis represents the ratio F_f/F_0 or F_f'/F_0, while the horizontal axis represents beam depth in Fig. 4.12(a), (b) and beam span in Fig. 4.12(c), (d). The squares markers in the figure illustrate the internal forces of flange, while the gray line denotes the calculated values of F_f/F_0 *and* F_f'/F_0 derived using Eq. 4.3 which was derived from Eq.(3.4)~(3.5)

$$\frac{F_{f\theta}}{F_{f0}} = 1 + \frac{D_b}{2L}\tan\Theta_V, \frac{F_{f\theta}'}{F_{f0}} = 1 - \frac{D_b}{2L}\tan\Theta_V \tag{4.3}$$

Comparing Fig. 4.12(a), (b), it can be observed that for the same oblique angle, as the beam depth increases, the internal force in the upper flange increases, while the internal force in the lower flange decreases. Comparing FE results with the calculated values, the trends in internal force changes are captured, though the calculated value is slightly underestimated. In contrast, the results in Fig. 4.12(c), (d) indicate that increasing the beam span causes a decrease in the internal force of the upper flange and an increase in the internal force of the lower flange. The results of the calculated value and FE analysis results demonstrate a corre-

lation, indicating that the calculated values effectively predict the changes of internal forces in beam-end flange.

To further investigate the internal forces during the plastic state (θ_b=0.025 rad.), the comparison of internal force in beam flange between elastic and plastic state are shown in Fig. 4.13. In the figure, the red and black lines represent the internal forces of beam flange in the elastic state (θ_b=0.005 rad.), while the square marks represent the internal forces in the plastic state. Comparing the internal forces in the elastic and plastic states reveals that the difference of internal force decreases in the plastic state. This phenomenon is consistent with experimental result in Chapter 3. However, when comparing the effects of beam depth and

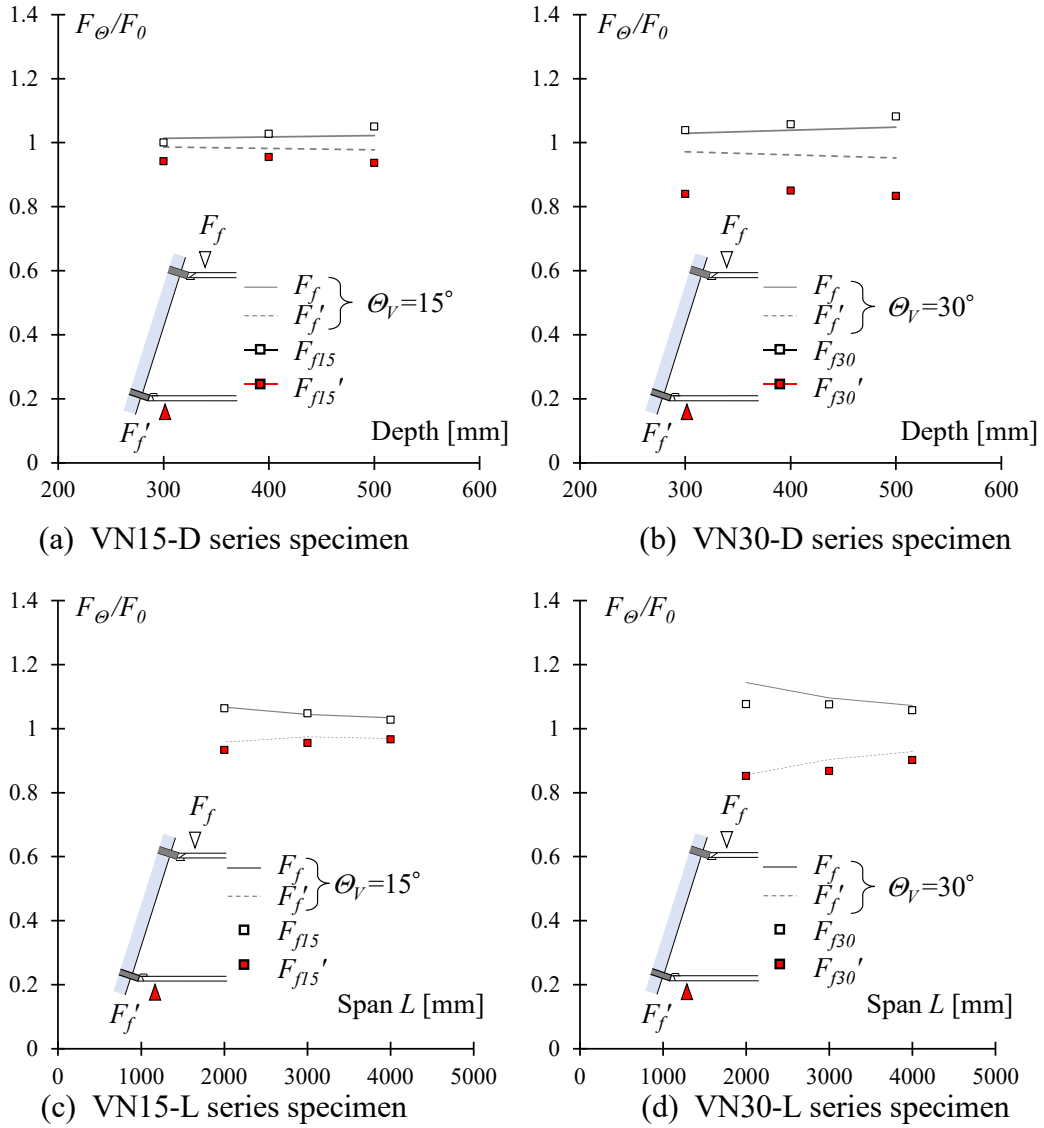

(a) VN15-D series specimen (b) VN30-D series specimen

(c) VN15-L series specimen (d) VN30-L series specimen

Fig.4.12 Internal force of flange vs calculation in elastic state.

span, it is evident that for longer spans, the changes in difference of internal force are negligible. Notably, in the L4 series specimens (Span=4000mm), the difference of internal force difference at the beam-end shows almost no reduction at plastic state.

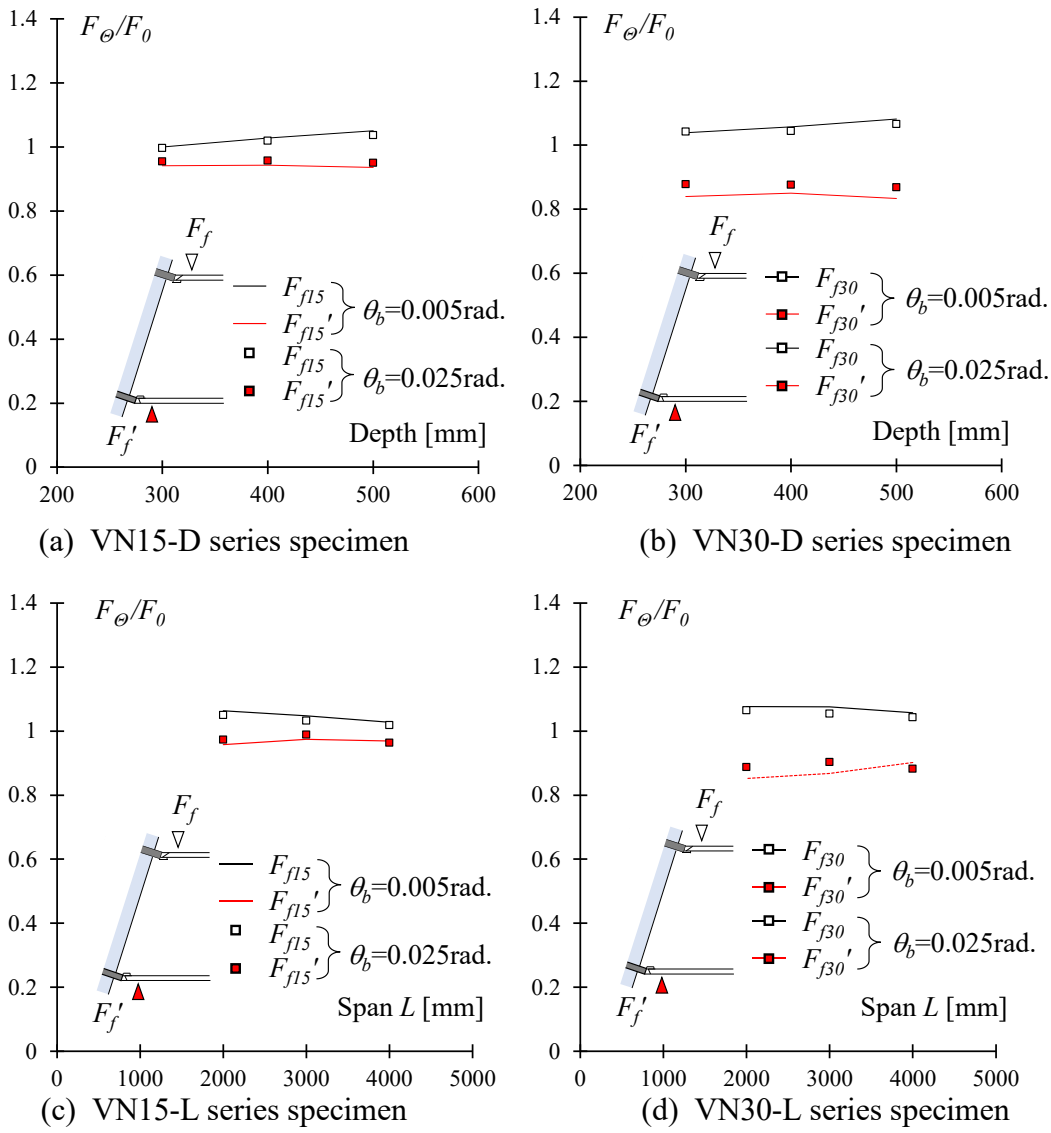

(a) VN15-D series specimen (b) VN30-D series specimen

(c) VN15-L series specimen (d) VN30-L series specimen

Fig.4.13 Internal force of flange in elastic state vs plastic state.

4.3 FEA results of beam-end with horizontal oblique angle

In the experiments conducted in Chapter 2 on beam-end connections with horizontal oblique angles, it was observed that the strain distribution in the beam-end flanges concentrated in the obtuse angle zone, while the strain in the acute angle zone became significantly smaller. This result indicates that the oblique angle at the beam-end leads to an uneven strain distribution. In the experiment, strain distribution at the beam-end was measured using strain gauges, but more detail is required to capture the strain distribution. Additionally, only one type of beam section and span was used, and further investigation is needed to determine the effects of beam section and span on the behavior of connections. Since the experimental data were limited to a specific beam section and span, further numerical analysis is required to generalize the findings. In this section, FE analysis will be conducted to replicate the experimental results, while numerical analysis will evaluate the effects of beam section and span.

4.3.1 Model construction

The FE analysis model was generated using ABAQUS 2020 software. Solid elements using 8-node linear reduced integration were employed to construct the model. Taking NS30 specimen as an example, the detailed setup of the specimen is shown in Fig. 4.14. To ensure consistency in the beam-end analysis model across all simulations in Chapter 4, the column component and welding details were omitted. The boundary conditions at the beam-end and loading points were kept consistent with those described in section 4.2. The mesh configura-

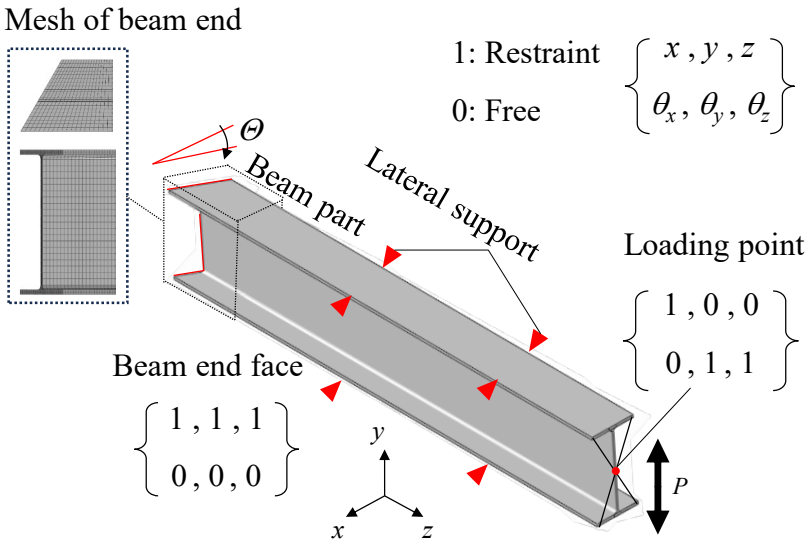

Fig.4.14 FE models of beam-end connection with horizontal oblique angle (NS30).

tion is illustrated in Fig. 4.14. Due to the asymmetrical shape of the beam flange, the mesh was refined in greater detail to enable more accurate simulation of the stress-strain relationship at the beam-end.

4.3.2 Comparison of experimental results

Fig. 4.15 provides a comparison of the hysteretic curves derived from the FE analysis and experimental result. Only minor differences were observed in the Bauschinger region.

Table 4.5 Summary of FE analytical results.

Spec.	K_{FEA} [N/mm]	K_{exp} [N/mm]	K_{FEA}/K_{exp}	$M_{max\text{-}FEM}$ [kN-m]	$M_{max\text{-}exp}$ [kN-m]	$M_{max\text{-}FEM}/M_{max\text{-}exp}$
NS0	10.9	13.1	0.83	582.7	559.2	1.04
NS15	10.7	12.7	0.84	600.4	565.7	1.06
NS30	10.7	12.0	0.89	599.5	571.0	1.05
NS45	10.9	13.2	0.83	603.1	572.1	1.05

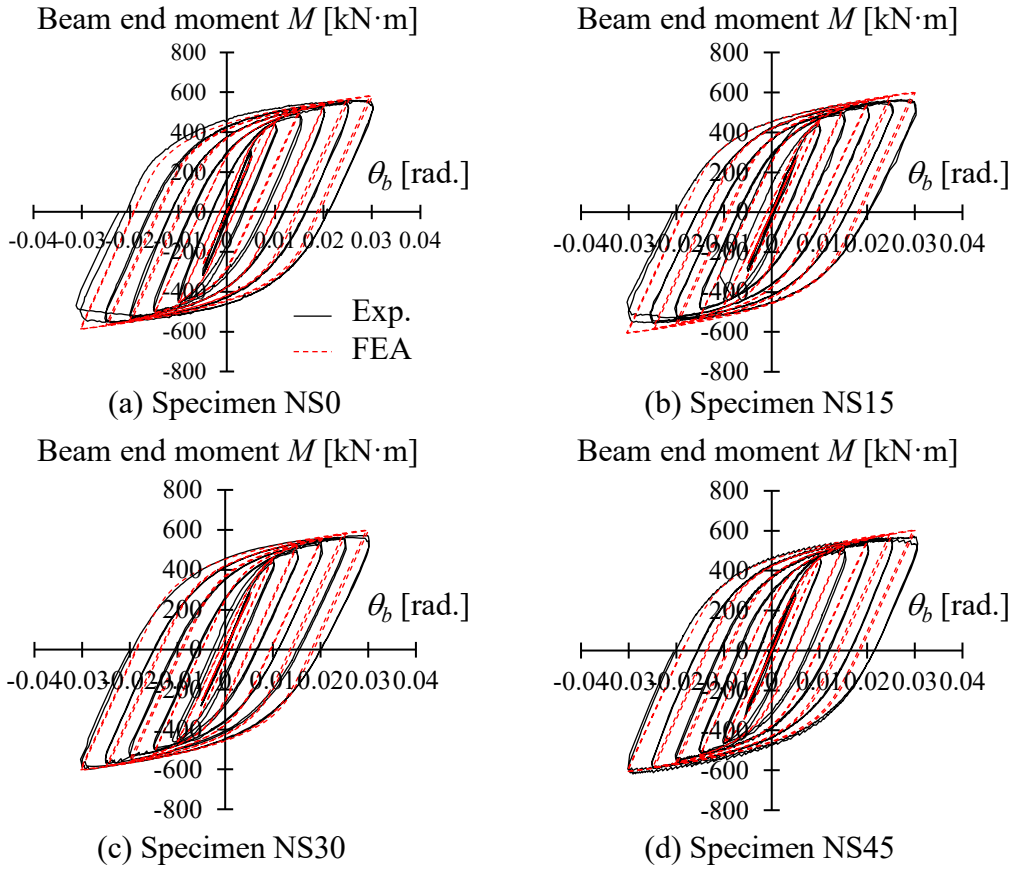

(a) Specimen NS0 (b) Specimen NS15

(c) Specimen NS30 (d) Specimen NS45

Fig.4.15 Hysteretic curves of FE analysis.

The FE analytical results corresponded closely to the experimental result. The maximum moment and elastic stiffness values obtained from the analysis are summarized in Table 4.5. The ratio of the maximum moment and stiffness between the experimental and analytical results was consistently around 1.0, indicating that the horizontal oblique angle had minimal effect on the maximum moment or stiffness.

4.3.3 Analysis of stress distribution at beam-end

The plastic strain distribution along the *y*-direction (PE22) at the beam-ends of each specimen is illustrated in Fig. 4.16. For specimens NS0 and NS15, The plastic strain gradually accumulated at the two edges of the beam-end during deformation. In contrast, for specimens NS30 and NS45, the plastic strain concentrates in the obtuse angle zone of the beam-end (the red box in the figure), while the plastic strain in the acute angle zone decreases. This result aligns with the strain distribution observed in the experiments of Chapter 2, confirming

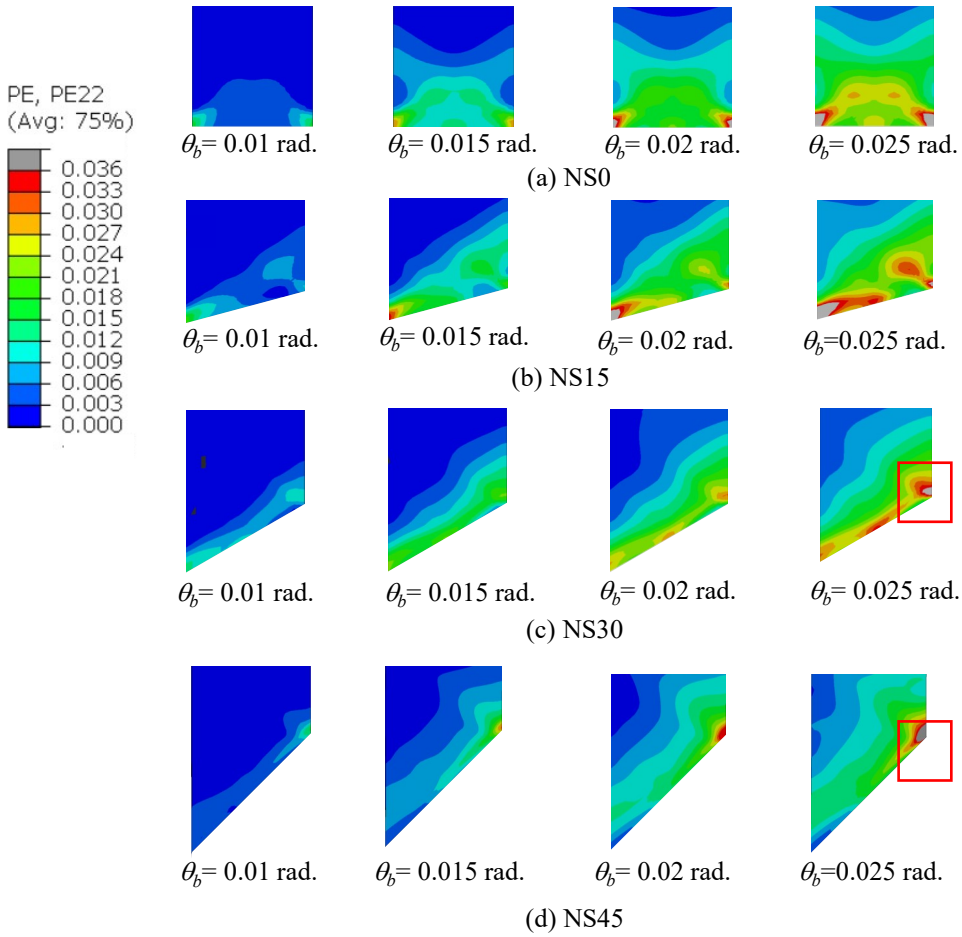

Fig.4.16 Plastic strain distribution in *y*-direction (PE22) of FE analysis.

the effectiveness of the analysis for beam-end connections with horizontal oblique angles.

To validate the effectiveness of the FE analysis for strain distribution in the plastic state (θ_b=0.025rad.), a comparison between experimental and analytical strain distributions is presented in Fig. 4.17. The vertical axis represents the strain, while the horizontal axis represents the beam width. The black squares indicate the experimental strain distribution at the *u*-section of beam-end , and the red line represents the corresponding strain distribution from the FE analysis. Since only five strain gauges were used in the experiment at the *u*-section, the strain at the beam-end edge could not be directly measured. Therefore, to estimate the strain at the edge in experimental result, the strain closest to the edge were interpolated with a straight line. The line was then extended to the beam edge, and the strain at the intersection of the extended line and the beam edge was estimated as the strain at that position, represent-

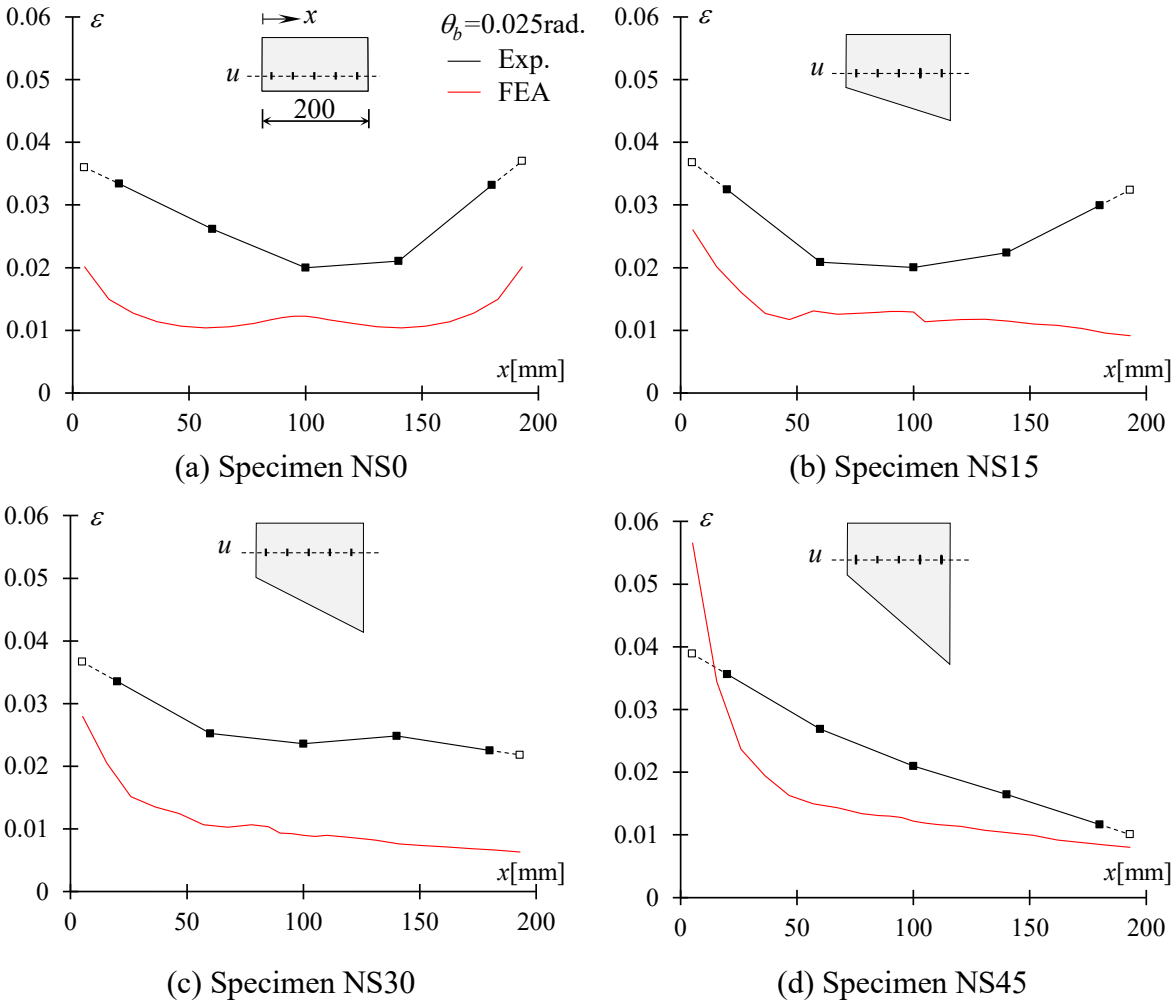

(a) Specimen NS0 (b) Specimen NS15

(c) Specimen NS30 (d) Specimen NS45

Fig.4.17 Strain distribution at *u*-section of FE analysis.

ed by the white squares in the figure.

Comparing the experimental and analytical results, it can be seen that although the FE analysis values are slightly lower than the experimental strains, they effectively capture the strain variations at different positions along the *u*-section. Remarkably, in the FE analysis results for NS30 and NS45, the strain concentration effect is well reproduced.

4.3.4 Parameter analysis

The strain distribution results from the previous chapter confirm that the FE analysis can reliably replicates the experimental result. Because only specimens with horizontal oblique angles of 15°, 30°, and 45° were tested, the strain distribution analysis of experiment revealed a nonlinear relationship between strain concentration and the oblique angle. To better fill the gap in the untested oblique angle range, numerical analysis will be conducted for specimens at various oblique angles. In addition, as in Section 4.2, the effects of beam span and beam width on beam-end connections with horizontal oblique angle will also be examined.

4.3.4.1 Effect of different horizontal oblique angle

To confirm the relationship between the oblique angle and strain concentration in the

Table 4.6 Numerical analysis list.

Spec.	Θ_H	Section	Span L	Loading method
NS0	0	RH 400x200x8x13	2200	Cycle loading
NS5	5			
NS10	10			
NS15	15			
NS20	20			
NS25	25			
NS30	30			
NS35	35			
NS40	40			
NS45	45			

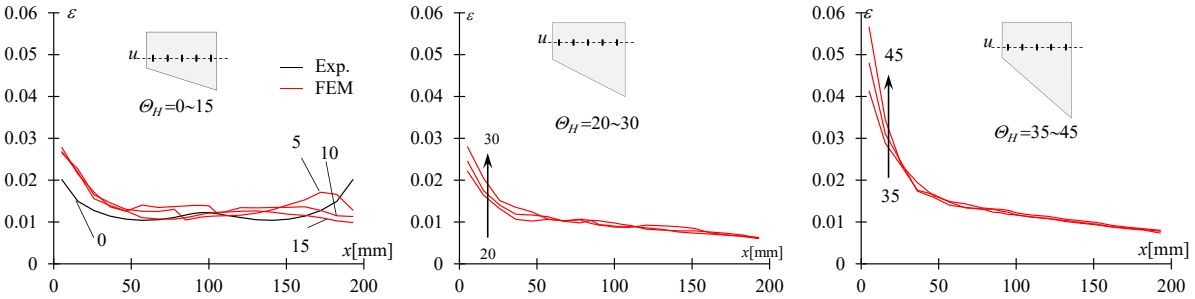

(a) Specimen NS0 (b) Specimen NS15 (a) Specimen NS0

Fig.4.18 Strain distribution at *u*-section of FE analysis.

obtuse zone of the beam-end, specimens with horizontal oblique angles from 0° to 45° were used for numerical analysis. The oblique angles ranged from 0° to 45°, divided into 5° intervals, resulting in a total of ten specimens. The list of numerical analysis specimens is summarized in Table 4.6. The beam section and span of numerical analysis were consistent with those used in the experiments, and the analysis conditions remained the same as in Section 4.3.1.

The strain distribution extracted from the *u*-section of the beam-end is illustrated in Fig. 4.18. FE analysis results for oblique angles from 0° to 15° are shown in Fig.4.18(a), for 20° to 30° in Fig.4.18(b), and for 35° to 45° in Fig.4.18(c). In each figure, NS0 specimen is represented in black line for comparison, while the other specimens are shown in red. From Fig.4.18(a), it can be seen that for oblique angles range between 5° and 15°, strain concentration at the obtuse zone is only slightly greater than that of the 0° specimen, which aligns with the experimental results. In Fig.4.18(b), for oblique angles in the range of 20° to 30°, strain

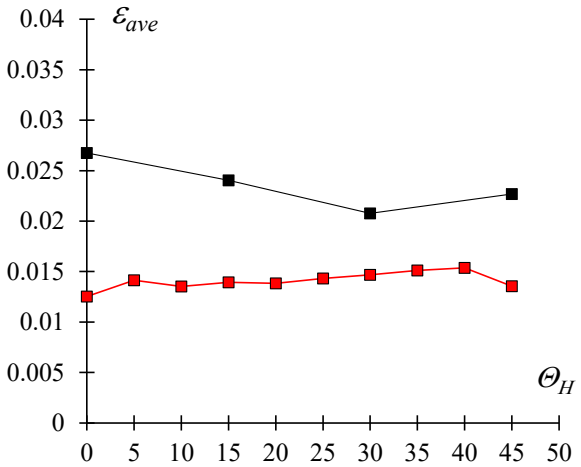

Fig.4.19 Average strain ε_{ave} of *u*-section in different horizontal oblique angle.

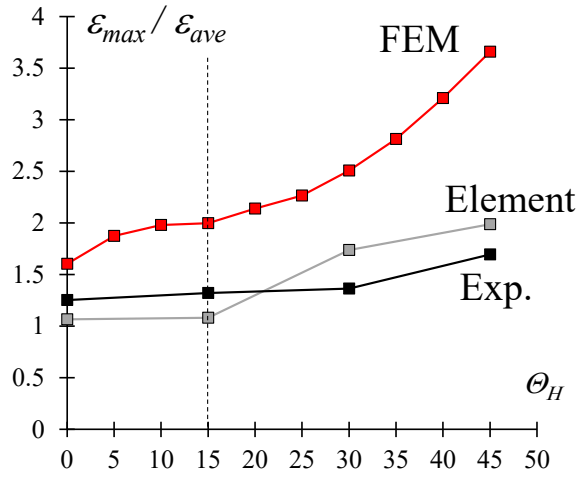

Fig.4.20 Strain concentration ratio in different horizontal oblique angle.

concentration in the obtuse zone gradually increases with increasing oblique angle, while the strain in the acute angle zone decreases. But in Fig.4.18(c), for oblique angles between 35° and 45°, the strain concentration has rapidly increased as the oblique angle grows.

To further clarify the change in strain concentration, the average strain ε_{ave} at the *u*-section was defined, and its relationship with the oblique angle is illustrated in Fig.4.19. The experimental results are indicated by black squares, while the analysis results are shown by the red squares. It is evident that, in both experiment and FE analysis results, the average strain ε_{ave} at the *u*-section remains nearly constant regardless of the oblique angle. To further evaluate the degree of strain concentration, the strain concentration ratio was defined as the ratio of the maximum strain ε_{max} at the *u*-section by the average strain ε_{ave}. The strain concentration ratio is plotted on the vertical axis, and the oblique angle on the horizontal axis. Both experimental and FE analysis results are summarized in Fig. 4.20. In the figure, the red squares represent the FE analysis results, the gray squares show the element test results from Chapter 2.3, and the black squares depict the experimental results. Comparing the strain concentration ratio ε_{max} / ε_{ave} from the figure, it can be seen that although all the experimental results show a slightly lower strain concentration ratio, both the experimental and analytical results show a synchronized increase. From the trend observed in the FE analysis results, when the oblique angle is up to 15°, the strain concentration ratio barely increases and remains below 2. After 15°, the ratio increases rapidly with increasing oblique angle, and for oblique angles greater than 30°, the ratio rises even faster. So it can be concluded that the beam-end with a horizontal oblique angle should ideally not exceed 15°.

4.3.4.2 Effect of different beam span and depth

To evaluate the influence of beam width and span on the beam-end connection with horizontal oblique angles, a numerical analysis was conducted using beam width and span as the primary variables. The details of the specimens used in the numerical analysis are summarized in Table 4.7. The specimens are categorized into two series based on the parameters: beam width (B series) and beam span (L series). Each series includes specimens with oblique angles of 15°, 30°, and 45°. In the B series, beams with widths of 100 mm (B1), 200 mm (as used in the experiments), and 400 mm (B4) were used. In the L series, to investigate the effect of span, the beam span was varied to half (L1) and double (L4) of the experiment condition. The results of the numerical analysis are illustrated in Fig. 4.21, where the beam span and width are plotted on the horizontal axis and the strain concentration ratio on the vertical axis. The dashed lines represent the strain concentration ratio in the elastic state (θ_b=0.005 rad.), while the solid lines represent those in the plastic state (θ_b=0.025rad.).

For the B series (Fig. 4.21(a)), it can be observed that as the beam width increases, the strain concentration ratio also increases. Comparing the strain concentration ratio of the elastic and plastic state, regardless of the beam width, the strain concentration ratio in the plastic

Table 4.7 Numerical analysis list of beam span and width.

Spec.	Θ_H	Section	Span L	Loading method
NS15-L1	15	RH 400x200x8x13	1100	Cycle loading
NS30-L1	30			
NS45-L1	45			
NS15-L4	15		4400	
NS30-L4	30			
NS45-L4	45			
NS15-B4	15	RH 400x400x13x21	2200	
NS30-B4	30			
NS45-B4	45			
NS15-B1	15	RH 200x100x5.5x8		
NS30-B1	30			
NS45-B1	45			

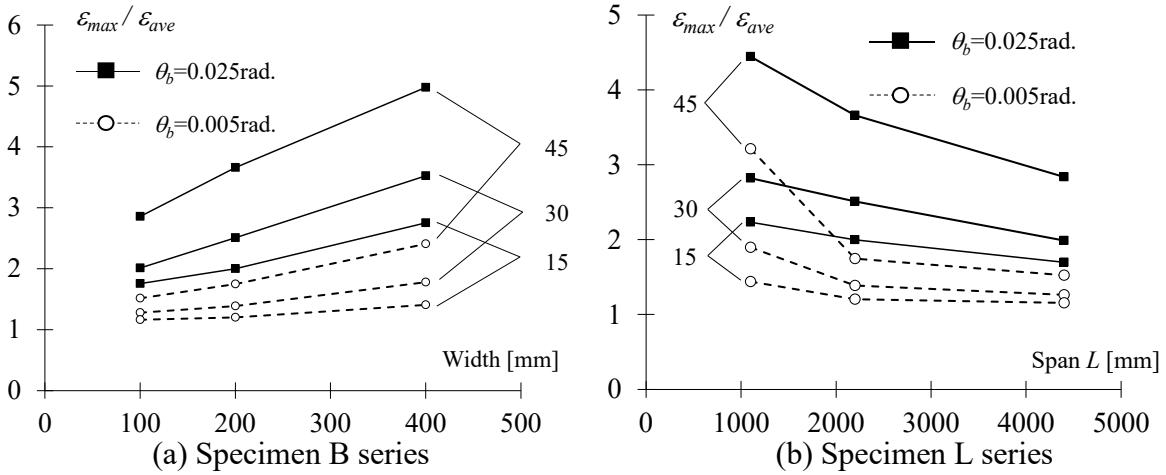

(a) Specimen B series (b) Specimen L series

Fig.4.21 Strain concentration ratio in different beam span and width.

state is nearly double that in the elastic state. In the L series results (Fig.4.21(b)), as the beam span increases, the strain concentration ratio gradually decreases. However, when comparing strain concentration ratio of the elastic and plastic state, it can be seen that, for beam spans of 2200 and 4400 mm, the change in the strain concentration ratio between elastic and plastic states is approximately twofold. In contrast, for span 1100 mm, the change in the strain concentration ratio decreases to about 1.5 times. This indicates that a shorter beam span reduces the strain concentration ratio in the plastic state.

To predict the strain concentration ratio, a mechanical analysis was conducted on the strain at the beam-end. When the beam is subjected to a shear force, the corresponding loading condition is illustrated in Fig. 4.22. Based on the previous experimental and analytical findings, it is known that the irregular part of the beam-end tends to develop strain concentration, resulting in uneven deformation. However, away from the beam-end, the deformation gradually becomes uniform again.

To simplify the analysis of strain at the beam-end, the irregular deformation beam part was defined as part A, while the normal beam part is defined as part B. The small incremental deformation in the boundary area of part A and B is labeled as Δx (highlighted in yellow in the figure). The edge length on the side of acute zone and the obtuse zone in part A is defined as l_a, l_b, respectively, while the flange width is B. Then the flange width is divided infinitely, with each segment width labeled as Δi. And the length of each segment in part A can be represented by the following equation.

The strain in section l_i can be expressed by Eq.(4.5).

Then, the ratio of the strain at the acute zone ε_t to the strain at the obtuse zone ε_b can

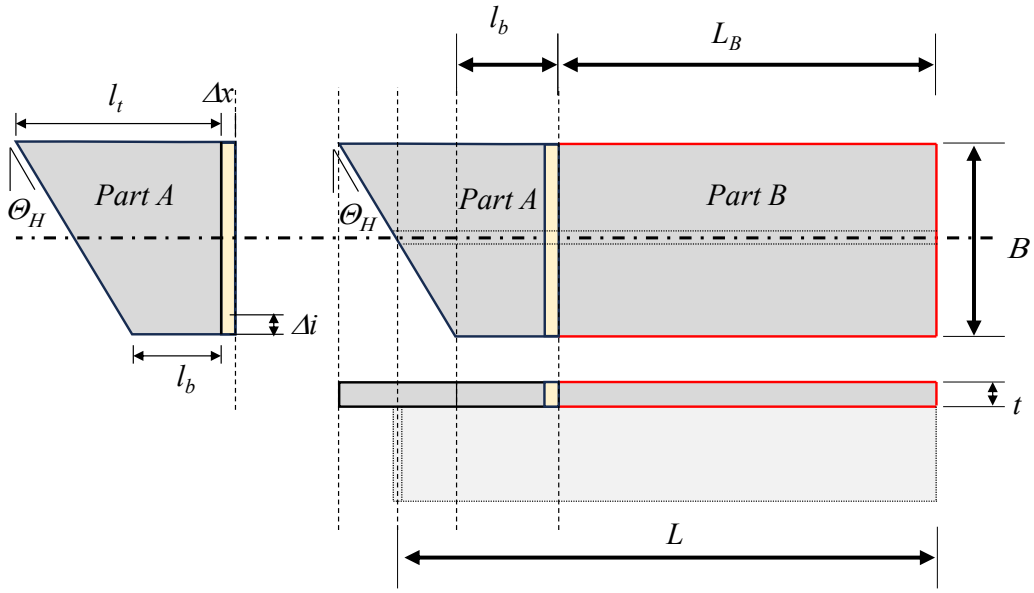

Fig.4.22 Strain analysis of beam flange with horizontal oblique angle.

$$l_i = l_b + i\tan\Theta_H \tag{4.4}$$

also be represented by the following equation.

$$\varepsilon_i = \frac{\Delta x}{l_i} \tag{4.5}$$

Therefore, based on Eq. (4.4) to (4.6), the strain concentration ratio can be expressed by the following equation.

$$\frac{\varepsilon_b}{\varepsilon_t} = \frac{l_t}{l_b} = 1 + \frac{B}{l_b}\tan\Theta_H \tag{4.6}$$

Additionally, based on the FE analysis from the previous chapter, it can be concluded that the strain concentration ratio is influenced by the beam span. This implies that there is a

$$\frac{\varepsilon_b}{\varepsilon_{ave}} = \frac{l_{ave}}{l_b} = 1 + \frac{B}{2l_b}\tan\Theta_H \tag{4.7}$$

proportional relationship between the lengths of part A and part B. Therefore, the relationship α can be defined as

Thus, the relationship between l_b and L can be expressed as follows.

The calculation result of strain concentration ratio represented by α is plotted alongside the FE analysis results in the elastic state (Fig. 4.21). The comparison results

$$\alpha = \frac{L_B}{l_b} \tag{4.8}$$

$$l_b = \frac{\alpha}{1+\alpha}\left(L - \frac{B}{2}\tan\Theta_H\right) \tag{4.9}$$

are presented in Fig. 4.23. In the figure, the calculation result are shown in red lines. By comparing the red line with the FE analysis results, it can be concluded that when α =0.1, meaning the length l_b is one-tenth of L_b, the calculated result can accurately predict the strain concentration ratio at the beam-end.

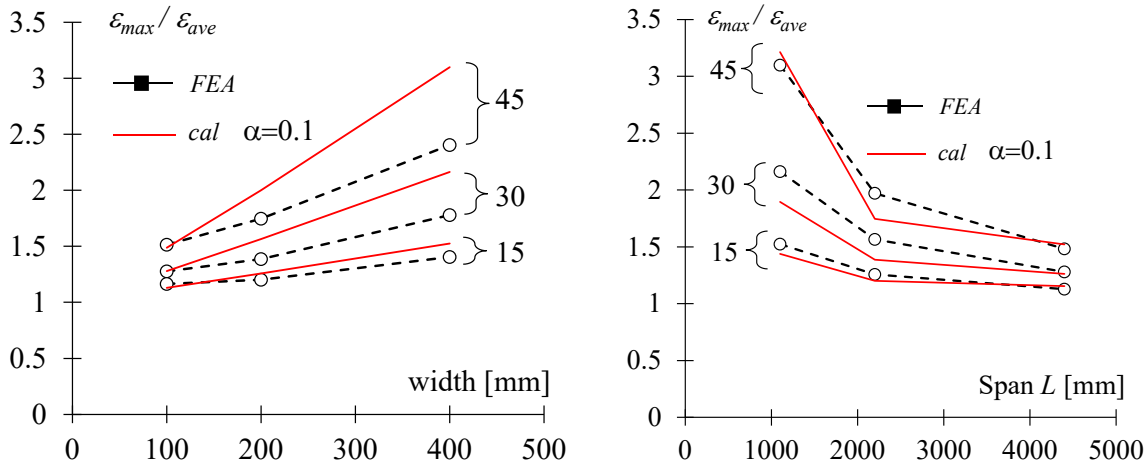

(a) Specimen B series (b) Specimen L series

Fig.4.23 Comparison between strain concentration ratio from calculation and FEA result.

4.5 Conclusions

In this chapter, finite element (FE) analysis using ABAQUS was conducted for beam-end connections with vertical or horizontal oblique angles. The FE results accurately reproduced the seismic behavior observed in the experiments and confirmed the validity of FE analysis for beam-end connections with oblique angles. The numerical analysis investigated the effects of beam section, span, and loading mode, revealing their influences on the behavior of beam-end connections with oblique angles. The main conclusions of this chapter are summarized as follows:

(1) In vertical oblique angle analysis, FE analysis accurately reproduced the experimental results, presenting the internal forces in beam flange at the failure section. These internal forces were compared with the calculated results from the mechanism analysis presented in Chapter 3, confirming its reliability.

(2) More detailed numerical analyses of various vertical oblique angles were conduct-

ed. At each vertical oblique angle, the internal forces of beam flange in failure section were presented. The results indicated that the changing of internal force of the upper at the beam-end increased linearly with the vertical oblique angle. The effectiveness of the mechanism analysis for calculating internal forces was verified.

(3) In the numerical analysis of vertical oblique angle, the effects of loading mode, beam depth, and span were investigated. Under a load paralleled to the column, the difference of internal force between the upper and lower flanges was reduced by half, suggesting that the effect of vertical oblique angle can be largely neglected in long-term loading. It was also found that greater beam depth and shorter span amplified the effect of the oblique angle, increasing the internal force difference. The numerical analysis results show that the mechanism analysis effectively captured the impact of beam depth and span.

(4) FE analysis of beam-end connections with horizontal oblique angles was conducted, reproducing the hysteretic behavior obtained in the experiment. The change of plastic region at the beam-end was analyzed for different horizontal oblique angles. The strain distribution was compared with experimental results, demonstrating that the FE analysis accurately replicates the strain concentration observed in the experiments.

(5) A numerical analysis with various horizontal oblique angles was given. The numerical analysis result showed the continuous change of the strain concentration ratio in the obtuse angle zone. The results indicated that for the horizontal oblique angle smaller than 15°, strain concentration in the obtuse angle zone was insignificant, whereas the oblique angle ranges between 15° and 30°, it increased slightly. When the oblique angle larger than 30°, strain concentration increased sharply.

(6) Numerical analysis studying the effect of beam width and span on the beam-end connection with horizontal oblique angles was conducted. It was found that increased beam width and short span led to an increase of strain concentration ratio. Based on deformation conditions at the beam-end, strain condition was discussed, and an equation for predicting the strain concentration ratio was derived. The results showed that when the ratio of the strain concentration area to the uniform strain area was 0.1, the equation could effectively predict the strain concentration ratio.

References

[1] J. Zhao, J. Li, Y. Sun, Experimental and numerical study on overall buckling behavior of Q460 high-strength steel continuous beams with welded singly symmetric I-section, Eng. Struct. 280 (2023) 115678.

[2] T. Tankova, F. Rodrigues, C. Leitao, C. Martins, L. Simoes da Silva, Lateral-torsional buckling of high strength steel beams: Experimental resistance. Thin-Walled Struct, 164 (2021) 107913.

[3] D.S. Lee et al., Experimental study of low-cycle fatigue behavior of a welded flange-bolted web connection in steel moment-resisting frames, Earthquake Spectra 34.4 (2018) 1829-1846.

[4] L. Moussa, et al., Shear buckling and stress distribution in trapezoidal web corrugated steel beams, Thin-Walled Structures, 113 (2017) 13-26.

[5] J. P. Fatemeh, et al., Seismic behavior of through beam connection to steel box-column, J. Constr. Steel Res. 193 (2022) 107261.

[6] M. Haider , Y. Feng, Numerical study of intermeshed steel beam-column connections, J. Constr. Steel Res. 189 (2022) 107079.

[7] X. Wei, et al., Cyclic behaviour of welded stainless steel beam-to-column connections: Experimental and numerical study, J. Constr. Steel Res. 218 (2024) 108736.

[8] X. Ping, et al. Constitutive model of aluminum under variable-amplitude cyclic loading and its application to buckling-restrained braces. Journal of Materials in Civil Engineering 30.3 (2018) 04017304.

[9] M. Wójcik, A. Skrzat. Identification of Chaboche–Lemaitre combined isotropic–kinematic hardening model parameters assisted by the fuzzy logic analysis. Acta Mechanica 232.2 (2021) 685-708.

[10] R. Nascimbene, Penalty partial reduced selective integration: a new method to solve locking phenomena in thin shell steel and concrete structures, Curved and Layered Structures, 9 (2022) 352-364.

[11] P. J. Davis, and P. Rabinowitz, Methods of numerical integration. Courier Corporation, 2007.

[12] O.C. Zienkiewicz, R.L. Taylor, The finite element method: solid mechanics, Vol. 2. Butterworth-heinemann, 2000.

[13] H. Asada, Study on Steel Beam-to-column Connections Subjected to Axial Force and Bending part1-5, Summaries of Technical Papers of Annual Meeting Architectural Institute, Japan, 2023. pp. 879-880 (in Japanese).

CHAPTER 5

Conclusions and future works

5.1 Conclusions

This dissertation presents experimental and analytical investigations of beam-end connections with oblique angle in SMRF system. The following conclusions were made:

In **Chapter 2**, a stress state of beam flanges with oblique angles was analyzed, and failure section was identified. In the element test, a phenomenon was observed where strain concentration led to a reduction in plastic deformation capacity. In the full-scale experiments, specimens with oblique angles of 15°, 30°, and 45° were tested. The full-scale tests confirmed that connections with oblique angles exhibit stable hysteretic behavior. The study revealed that horizontal oblique angles significantly influence the strain distribution at the beam end. When the angle was below 15°, its effect on strain distribution at the beam end was relatively small. However, for specimens with angles of 30° and 45°, strain concentration became significant. The failure mode of the specimens indicated that the failure section was the *u*-section (the section perpendicular to the beam's axis), which was consistent with the results of the stress analysis. However, due to the occurrence of local buckling at the beam end, the reduction in plastic deformation capacity was not observed.

In **Chapter 3**, a mechanism analysis was presented to predict the internal forces in beam flanges and critical failure sections of beam-to-column connections with vertical oblique angles. To validate the results of the mechanism analysis, specimens with vertical oblique angle of 0°, 15°, and 30° were tested. The experimental results showed that beam-to-column connections with vertical oblique angle exhibited stable hysteretic behavior. By observing the number

of cycles to failure, it was evident that the plastic deformation capacity of the beam ends decreased as the oblique angle increased. Through an analysis of strain distribution at the beam-end, it was observed that the oblique angle had a significant effect on the strain distribution. For specimens with vertical oblique angles, the neutral axis at the beam end shifted upward, which aligned with the results of the mechanism analysis. Additionally, a comparison between specimens with and without weld access holes indicated that for the specimens with weld access holes, the deformation at the beam end was concentrated at the bottom of weld access hole.

In **Chapter 4**, a finite element (FE) analysis was performed to extend the experimental findings and analyze the behavior of beam-to-column connections with oblique angles. For vertical oblique angle analysis, FE analysis accurately reproduced the experimental results. More detailed numerical analyses of various vertical oblique angles were conducted. At each vertical oblique angle, the internal forces of beam flange in failure section were presented. The results show that internal force of the upper flange increased linearly with the vertical oblique angle. The effectiveness of the mechanism analysis for calculating internal forces was verified. In the numerical analysis of vertical oblique angle, the effects of loading direction, beam depth, and span were investigated. Under a load paralleled to axis of the column, the difference of internal force between the upper and lower flanges was reduced, suggesting that the effect of vertical oblique angle can be neglected. It was also found that greater beam depth and shorter span amplified the effect of the oblique angle. For horizontal oblique angle, the strain distribution was compared with experimental results, demonstrating that the FE analysis accurately replicates the experiments. Numerical analyses with various horizontal oblique angles were carried out. The results indicated that for oblique angle is less than 15°, strain concentration in the obtuse angle zone can be neglected, whereas the oblique angle is larger than 15°, strain concentration increased sharply. In the analysis of beam width and span, large beam width and short span led to an increase of strain concentration ratio. An equation for predicting the strain concentration ratio was also given.

5.2 Recommendations

This dissertation combines the experimental and analytical results with practical engineering design applications to provide the following recommendations for beam-to-column connections with oblique angles:

1. For beam-to-column connections with oblique angles, if the definition of span in this study is applied, the effect of the oblique angle on the maximum strength, elastic stiffness, and plastic behavior up to the maximum strength under cyclic loading is relatively small.
2. In the design of beam-to-column connections with oblique angles, shorter beam span and larger beam sections amplify the effect of the oblique angle. Therefore, when using the large oblique angle, it is recommended to use longer beam span or smaller beam sections in design to minimize the impact of the oblique angle.
3. In the design of beam-to-column connections with horizontal oblique angles, when the oblique angle is less than 15°, the strain concentration on the obtuse angle zone of the beam end is small, and the angle has little effect on the plastic deformation capacity of the connection. However, when the oblique angle exceeds 15°, strain concentration at the obtuse angle zone of the beam end increases significantly, reducing the plastic deformation capacity of the beam-to-column connection. It is recommended to use the extended diaphragm method to mitigate strain concentration at the beam end or using the cover plate (Fig, 5.1(b)) to enhance the obtuse zone of the beam-ends.
4. In the design of beam-to-column connections with vertical oblique angles, the oblique angle causes unequal internal forces between the upper and lower flanges. As the angle increases, the internal force in the upper flange of the beam-to-column connection rises linearly, resulting in reduction of plastic deformation capacity of beam-to-column connections. It is recommended to apply the haunch method (Fig. 5.1(a)) for beam ends to enhance the connection appropriately.

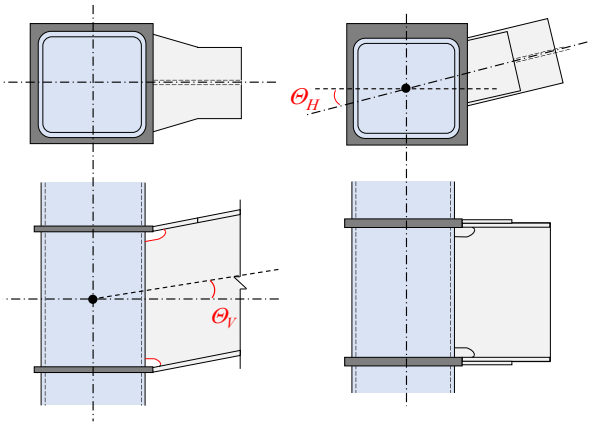

(a) Haunch method (b) Cover plate method

Fig. 5.1 Reinforcement method for beam-ends with oblique angle

5.3 Future works

This dissertation has focused on the structural behavior of beam-end connections with vertical or horizontal oblique angles. Through mechanism analyses and experiments, the effects of oblique angles on beam-ends were explained. Additionally, numerical analysis was employed to clarify the structural behavior of beam-end connections with oblique angles under different conditions. However, as a fundamental study, many issues remain to be explored. The following summarizes potential future works:

Future work 1: The structural behavior of beam-to-column connections with vertical and horizontal oblique angle.

In this dissertation, the specimens in Chapter 2 and 3 were classified into vertical and horizontal oblique angles. However, in practical applications, there are complex beam-to-column connections that incorporate both vertical and horizontal oblique angles. Whether the structural behavior of such connections is consistent with connections that have only one type of oblique angle remains unknown. Exploring this aspect could be a focus for future research.

Future work 2: The ultimate strength of panel zone in beam-to-column connections with oblique angle.

As introduced in the dissertation's introduction, previous studies have conducted experiments on panel zones under bidirectional loading. However, these experiments were either on isolated panel zones component or on beam-to-column connections without oblique angles. And in this dissertation, the structural behavior, failure modes, and stress-strain distribution of

the panel zone were not analyzed in either the experiments or the numerical analysis. Therefore, further experiments and analyses focusing on the panel zone in beam-to-column connections with oblique angles could be pursued in future work.

Future work 3: The deformation capacity of a cruciform beam-to-column connection with oblique angle.

In SMRF systems, beam-to-column connections typically function as a cross-shaped unit. While cantilever beams were used as specimens for both loading and numerical analysis in this dissertation, the potential effects of beam-end connections with oblique angle on other beam and column components also require evaluation. Particularly, for beam-to-column connections with vertical oblique angle, the connections changes the length of panel zone, making the configuration of the connection more complex. Additionally, the impact of oblique-angle beam-to-column connections on the seismic performance of the overall frame structure needs to be further investigated.

Future work 4: Relationship between strain concentration and plastic deformation capacity of beam-to-column connections with oblique angles

This study analyzed the effects of oblique angles on the stress and strain distribution at beam-end connections. The results showed that with increasing horizontal oblique angles, strain concentrates at the obtuse zone of the beam end, leading to a reduction in the plastic deformation capacity of beam-end connections. Similarly, with increasing vertical oblique angles, strain concentrates at the upper flange, which also reduces the plastic deformation capacity. Additionally, the effects of beam span and beam section on strain concentration were also evaluated through FE analysis. However, this study did not establish a quantitative relationship between strain concentration and plastic deformation capacity. Such a relationship is also crucial for evaluating the seismic performance of beam-to-column connections.

Appendices

Appendix A. Comparison of increasing of strain concentration ratio

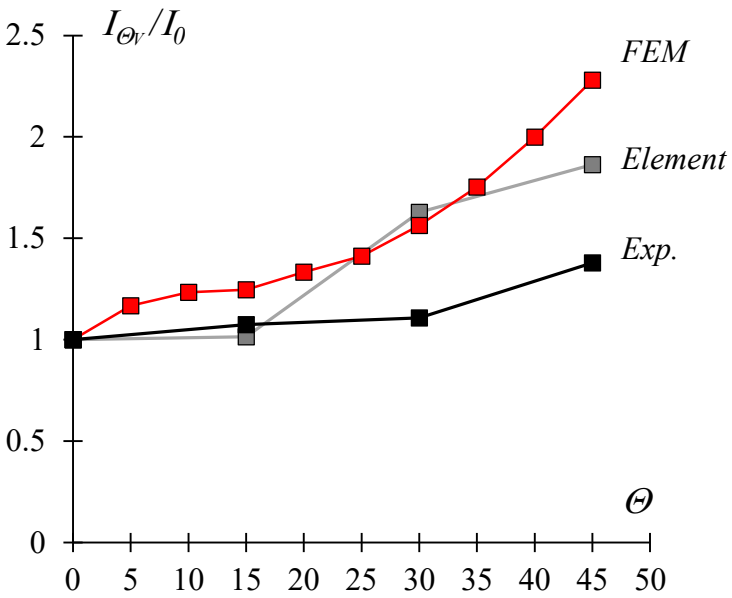

Fig. A-1 Comparison of increasing of strain concentration ratio.

In the analysis of horizontal oblique angles, the variation of the strain concentration ratio under different angles was presented. In Fig. 4.20, Since $\varepsilon_{max}/\varepsilon_{ave}$ at 0° is different, the comparison standards vary. To compare the increasing of strain concentration, here, $\varepsilon_{max}/\varepsilon_{ave}$ was defined as I_θ and I_0 was defined as the standard for comparison. The comparison of increasing of strain concentration ratio are shown in Fig. A-1. In the figure, different colors represent the results of FE analysis, element tests, and full-scale experiments. Comparing the

FE results with those of the two experiments, it can be observed that the FE results are closer to the element test results but slightly larger than the full-scale experiment results. However, a comparison of strain distribution reveals that significant strain concentration occurs in specimens S30 and S45 (see Fig. 2.20). The reason for the lower strain concentration ratio $\varepsilon_{max}/\varepsilon_{ave}$ obtained in the experiment is that the maximum strain ε_{max} measured in specimens S0, S15 S30 and S45 remained approximately the same across different oblique angles. Nevertheless, as shown in Fig. A-1, the trend of strain concentration increasing with larger oblique angles remains evident in both experimental result and FE analysis. Therefore, the FE analysis results can reasonably reflect the experimentally observed.

Appendix B. FE analysis of the element test

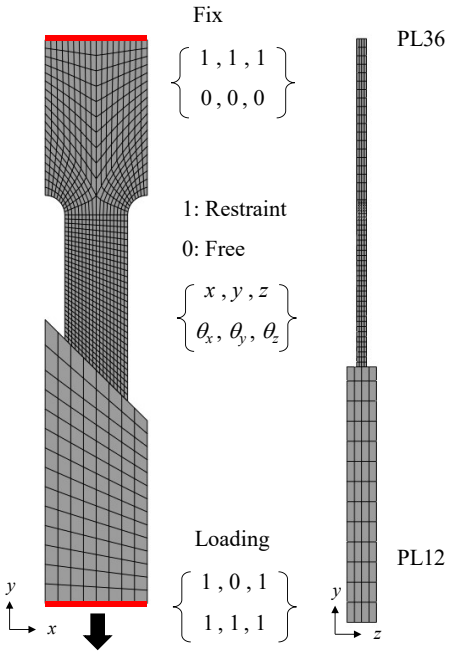

Fig. B-1 Loading condition of FE analysis on element test.

The FE analytical was also applied for the element test, the model of L0, L15, L30, L45 was conducted. The model of 45° specimen (L45) as an example, is shown in Fig. B-1. The figure illustrates the boundary conditions and the element discretization of the model. The modulus generated was fully based on the design of the element test. Hexahedral solid elements (C3D8R) were used for the analysis, and the material properties of the elements were determined using the results of material tests. The boundary conditions were same to

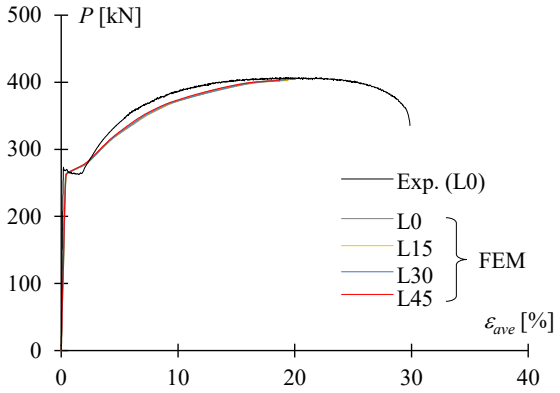

Fig. B-2 Loading behavior of FE analysis on element test.

those in the element test, with the bottom edge fixed and tensile loading applied to the upper edge.

The loading behavior obtained from the FE analysis are shown in Fig. B-2. The black line represents the results of specimen L0 from the element test, while the colored lines represent the FE analysis results. Since fracture analysis was not conducted in the material tests, the loading behavior of FE analysis are shown only up to the maximum strength. From the comparison between the FE analysis results and the experimental results, it can be observed that the FE analysis effectively reproduces the loading behavior observed in the experiment.

To identify the potential fracture locations of the specimen, the analysis was carried out with an extended tensile loading, allowing the specimen to develop necking. Fig. B-3 shows the locations of necking at the maximum deformation of the specimen. Comparing the necking locations, although there are slight differences in the necking positions among the specimens, the necking always occurs perpendicular to the specimen, indicating that the fracture is likely to occur at *u*-section. This result is consistent with the element test findings.

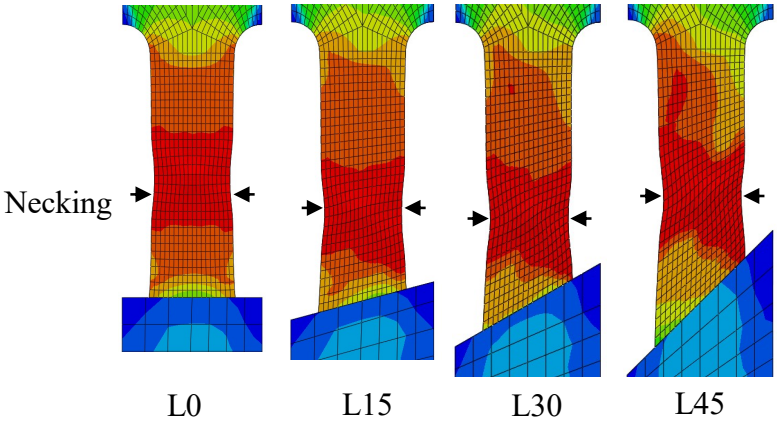

Fig. B-3 Location of necking at max strength.

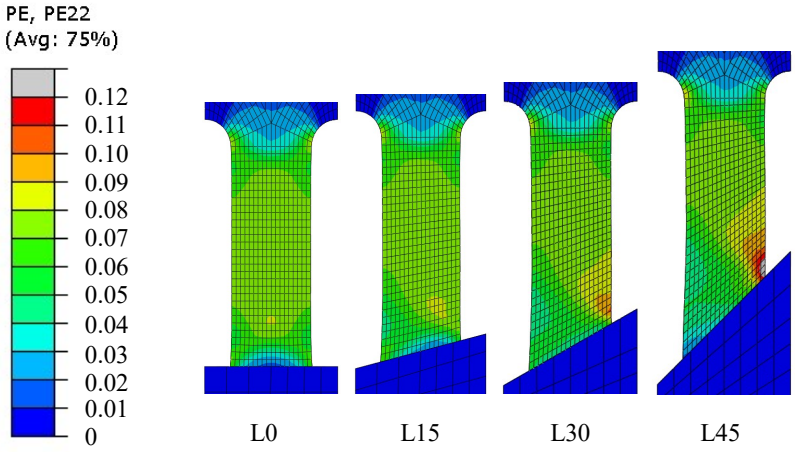

Fig. B-4 Plastic strain distribution from FE analysis at ε_{ave} = 0.07 (y direction).

Additionally, to observe the strain distribution of the specimen, the plastic strain distribution in the y-direction at the moment when ε_{ave}=0.07 are shown in Fig. B-4. From the strain distribution in the figure, it can be observed that, compared to the 0° specimen (L0) and 15° specimen (L15), the specimens with 30° (L30) and 45° (L45) exhibited significant strain concentration in the obtuse angle zone. This result is consistent with the strain distribution analysis from the element tests.

To evaluate the change of strain concentration, the strain distribution at u-section of obtuse angle zone was analyzed. The strain distribution at different horizontal oblique are shown in Fig. B-5(a). From the variation in the strain distribution, it can be observed that as the oblique angle increases, the strain on the obtuse angle zone gradually increases. The strain concentration ratio was used to analyze the changing of strain distribution, and the

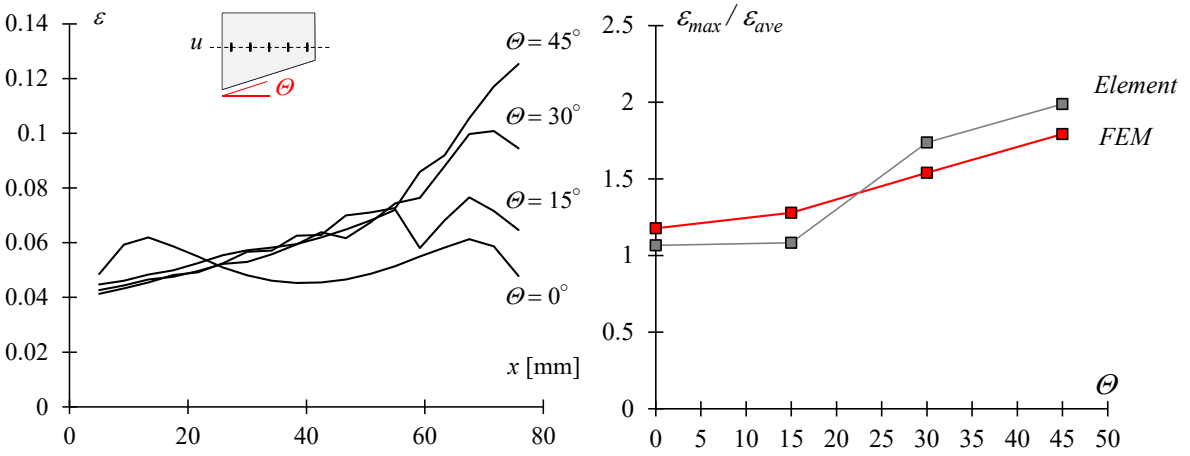

(a) Strain distribution at u-section (b) Strain concentration ratio at u-section

Fig. B-5 Comparison of strain concentration ratio on FEM and element test.

strain concentration ratio compared with that obtained from the element tests are shown in Fig. B-5(b). The results indicate that the variation in strain concentration ratio from the FE analysis and element test are nearly identical, demonstrating that the FE analysis effectively reproduces the strain concentration phenomenon observed in the element tests.

Acknowledgments

First and foremost, I would like to express my deepest gratitude to Professor Shoichi Kishiki for his invaluable guidance and unwavering support throughout my doctoral studies. Despite his busy schedule, he always took the time to provide me with insightful advice and encouragement. Under his mentorship, I was able to develop my academic knowledge and improve my ability to present my research clearly and effectively. My background in experimental structural engineering was initially limited, and I made many mistakes during my research. However, with his patient guidance, I was able to overcome these challenges, gain valuable experience, and grow as a researcher. I will always remember the times when he personally assisted me during my experiments. I am sincerely grateful for his support, and I will carry the lessons I have learned from him as I move forward in my career.

I am deeply indebted to Professor Tatsumi, who provided me with substantial guidance during my master's studies, particularly in my experiments and academic writing. During that time, he patiently and thoroughly explained everything to me, especially during the experimental setup, even when I had little prior knowledge. I also appreciate his patience, as my Japanese was not very strong, and I often had to ask the same questions multiple times. Despite this, he always responded kindly and encouraged me to improve. I am truly grateful for all the support he gave me during my time as a master's student, and I sincerely wish him success in his future research endeavors.

Beyond my professors, I am incredibly grateful to all my fellow lab members, whose assistance and encouragement made my doctoral journey a fulfilling and enjoyable experience. Their cooperation in experiments and insightful discussions helped me refine my research. I would like to extend my deepest gratitude to Kurosawa and Hirano, who have been by my side as my fellow classmates since I entered the lab and supported me throughout my research life until my doctoral graduation. They provided invaluable help in both my academic and daily life in Japan, making my experience much smoother and more enriching. I am also sincerely grateful to Nakada, who had already graduated but played a crucial role in guiding me when I first joined the lab. He helped me manage my experiments, taught me how to analyze data, and demonstrated his remarkable expertise. His support was instrumental in shaping my research approach. Additionally, I would like to express my heartfelt ap-

preciation to my dear Chinese friends who have already graduated: Li Jiaxi, Fuxiang, and Yang Xiaoyu. They have been my closest friends during my time in Japan, offering me unwavering support in my research life and bringing me countless joyful moments. Their friendship made my doctoral journey much more enjoyable and memorable. Lastly, I would like to extend my special thanks to Mey, who played an indispensable role in my experiments. He provided invaluable advice on both my research and dissertation, and his support in English writing was especially crucial.

Additionally, I would like to extend my deepest gratitude to my parents for their unconditional support and encouragement throughout my academic journey. Their belief in me has been my greatest motivation, and I would not have come this far without their love and support.

Finally, I want to express my sincere appreciation to everyone who has contributed to my research and academic growth. This dissertation is not only the culmination of my efforts but also the result of the collective support and guidance I have received from many people. I will cherish these experiences and continue striving for excellence in my future endeavors.